

Biomechanical Model of Pediatric Upper Extremity Dynamics During Wheelchair Mobility

Alyssa J. Paul
Marquette University

Recommended Citation

Paul, Alyssa J., "Biomechanical Model of Pediatric Upper Extremity Dynamics During Wheelchair Mobility" (2012). *Master's Theses (2009 -)*. 169.
https://epublications.marquette.edu/theses_open/169

**BIOMECHANICAL MODEL OF PEDIATRIC UPPER EXTREMITY
DYNAMICS DURING WHEELCHAIR MOBILITY**

by

Alyssa J. Paul, B.S.

A Thesis submitted to the Faculty of the Graduate School,
Marquette University,
in Partial Fulfillment of the Requirements for
the Degree of Master of Science

Milwaukee, Wisconsin

December 2012

ABSTRACT

BIOMECHANICAL MODEL OF PEDIATRIC UPPER EXTREMITY DYNAMICS
DURING WHEELCHAIR MOBILITY

Alyssa J. Paul, B.S.
Marquette University, 2012

Biomechanical analysis has been used by many to evaluate upper extremity (UE) motion during human movement, including during the use of assistive devices such as crutches and walkers. However, few studies have been conducted to examine the upper extremity kinetics during wheelchair mobility, specifically within the pediatric population.

In 2000, 90% of wheelchair users (1.5 million people) in the United States were manual wheelchair users, requiring the use of their upper body to maneuver the wheelchair as well as perform other activities of daily living. Among children under the age of 18, the wheelchair was the most used assistive mobility device at 0.12% of the USA population (about 88,000 children). Of these children, 89.9% (79,000) use manual wheelchairs.

Associated with the leading causes of assistive mobility device usage in children and adolescents, are severe cases of osteogenesis imperfecta (OI), cerebral palsy (CP), myelomeningocele (MM) and spinal cord injury (SCI). Once confined to a wheelchair, the upper extremities must take over the responsibilities of the lower extremities, including mobility and other activities of daily living. For many individuals who are wheelchair-bound since childhood, pain and other pathological symptoms present by their mid to late 20's. Due to increased life expectancy and continual wheelchair use, these injuries may cause the user to have reduced, or loss of, independent function as they age, further decreasing quality-of-life.

Better knowledge of upper extremity dynamics during wheelchair propulsion can improve understanding of the onset and propagation of UE pathologies. This may lead to improvements in wheelchair prescription, design, training, and long-term/transitional care. Thereby, pathology onset may be slowed or prevented, and quality of life restored. In order to better understand and model the UE joints during wheelchair mobility three main goals must be accomplished:

1. Create an upper extremity kinematic model including: additional segments, more accurate representations of segments and joint locations, consideration of ease of use in the clinical setting with children.
2. Create the corresponding kinetic model to determine the forces and moments occurring at each joint.
3. Implement the model and collect preliminary data from children with UE pathology.

ACKNOWLEDGMENTS

Alyssa J. Paul, B.S.

I would like to thank my fiancé, Bob, for always knowing when to help, when to listen and when to let me be. I would like to thank Bob, my mother, father and sister, for their love and supporting my decision to go back to graduate school and keep me company on my long drives to and from campus. I would like to thank my professors, the faculty, my committee and my advisors, specifically: Dr. Gerald Harris, Dr. Brooke Slavens, Jessica Fritz, Dr. Philip Voglewede, Joe Krzak and Adam Graf. Without the support, knowledge and guidance of these individuals, the following work would not be possible. I would like to thank the Graduate School and all of the Marquette University administration. Additionally I would like to thank the University of Wisconsin Milwaukee Gait Analysis and Biodynamics Laboratory, Shriners Hospital for Children – Chicago and the Froedtert Hospital for their assistance and hospitality.

LIST OF ABBREVIATIONS

3D – three dimensional
AA – acromial angle
AC – acromioclavicular
ADLs – activities of daily living
AI – inferior angle
C7 – spinal cervical 7 vertebrae
COM – center of mass
CP pathology – cerebral palsy
CP marker – coracoid process
CTS – carpal tunnel syndrome
DLOP pattern – double looping over propulsion
GH – glenohumeral
HUM - humerus
IJ – incisura jugularis
ISB – International Society of Biomechanics
ISG – International Shoulder Group
M3 – third metacarpal
M5 – fifth metacarpal
MM – myelomeningocele
MW – manual wheelchair
MWU – manual wheelchair user
OI – osteogenesis imperfecta
OLC – olecranon process
PAPAW – push activated power assist wheelchair
RAD – radial styloid
RMS – root mean squared
ROM – range of motion
SC – sternoclavicular
SC pattern – semi-circular
SCI – spinal cord injury
SLOP pattern – single looping over propulsion
SS – scapular spine
STRN – sternum, xiphoid process
SW - SmartWheel
TS – trigonum spinae
UE – upper extremity
ULN – ulnar styloid

TABLE OF CONTENTS

ACKNOWLEDGMENTS.....	i
LIST OF ABBREVIATIONS.....	ii
CHAPTER	
I. INTRODUCTION.....	1
1.1 Background.....	1
1.1.1. Pediatric Wheelchair Usage and Pathology.....	1
1.1.2. Wheelchairs	2
1.1.3. Upper Extremity Anatomy	6
1.1.3.1. Shoulder Girdle.....	6
1.1.3.2. Elbow Joint	10
1.1.3.3. Wrist Joint	11
1.2 Significance.....	12
1.3 Previous Work.....	13
1.3.1. Wheelchair Stroke Patterns	13
1.3.2. Wheelchair Kinematics	17
1.3.3. Wheelchair Kinetics	30
1.3.3.1. The SmartWheel.....	30
1.3.3.2. Wheelchair Kinetics	31
1.4. Hypothesis and Specific Aims.....	44
II. UPPER EXTREMITY MODEL FEATURES	45
2.1 Previous Model / Slavens Model.....	45
2.2. Addition of Scapula and Clavicle Segments	46

2.3. Scapula Markers Tracking Technique	47
2.4 Body Segment Parameters.....	52
2.5 Locations of Joint Centers	56
2.5.1 Elbow Joint Center	56
2.5.2 Glenohumeral Joint Center	58
2.6 Thorax Kinematics	62
 III. BIOMECHANICAL MODEL OF PEDIATRIC UPPER EXTREMITIES DYNAMICS DURING WHEELCHAIR MOBILITY	66
3.1 Introduction/Model Aims.....	66
3.2 Methods.....	67
3.2.1 Kinematics	67
3.2.1.1 Joint Centers	70
3.2.1.2 Segment Coordinate Systems	73
3.2.1.3 Euler Angle Sequence	75
3.2.2 Kinetics	76
3.2.2.1 Instrumentation	77
3.2.2.2 Kinetic Model Inputs	78
3.2.2.3 Inverse Dynamics	79
3.2.2.4 Kinetic Model Equations	80
3.2.3 Application to Patient Population	84
3.2.3.1 Testing Protocol	85
3.3 Results.....	86
3.3.1. Upper Extremity Kinematics	86

3.3.2 Upper Extremity Kinetics	95
3.4 Discussion.....	101
3.4.1. Kinematics	101
3.4.2. Kinetics	105
3.4.3. Summary	107
IV. CONCLUSION	108
4.1. Summary.....	108
4.2. Future Work.....	108
4.3. Concluding Remarks.....	109
V. REFERENCES.....	110
VI. APPENDICES.....	118
Appendix 1: Yeadon and Morlock Inertia Equations	119
Appendix 2: Sign Convention.....	120
Appendix 3: MATLAB Source Code.....	121
A.3.1. Parameters (*.m).....	121
A.3.2. Biomechanical Model (*.m).....	123
A.3.3. Scapula Kinematics (*.m).....	135
A.3.3.1 Main Scapular Kinematics	135
A.3.3.2 Veldpaus Rotation Matrix Calculation.....	138
A.3.4. Additional Functions in Biomechanical Model (*.m) ...	139
Appendix 4: Coordinate System Figures.....	140
Appendix 5: SmartWheel Specifications.....	143

CHAPTER 1: INTRODUCTION

1.1 Background

1.1.1 Pediatric Wheelchair Usage and Pathology

In 2000 there were about 1.7 million wheelchair users in the United States. Of this group, 90% (1.5 million) were manual wheelchair users (MWUs), requiring the use of their upper body to maneuver the wheelchair as well as perform other activities of daily living. Among children under the age of 18, the wheelchair was the most used assistive mobility device at 0.12% of the USA population (about 88,000 children). Of these children, 89.9% (79,000) use manual wheelchairs [1].

Associated with the leading causes of assistive mobility device usage in children and adolescents, are severe cases of osteogenesis imperfecta (OI), cerebral palsy (CP), myelomeningocele (MM) and spinal cord injury (SCI). Osteogenesis imperfecta, or brittle bone disease, is a genetic defect that causes a lack of collagen production resulting in weak bones that are more susceptible to fracturing. In severe cases, bowed legs and scoliosis can severely impair a person's mobility, confining them to a wheelchair [2]. Cerebral palsy is caused by a brain injury or other problem that occurs during pregnancy, birth or the first three years of life. While challenging to define, CP "describes a group of disorders of the development of movement and posture..." [3]. Myelomeningocele, or spina bifida, is a developmental disorder occurring in the womb, caused by the incomplete closing of the embryonic neural tube and often some vertebrae. Physical complications may include weak or paralyzed legs and orthopedic abnormalities, resulting in most individuals requiring the use of assistive devices, such as wheelchairs,

for mobility [4]. Lastly, spinal cord injury more broadly encompasses all injuries to the spine that are not disease related. Injuries can range from pain to paralysis, and serious motor problems often require assistance of a wheelchair for mobility [5].

1.1.2 Wheelchairs

Lusardi describes: “A wheelchair, or wheeled mobility device, is a complex piece of assistive technology,” [6] and, as mentioned earlier, is the most used assistive mobility device amongst children under 18 years of age [1]. A wheelchair must provide a means for mobility as well as support, and facilitate all other activities of daily living, including: work tasks, personal care, and recreation. Lusardi says a wheelchair consists of three main components: the postural support structure, the supporting structure (or frame), and the propelling structure. The postural support structure, or seating system, is greatly important as the human body is not well designed for sitting and will develop orthopedic changes over time when confined to a seated position [7]. The goals of the seating system include: effective postural support for the lower body, trunk and pelvis and any other area of concern (sometimes including the head), optimal soft tissue loading through pressure distribution (to reduce chances of pressure sore development), optimal comfort for long periods of time, and the ability to easily access and use the mobility interface component [6]. Considerations for the postural support include the prevention of resulting orthopedic complications, maintaining vital organ capacity (as spinal changes create pressure on internal organs), reducing soft tissue strain (such as those at the wrist, elbow and shoulder that result from propelling a wheelchair in awkward positions to due poor fit), providing comfort and increasing endurance and tolerance [7]. Schmeler goes on to state that often accommodating posture, rather than correcting it, is the goal. When

a postural support structure is properly designed, results show an increase of motor control, attention/awareness, independence, communication and work performance [7]. The supporting structure is the framework of the wheelchair that connects the seating system to the mobility structure, enabling the user to access the mobility system. There are many types of frames available, such as: rigid, folding, tilt, recline, or even standing, allowing for a multitude of wheelchair configurations [6]. Additionally, frame material options provide different strength and durability, as well as overall wheelchair weight [8, 9]; however due to price and machinability tradeoffs are sometimes inevitable [8]. The wheelchair's propelling structure is made up of the tires, caster wheels, drive wheels and a user interface. The main objective of the propelling structure is to facilitate subject mobility, promote safety and prevention of overuse injuries, and maximize efficiency, while also allowing for subject independence and functionality in everyday activities [6].

Design decisions to be made when deciding on the correct manual wheelchair prescription include: rigid or folding frame, wheelchair weight, wheel size and type, wheel axle placement and camber angle, seat cushion type, and handrim size. The type or presence of a back support, arm rests, foot rests, push handles, casters, suspension and anti-tippers must also be determined. Additionally, patient specific measurements are required to determine the proper settings for seat width, height and depth; seat angle; and seat back height and angle. [10] All of these decisions are based on seating and mobility assessments performed by an interdisciplinary team. These assessments begin with gathering detailed information on the subject's health history and living environments. A systems review typically follows, examining issues such as: range of motion, muscle strength and postural asymmetries (musculoskeletal system); heart rate and blood

pressure (cardiovascular system); respiratory rate, shortness of breath and blood oxygenation (pulmonary system); skin inspection, ability to perform pressure reliefs (integumentary system); and various neurological, communication and cognitive systems tests. The results of the systems review help determine areas requiring a more detailed examination with specific tests, such as: mat evaluations, seating and equipment simulations, and pressure mapping. Required tests are performed for each patient in order to determine their functional level and adaptive seating and wheeled mobility needs. Medical professionals can then provide the correct wheelchair equipment prescription. [6]

The list of decisions may seem daunting, but according to Schmeler: “care should be taken in setup and prescription to avoid potential damage” [7]. Manual wheelchair users have an increased chance of developing repetitive stress injuries as well as pressure sores that reduce functionality and quality of life [8, 11]. Improper wheelchair fit has been shown to be related to incorrect propulsion and multiple injuries. Boninger et al. found that the axle position relative to the shoulder can significantly alter pushrim biomechanics. There is an inverse relationship between the push angle and the vertical distance between the axle and the shoulder, which means when the user’s shoulder is farther away from the wheel axle, there is less handrim surface area within their reach. Additionally, Boninger et al. showed that when the axle is positioned farther back relative to the subject, the frequency of propulsion increased and the rate at which the propulsive force increased was higher. By moving the axle to the farthest forward position, the weight of the subject is placed more over the larger rear wheels, which reduces rolling resistance and thus the frequency of propulsion. Additionally, a forward axle position

allows the subject to reach more of the handrim which increases the push angle and decreases the rate of increase in propulsive force application [12]. Shoulder to axle alignment should be directly vertical to optimize force dispersion, proper muscle recruitment and decrease awkward arm positioning [9]. In another study, van der Woude et al. determined that seat height is an important wheelchair adjustment and provides optimal cardiorespiratory responses when the elbow angle is near 100 to 120 degrees of extension with the subject at rest, hands on the top-dead-center of the hand rims [13]. Also, while seat back height is dependent upon individual comfort and support needs, it must be low enough so that it does not interfere with the arms' natural range of motion, or the subject's ability to contact a sufficient amount of pushrim surface area [9] and optimally propel the wheelchair. As a solution, when high seat back height is necessary, a narrower upper back should be used in order to allow for increased scapular excursion. Another wheelchair setting of concern is the seat pan, if too wide the subject must abduct the upper arms to a greater degree in order to reach the handrim for propulsion, increasing difficulty. [14]

In conclusion, a standard, one-size-fits-all wheelchair is inappropriate, inefficient and even harmful, to the long-term manual wheelchair user. Manual wheelchairs must be highly customizable in order to accommodate the multitude of pathologies and injuries that result in their use. The pediatric population is no exception, with arguably more difficulty in properly prescribing the wheelchair to accommodate their smaller, still developing musculoskeletal systems. Wheelchairs designed for the pediatric population reduce the overall seat dimensions and weight in order to facilitate easier movement [9].

Correct, subject specific prescription is important to maintain comfort, functionality and quality of life for manual wheelchair users of all ages.

1.1.3 Upper Extremity Anatomy

1.1.3.1 Shoulder Girdle

Although the shoulder joint is commonly thought to be the glenohumeral joint, it actually comprises four joints: sternoclavicular, scapulothoracic, acromioclavicular and glenohumeral. These joints, sometimes called the shoulder girdle, are constructed with the sternum, ribs, clavicles, scapulae and humeri (see Figure 1).

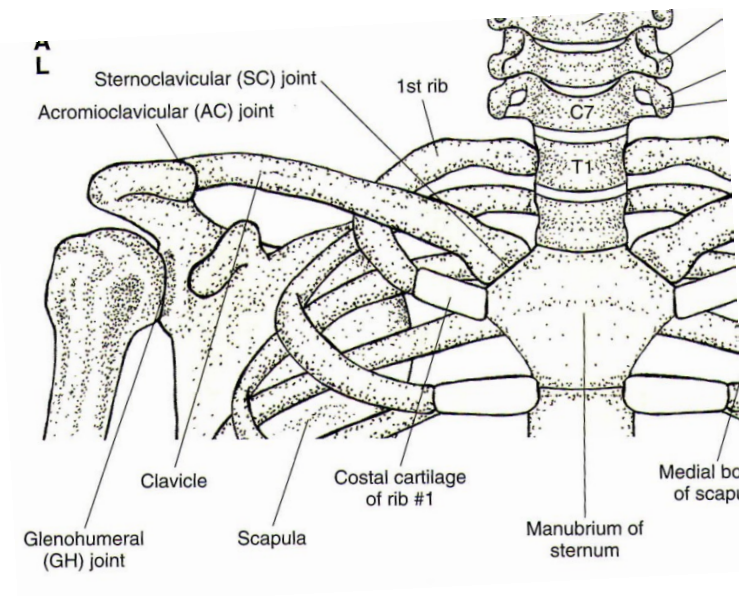


Figure 1. Shoulder Complex: the glenohumeral, sternoclavicular and acromioclavicular joints, anterior view [15]. Figure reprinted with permission.

The glenohumeral joint is a ball and socket type joint that allows flexion, extension, abduction, adduction, medial and lateral rotational articulations between the humeral head and the glenoid cavity of the scapula. The center of rotation is modeled as the

geometric center of the glenohumeral joint. Ranges of motion for healthy individuals have been found to be at least 120 degrees of flexion (flexing the shoulder to almost 180 degrees requires the rotation of the scapula to comprise the remaining 60 degrees), 65 degrees of active extension and up to 80 degrees of passive extension. Additionally, the glenohumeral joint experiences around 120 degrees of abduction, though a wide range of values have been reported. When the arm is adducted, the GH joint can provide about 75-85 degrees of internal rotation and 60-70 degrees of external rotation, although much variation exists. [16]. Another source reports 55-95 degrees of internal rotation and 40-90 degrees of external rotation, with the rotation ranges depending upon the state of upper arm abduction/adduction [17]. For example when the arm is abducted approximately 90 degrees, the GH joint is capable of 90 degrees of external rotation.

The sternoclavicular joint is located where the medial end of the clavicle meets the manubrium of the sternum (Figure 1). This is a 3 degree of freedom saddle joint, which allows for bones to spin relative to one another; however, limitations exist due to the interlocking nature of the bones at the joint. The SC joint motions are described as elevation and depression in the frontal plane, protraction and retraction in the transverse plane and axial rotation in the sagittal plane. Typical maximum elevation angles and maximum depression angles seen at the SC joint are around 45 degrees and 10 degrees respectively and typically occurs almost parallel to the frontal plane and around the anterior-posterior axis. The protraction and retraction rotations of the SC joint occur almost parallel to the transverse plane around the superior-inferior axis. Maximum angles in each direction are between 15 and 30 degrees of rotation. Lastly, rotation around the longitudinal axis of the clavicle, which occurs during shoulder abduction or

flexion, typically results in 20 to 35 degrees of posterior rotation. [16] However, available landmarks for segment definition generally only allow two markers to be placed on the clavicle, restricting the model to only capture motion in the transverse and frontal planes. Sagittal plane, axial rotation of the clavicle may not be, and is usually not, modeled [18, 19, 20].

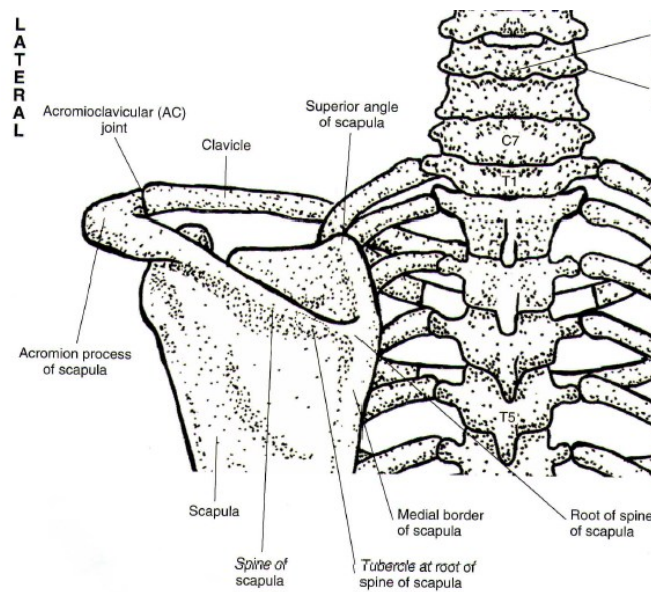


Figure 2. Shoulder Complex: the acromioclavicular and scapulathoracic joints, posterior view [15]. Figure reprinted with permission.

The point at which the lateral end of the clavicle meets the acromion of the scapula is the acromioclavicular joint (Figure 2). This is a plane, or gliding, joint, allowing only a sliding motion between the two surfaces, similar to the wrist joints. While the SC joint allows for extensive movement of the clavicle, which guides scapular motion, the AC joint allows for more subtle movements between the scapula and clavicle, which optimizes the mobility and fit between the scapula and thorax. The most noted and visible motion of the scapula around the clavicle is upward and downward rotation which

occurs in the plane of the scapula though it is considered to frontal plane motion. Up to 30 degrees of AC joint upward rotation may be seen as the arm is lifted above the head. Upward rotation occurs naturally as the shoulder is flexed or abducted, just as downward rotation returns the scapula to anatomical position and occurs naturally during arm extension and adduction. Rotations in the sagittal and transverse plane are considered rotational adjustment motions that properly align the scapula along the thorax. Sagittal plane motions occur around the AC joint close to the medial-lateral axis. Rotation of the inferior angle away from the posterior side of the thorax is called anterior tilting while rotation of the inferior angle toward the posterior side of the thorax is called posterior tilting. Lastly, rotations around the AC joint in the transverse plane, called internal and external rotations occur around the superior-inferior vertical axis. Due to the technical difficulties in motion capture of the scapulae and clavicles, AC joint kinematics have been reported between 5 and 30 degrees of motion in each the transverse and sagittal planes. [16]

Lastly, the scapulothoracic (or scapulocostal) joint is the articulation between the anterior surface of the scapula and the posterior-lateral wall of the thorax, which are separated by muscle tissue (Figure 2). This is not a joint in the traditional sense and results in a gliding motion between the two surfaces, allowing for scapular depression, elevation, retraction and protraction, etc. [16] It is not often included in kinematic models due to modeling complexity and because the amount of scapular elevation, depression, retraction and protraction may be determined through other means [21].

One of the main points is that the extensive motions of the humerus are actually combinations of rotations at the GH, AC, SC and scapulothoracic joints. [16]

1.1.3.2 Elbow Joint

The elbow and forearm comprises four joints: humeroradial, humero-ulnar, distal radio-ulnar and proximal radio-ulnar. The main bones involved include the humerus, radius and ulna (Figure 3). The elbow motion is associated with the humeroradial and humero-ulnar joints, often modeled together as a singular hinge joint, restricting the possibility of varus and valgus movements.

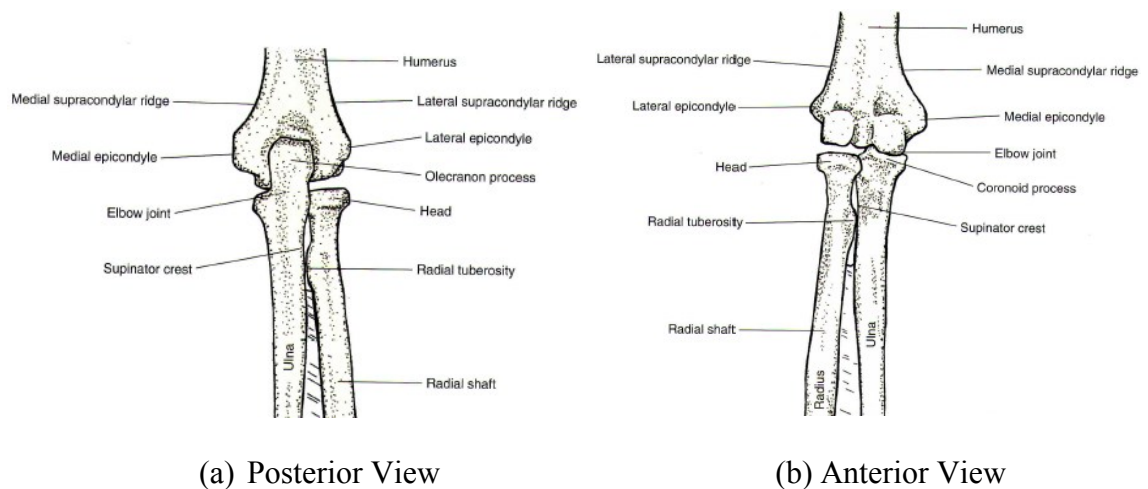


Figure 3. Posterior(a) and anterior (b) views of the left elbow joint. [15] Figure reprinted with permission.

The medial –lateral axis of the elbow, around which flexion and extension occurs, angles slightly superiorly on the lateral side. This results in a natural angle between the forearm and upperarm when the elbow is fully extended. This angle is called the normal cubitus angle, or the carrying angle and is around 13 degrees for men and 15 degrees for women, and always greater for the dominant arm. Elbow joint ranges of motion: about 145 degrees of passive flexion and 5 degrees of passive extension, past neutral. Though for most activities of daily living the elbow joint experiences 30 to 130 degrees of

flexion. On average the radio-ulnar joint experiences about 75 degrees of pronation and 85 degrees of supination, though many activities of daily living require only 50 degrees of rotation in either direction. [16]

1.1.3.3. Wrist Joint

The wrist consists of three joints: radiocarpal, midcarpal and intercarpal. There are many bones involved in the motions of the wrist, including the radius and the carpal bones. The wrist itself comprises eight bones, creating two rows of four. The distal row of wrist bones, moving laterally from the radial side of the hand, includes: trapezium, trapezoid, capitate and hamate. The proximal row of wrist bones, moving laterally from the radial side of the hand, includes: scaphoid, lunate, triquetral and pisiform.

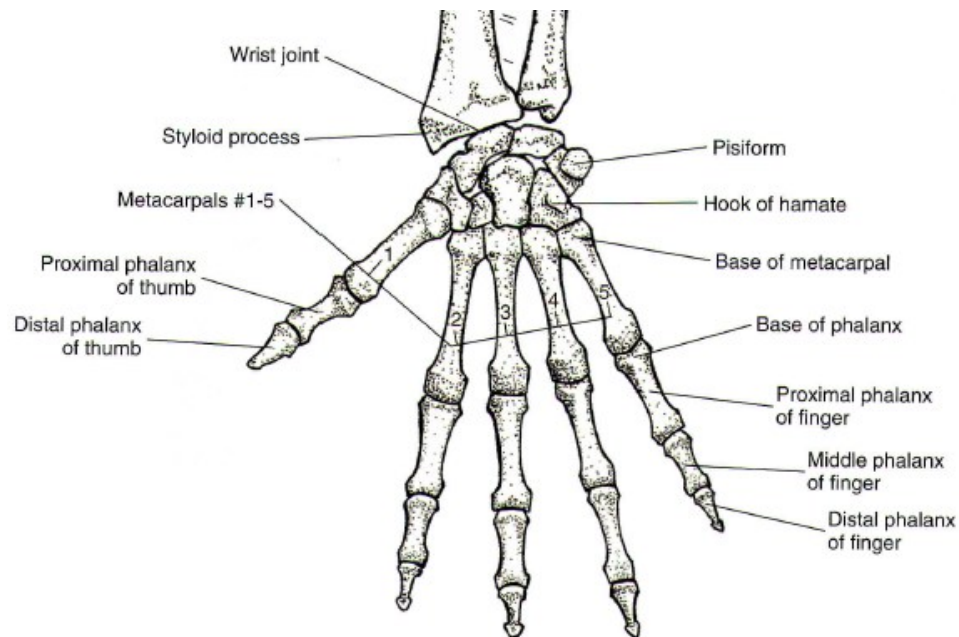


Figure 4. The wrist joint, anterior view, radius is the larger distal head on the left side and the ulna is the small distal head on the right side. [15] Figure reprinted with permission.

The wrist is defined as a two degree of freedom joint: with flexion/extension occurring in the sagittal plane and ulnar/radial deviation occurring in the frontal plane. Normal ranges of motion for adults are the following: 70 to 85 degrees of flexion, 60 – 75 degrees of extension, with flexion usually exceeding extension about 15 degrees and with total sagittal motion between a 130 and 160 degree range. The range of motion of the wrist in the frontal plane is around 50 to 60 degrees with 15 to 20 degrees consisting of radial deviation and the remaining 35 to 40 degrees of ulnar deviation. [16] Note that there is no distinct rotation of the wrist in the transverse plane, although minor amounts of rotation are possible [22].

1.2 Significance

Use of a manual wheelchair requires the upper extremities (UE) to take over the responsibilities of the lower extremities, including mobility and other activities of daily living. Additional tasks that the upper body must now perform include weight relief and transfers into and out of the wheelchair. These activities are repetitious and require high loads to be applied to the wrist, elbow and shoulder joints which are not structured to handle such loading patterns [23, 24]. Due to these increased UE demands, the upper body experiences pathologies it may not otherwise encounter, including: carpal tunnel syndrome [24], shoulder impingement and tendinitis. Additionally, the combination of repetitive actions and awkward positioning, as seen during wheelchair propulsion, exacerbates the problem [23]. It has been documented that 30-73% of manual wheelchair users with paraplegia experience shoulder pain [23, 25, 26]. All of these factors further restrict a person's mobility and ability to perform ADLs, which are important for an individual's self-esteem and independence [25]. Lundqvist et al. found that severe pain

was the only complication that resulted in a decreased quality-of-life [27]. For many individuals who are wheelchair-bound since childhood, pain and other pathological symptoms present by their mid to late 20's. Due to increased life expectancy and continual wheelchair use, these injuries may cause the user to have reduced, or loss of, independent function as they age, further decreasing quality-of-life [14].

1.3 Previous Work by Others

In order to reduce the prevalence of upper extremity pain and injury in manual wheelchair users, information must be obtained regarding the interactions within the wheelchair-user system. Analyzing the movements and loading patterns of the body segments and joints during wheelchair mobility will result in greater understanding of pain and injury origin and propagation. This knowledge will hopefully lead to successful interventions in quelling the onset and proliferation of UE pain and pathology during manual wheelchair use.

1.3.1 Wheelchair Stroke Patterns

Wheelchair stroke patterns and spatiotemporal factors have been investigated and characterized in many studies. The patterns have been analyzed via variables including joint accelerations, joint ranges of motion, stroke efficiency and percent of time spent with the hand in contact with the handrim (propulsion phase) versus not in contact (recovery phase). It has been shown that semi-circular hand motion provides the most efficient motion [28] with the least risk of UE injury.

In 1985 Sanderson and Sommer were the first to research wheelchair propulsion pattern characterization. The three male athletes exhibited two different stroke patterns:

pumping and circular. Sanderson and Sommer concluded that the circular pattern was more advantageous to the MWU due to the increased time spent in the push phase [29]. In 1989 Veeger et al. investigated manual wheelchair propulsion patterns and kinematics of 5 experienced manual wheelchair athletes at different propulsion speeds. Veeger et al.'s confirmed the pumping and circular stroke patterns found by Sanderson and Sommer. Additionally, Veeger et al. found a significantly greater gross mechanical efficiency when using the circular stroke pattern versus the pumping pattern [30].

In 1998 Shimada et al. characterized manual wheelchair propulsion patterns through a kinematic and kinetic investigation of seven experienced manual wheelchair athletes with spinal cord injury during 1.3 m/s and 2.2 m/s propulsion speeds. Joint excursions and accelerations, propulsion phase time and stroke efficiency were analyzed through use of marker tracking and a SmartWheel (sections 1.3.3.1 & 2.2.5). Plots of the metacarpal joint marker position in the sagittal plane revealed three stroke patterns: semicircular (SC), single looping over propulsion (SLOP) and double looping over propulsion (DLOP). The SC pattern involved the hand dropping below the handrim during the recovery phase (similar to the circular pattern as seen by both Sanderson et al. and Veeger et al.), while during the SLOP pattern the hand comes above the handrim during recovery phase. In the DLOP pattern the hand comes up over the handrim after release (like the SLOP pattern) but then drops below the handrim (like the SC pattern) before coming in contact with the handrim again, creating a figure-eight-like motion. At the 1.3 m/s propulsion speed the SC pattern showed significantly smaller elbow and shoulder joint accelerations in flexion/extension while also showing significantly larger shoulder joint accelerations in abduction/adduction than the DLOP pattern. During both

propulsion speeds the SC pattern showed significantly larger elbow joint range of motion than the SLOP or DLOP patterns and at the faster speed had significantly larger shoulder abduction/adduction joint angle ROM. The data provided by the SmartWheel, showed a significantly greater percentage of time is spent in the propulsion phase rather than the recovery phase during the SC pattern compared to the SLOP and DLOP patterns at both propulsion speeds. Shimada et. al. also calculated stroke efficiency. They stated that only tangential force applied to the handrim contributes to forward motion of the wheelchair and defined stroke efficiency as the square of the tangential handrim force divided by square of the resultant force. The SC stroke pattern had higher stroke efficiency than the SLOP and DLOP patterns, though not significantly. Shimada et al. concluded that since high joint accelerations contribute to injury, the lower joint accelerations of the SC pattern may lessen the risk of injuries. Additionally, while the SC pattern has larger elbow and shoulder joint ROMs, the peaks were within the normal range and therefore likely do not contribute to injury. Shimada et al. conjectured that the greater percentage of time spent in the propulsion phase results in more time for force application at the handrim, leading to greater stroke efficiency, as seen with the SC pattern. Overall, Shimada et al. hypothesized that the SC stroke pattern was the most biomechanically efficient and least likely to result in injury [28].

The main limitation with the previous studies was the small sample size. In 2002 Boninger et al. classified the stroke patterns of thirty-eight experienced MWU with SCI, while investigating stroke pattern force and cadence and speed effects on stroke pattern, efficiency, and bilateral symmetry. The positions of markers on the subjects' third metacarpophalangeal joint and the rear wheel axle were recorded for kinematic analysis

and a SmartWheel captured handrim kinetic data while the subject propelled his or her own wheelchair on a dynamometer at two different steady-state speeds. All four patterns, SC, SLOP, DLOP, and arcing (similar to pumping), seen amongst the previously mentioned studies were observed. SLOP was the most common (45%), followed by DLOP (25%), SC (16%) and arcing (14%). Most subjects (58%) used the same propulsion pattern bilaterally and at both speeds, although several subjects exhibited the opposite. Additionally, at higher speeds the subjects spent greater time in the recovery phase than the propulsion phase of the stroke cycle, and mechanical efficiency decreased. Also, with increased body weight, all handrim forces increased. There were no significant differences in pushrim forces amongst propulsion patterns. This was deemed logical as the propulsion patterns are only different during recovery phase since the hand is restricted to the path of the pushrim during the push phase [31]. As with Shimada et al. [28], Boninger et al. saw the lowest cadence and greatest propulsion phase time during the SC pattern. Boninger et al. came to the same conclusion as Shimada et al. in that the SC stroke pattern is the most advantageous [31]. Additionally, Boninger et al. concluded that “assuming that the left and right sides are identical may lead to errors”. Boninger et al. and Shimada et al. recommend clinicians train patients to use the semicircular stroke pattern in order to decrease stroke frequency, abrupt directional changes and extra hand movements, thereby increasing stroke efficiency and reducing injury risk [28, 31].

In 2003 Koontz et al. advised MWUs is to use long, smooth strokes in order to reduce the occurrence of high joint forces and the rate of pushrim loading. Additionally, Koontz et al. advised that the wheelchair user allow the hand to drift down below the pushrim when letting go and to continue to keep the hand below the handrim while not in contact

with the pushrim, following the SC stroke pattern [32]. This same advice was proposed in a 2005 article by Boninger et al. after analyzing manual wheelchair propulsion of SCI subjects [33]. A 2007 article in Paralegia News also suggested the use of the semicircular propulsion pattern in order to avoid overly repetitive strokes and high, inefficient forces that increase the risk of pain and pathology [34].

1.3.2 Wheelchair Kinematics

In addition to studying wheelchair stroke patterns and spatiotemporal factors, upper extremity models have been created to calculate joint kinematics occurring during wheelchair propulsion. Joint ranges of motion, angular velocities and angular accelerations have been well documented [24, 30, 35-44].

Rao et al. conducted one of the first studies investigating shoulder, elbow and wrist joint kinematics during manual wheelchair use. The subjects analyzed comprise 16 males (aged: 19-50) with low level paraplegia due to traumatic SCI. Mean maximum and minimum joint angles were determined for the group as well as the average transition point from push phase to recovery phase. The transition point occurred at 32% of the overall stroke cycle. Humeral elevation, abduction/adduction with respect to the global coordinate system, achieved a maximum angle of 56.6° at 94% of the stroke cycle and a minimum angle of 22.5° at 42% of the stroke cycle. Sagittal plane humeral rotation exhibited a maximum angle of 23.2° at 40% stroke cycle and a minimum angle of -57.3° at 93% stroke cycle. Lastly, maximum and minimum humeral internal/external rotation angles were 86.2° at 95% and 11.6° at 41%, respectively. All three humerus rotations reached extremes during the recovery phase. Maximum humeral elevation and internal rotation, and minimum sagittal plane rotation all occurred towards the end of recovery

phase, close to the next hand contact. The elbow experienced maximum flexion of 76° at 15% of the stroke cycle and minimum flexion of 34.2° at 39% of the stroke cycle. The maximum and minimum forearm pronation angles were 32° at 96% and 8.5° at 27%, respectively. Forearm carrying angle ranged from -11.2° at 43% of the stroke cycle to -2° at 98% of the stroke cycle. Lastly, the average maximum wrist joint angles were 17.9° at 28% and -30.9° at 99% in flexion and extension, respectively, and 23.8° at 28% and -7.3° at 90% of ulnar and radial deviation, respectively. Wrist maxima were reached towards the end of the push phase, while the minima were exhibited late in the recovery phase. Rao et al. characterized these kinematic patterns to serve as a starting point and reference for data comparison with future studies. [39]

Due to the high prevalence of carpal tunnel syndrome (CTS) in MWU (up to 50-60% in SCI patients [24]), multiple research studies were conducted specifically investigating the wrist joint [35, 24, 40]. In 1997, Boninger et al. investigated wrist biomechanics of 6 Paralympic athletes who were MWUs during two speeds of wheelchair propulsion on a dynamometer. Boninger et al. determined that at the beginning of the stroke cycle, when the hand contacts the pushrim, the wrist was slightly extended, supinated and radially deviated. During the beginning of the push phase the wrist slightly increases its radial deviation before moving into ulnar deviation over the remainder of the push phase. Additionally, the wrist exhibited decreasing extension throughout the push phase, with slight flexion before the start of recovery phase. The pronation/supination of the wrist showed the greatest variability, though most subjects pronated as they moved through the push phase. While Boninger et al. believe that MWUs will inevitably develop CTS, their previous work has not found wheelchair racers at a higher risk for CTS. Boninger et al.

postulate that wheelchair racers are able to minimize injurious wrist motions during wheelchair propulsion because they are knowledgeable of wheelchair setup and customization and they focus on stroke efficiency necessary for racing. Therefore, Boninger et al. suggest that proper, subject-specific wheelchair setup and propulsion technique training will reduce wrist pain and pathology. [35]

Similar research focused at the wrist joint was conducted by Veeger et al. A three-dimensional analysis of the wrist was conducted during the push phase of wheelchair mobility. There were a total of nine subjects: four MWUs and five controls (some with previous MW experience). The subjects propelled a manual wheelchair at three different velocities on a treadmill at three different slopes. The radial-ulnar deviation range of motion values were similar to those of Boninger et al. and slightly larger than those reported by Rao et al. Additionally, the flexion-extension range of motion determined for the control group was similar to the values of MWUs determined by Boninger et al. and Rao et al. Veeger et al. suggest that differences between controls and MWUs may be more than differences in physical ability and experience. Additionally, Veeger et al. postulate that the differences in flexion-extension ranges of motion may be accounted for by handrim gripping styles, as a power grip restricts wrist motion, while a contact grip allows for greater wrist flexibility. Veeger et al. concluded that the large wrist ROMs (particularly when it rises above the reported active ROMs) are a likely contributing factor to wrist ailments, such as CTS, commonly experienced by MWUs. [24]

In an interesting study by Wei et al. in 2003, the effects of seat height on wrist kinematics were investigated. Wei et al. found that increasing seat height resulted in lower wrist ROMs, decreased wrist extension, and decreased radial deviation.

Additionally, increasing the seat height decreased push time and therefore decreased the amount of time that the hand is in contact with the handrim. It was concluded that wheelchair seat height is a critical factor in wrist kinematics. While one particular seat position was not found appropriate for all, care should be taken when setting the seat height in order to reduce extreme wrist positions associated with pain and pathology development. [40]

Boninger et al. also reported on Paralympic wheelchair athletes' shoulder and elbow kinematics. In general, the internal rotation and abduction of the shoulder joint decreased over the stroke cycle and sagittal plane motion moved from an extended state to a flexed state. During the push phase of the stroke cycle the elbow started in a slightly flexed position, increased initially and then extended almost completely by the end of the push phase. Interestingly, Boninger et al. noted two distinct elbow patterns during the recovery phase. One half of the subjects exhibited a gradual return of the elbow to the flexed position required for the beginning of the next stroke cycle, while the other half rapidly flexed their elbows to a larger than needed angle and then extended the elbow in order to reach the required arm position for the next stroke cycle. The movement patterns remained the same at both speeds; however, the average ROMs did not. During the faster propulsion speed, the subjects had greater shoulder adduction and increased shoulder and elbow sagittal plane flexion/extension. Boninger et al.'s ranges of motion and peak angular values are comparable to those obtained by Rao et al. The observed differences in minimum internal/external shoulder rotation and shoulder sagittal plane flexion-extension are likely explained by the different methods of shoulder angle calculations. Rao et al. determined shoulder motion relative to the global coordinate system while

Boninger et al. calculated shoulder joint angles with respect to the trunk coordinate system. [41]

Also published in 1998 was a study conducted by Davis et al., which specifically evaluated the kinematics of the shoulder complex. Ten subjects with minimal wheelchair experience propelled two different wheelchairs (adjustable and conventional) while the 3D positions of markers placed on bony landmarks of the left arm and thorax were collected. Joint angles were calculated with the humerus relative to the thorax. Maximal humeral elevation occurred shortly after release of the handrim while the minimum occurred shortly after handrim contact. The minimum amount of humeral elevation was significantly smaller for the conventional wheelchair versus the adjustable wheelchair. All other differences, while insightful, were not significantly different. During the recovery phase there was less internal shoulder rotation, but more overall shoulder motion when the adjustable wheelchair was used. It was concluded that the 3D kinematic shoulder model was appropriate for wheelchair propulsion evaluation and further investigation was required for different wheelchair types and different subject pathologies. [42]

A study by Corfman et al. examined the efficacy of a pushrim-activated power assist wheelchair (PAPAW) on upper extremity joint ROM reduction. Shoulder, elbow and wrist kinematics were calculated via bony landmark marker positions for each of the ten MWUs during wheelchair propulsion both with and without the PAPAW system. Propulsion was conducted at two speeds and three resistance levels on a dynamometer. The study revealed that the PAPAW system significantly reduced ulnar/radial deviation and flexion/extension at the wrist, elbow and shoulder (in the sagittal plane and

horizontally) joints. This reduction was observed at multiple speed and resistance combinations. For example, at the faster propulsion speed with slight resistance (1.8m/s and 30W), the shoulder ROMs decreased from 71° to 59° in flexion/extension and 77° to 57° in horizontal flexion/extension. Corfman et al. concluded that the PAPAW was able to significantly reduce UE joint ROMs during wheelchair propulsion and this may reduce the incidence of UE pain and pathology. Ultimately that would lead to longer use of manual wheelchairs, allowing the user to benefit from exercise and greater independence. [36]

Finley et al. published a study in 2004 that examined the biomechanical differences between individuals with and without UE impairment during wheelchair propulsion. The 32 subjects without UE impairment had collective average peak shoulder joint angles of 5.7° of flexion, 48.0° of extension, 19.5° of adduction and 39.7° of abduction. On average the 15 subjects with UE impairment experienced -3.7° of flexion, 45.1° of extension, 9.4° of adduction and 30.9° of abduction at the shoulder joint. Maximum shoulder flexion and abduction were significantly smaller for those with UE impairment, while maximum adduction was significantly larger for the impaired subjects. The impaired subjects exhibited higher cadence with less time of handrim contact and smaller joint ROM. Finley et al. conjectured that this may be due to motor control deficits or decreased muscle strength of the impaired subjects. Differences amongst impaired subjects with and without UE pain, as well as training effects should be evaluated in future studies. [43]

Collinger et al. described shoulder biomechanics during wheelchair propulsion of paraplegic subjects. The 61 subjects propelled their own wheelchairs at three different

speeds (self-selected, 0.9m/s and 1.8m/s) on a dynamometer. The maximum shoulder extension was 47.1, 45.9° and 47.1° for the self-selected, 0.9m/s and 1.8m/s propulsion speeds, respectively. Significant differences occurred between the 0.9 and 1.8m/s speeds. The maximum flexion angles were 23.7°, 15.6° and 27.6° for the three speeds, with statistically significant differences amongst all speeds. The shoulder joint maximum and minimum abduction angles were 52.4° and 30.5° at self-selected speed, 52.6° and 30.8° at 0.9 m/s, and 53.3° and 31.4° at 1.8m/s. Lastly, the average shoulder joint maximum and minimum internal rotations were 83.9° and 9.8° at self-selected speed, 83.1° and 15.6° at 0.9m/s, and 83.7° and 6.9° at 1.8m/s. The minimum value at 0.9 m/s was statistically different from the other two speeds. Overall, as the propulsion speed increased, the shoulder had less internal rotation and greater flexion. Additionally, the increased propulsion speed resulted in increased cadence and a larger joint ROM. As with other studies, Collinger et al. reported the shoulder joint maximal extension, abduction and internal rotation near the beginning of push phase and at a more neutral position at the end of push phase. [44]

Many studies have characterized UE kinematics during manual wheelchair propulsion; however, comparison amongst studies is difficult due to differences in modeling and angle reporting. Additionally, there has been a lot of debate on how to locate points of interest that may not be seen or reached non-invasively, such as joint centers of rotation. Many different methods have been developed to determine the location of the shoulder's glenohumeral joint center [45, 46]. In 2005, in an effort to standardize certain UE modeling tasks for easier discussion and data comparison amongst researchers, the International Society of Biomechanics (ISB) published recommendations

for UE kinematic modeling [47]. ISB is an international organization, founded in 1973 to promote biomechanics, especially of human movement. The group encourages open communication and dissemination of knowledge. [48]

Glenohumeral joint kinematics alone do not describe the entire system accurately. Raina et al. describes how shoulder joint stabilization while still allowing full 3D rotation of the humerus relative to the scapula requires coordinated movements of multiple shoulder muscles, and strength or control deficiencies of these muscles can alter the scapulohumeral rhythm and likely lead to pain and/or pathology [49]. Due to the high incidence of pain and pathology in the shoulder joint of MWUs, upper extremity kinematic models have grown in complexity to gather more information. The “shoulder joint” actually comprises three joints: glenohumeral (GH), acromioclavicular (AC) and sternoclavicular (SC). Thus the scapula and clavicle are additional segments of interest. “Proper scapular motion and stability is considered to be crucial to normal function of the shoulder.” During arm elevation, the scapula must act as stable base for proper glenohumeral joint function while also rotating in order to maintain correct glenohumeral joint alignment and optimal muscle length-tension relations [50]. One study reported that the acromioclavicular joint of the shoulder is the most susceptible to degenerative changes [51]. Shoulder impingement syndrome, described as reduced space available for the soft tissues that lay between the head of the humerus and the acromial arch of the scapula, has been reported as the most common UE pathology in MWU [52, 53]. It is the orientation of the scapula and the humerus that determine the amount of space available in this subacromial space [54]. While primarily observed during wheelchair weight relief and transfer [55] or non-wheelchair related activities [20], studies have begun to examine

the scapula and clavicle motions and the resulting AC, SC and GH joint kinematics during wheelchair propulsion.

In 1995, van der Helm et al. conducted one of the first studies aimed at quantifying the kinematics of the SC and AC joints. Van der Helm et al. acknowledge and discuss the problems with tracking scapular motion due to its subcutaneous motion. Other possible methods of scapular motion capture were listed as: x-rays of multiple humeral positions, tracking specific bony landmarks, goniometer measurements and motion capture with the use of pins inserted directly into the scapula and clavicle bones. Van der Helm et al. palpated specific bony landmarks and recorded their 3D locations using a palpator. The use of this method meant that the bony landmarks, and thus scapular and clavicular orientations, could only be recorded in static positions. Ten able bodied males were evaluated in seven different humeral elevation positions in combination with two different humeral abduction positions. An upper extremity inverse dynamics model calculated the rotations of the clavicles and scapulae, as well as the humeri and thorax. Van der Helm et. al. concluded that the motion of the scapula depends mainly on the amount of humerus elevation. Also, due to the closed-chain nature of the shoulder girdle, the clavicle simply rotates as required by scapular motion. Therefore the motion of the scapula relative to the thorax is more important than its orientation with respect to the clavicle. [21]

A similar study by Ludewig and Cook conducted semi-static testing with humeral elevations of 60°, 90° and 120°. Marker locations were palpated and rotations were calculated with the scapula relative to thorax. Three-dimensional GH and scapulothoracic (ST) kinematics were analyzed for able-bodied non-MWUs with and

without shoulder impingement symptoms. Ludewig and Cook hypothesized that subjects with impingement symptoms would experience decreased upward rotation and posterior tipping of the scapula, decreased humeral lateral rotation, and increased scapular internal rotation during humeral elevation. They determined that subjects suffering from shoulder impingement exhibited decreased upward scapula rotation and increased anterior tipping and internal rotation of the scapula. [56]

In 2004, Koontz et al. also looked at scapular kinematics in static positions. Unlike the previous studies this one was conducted specifically for MWUs. 10 subjects were each placed in 6 different static positions: -30° , -15° , 0° , 15° , 30° and 60° , according to the angle of the hand on the handrim, with zero degrees corresponding to when the hand was at top dead center of the handrim. Anatomical landmarks on scapula measured, scap hum and thorax angles calculated for each relative to the thorax. Scapula exhibited slight upward rotation (1.5°), 15° of protraction and 22° of forward tipping at the beginning of the push. As the subject progressed their hand position forward, simulating wheelchair propulsion, the scapula protraction angle increased and forward tipping decreased. [57]

Laurence et al. examined upper extremity kinematics during initial learning of wheelchair propulsion and evaluated the influence of propulsion velocity and repetition on the kinematics. Ten able-bodied people, with no wheelchair experience propelled a sports wheelchair along an 11 m pathway. The first set of trials was at a self-selected, comfortable speed, and the next set at an increased speed. Laurence et al. presented typical angular plots for the thorax, scapula-thoracic, gleno-humeral and elbow joints over a time interval containing four stroke cycles. It was determined that the angular ROM increased rapidly during initial acceleration, with steady state reached by the third

stroke cycle. As the subjects progressed through the trials, the average joint motion amplitudes increased at varying rates. Additionally, at the higher propulsion rate the average joint amplitudes were greater than at the lower propulsion rate. It appears that for both propulsion speeds, the greatest kinematic changes between the first and last trials were in scapula-thoracic elevation/depression and tilting. [37]

Morrow et al. were one of the first to investigate wheelchair propulsion in conjunction with shoulder health. Their goal was to characterize scapular kinematics during high loading periods for multiple wheelchair activities (propelling on level surface, up and down ramps and weight relief). Morrow et al. determined that during all activities the glenohumeral joint was externally rotated and the scapula was internally rotated, anteriorly tilted and slightly upwardly rotated. Similar humeral and scapular kinematic patterns were seen during level and ramp propulsion though there was a shift in the maximums and minimums due to the greater push phase time during ramp propulsion. The only dissimilarities between level and ramp propulsion were glenohumeral abduction and flexion angles. Additionally, at the time of peak loading the scapular kinematics exhibited anterior tilt and internal rotation, orientations associated with the decreased subacromial space of shoulder impingement. Morrow et al. concluded that for all activities, which are performed many times a day for MWUs, the scapula orientation causes concern for shoulder impingement syndrome development. In order to slow or prevent its onset strength training and alternative weight relief strategies are suggested. [54]

Another recent study by Raina et al. also investigated scapular kinematics during wheelchair propulsion. They hypothesized that the scapular kinematics associated with

shoulder impingement (decreased upward rotation, increased anterior tilt, etc.) will increase with greater loading demands during wheelchair propulsion. Eighteen male MWU with thoracic or cervical level SCI propelled a custom designed wheelchair on a wheelchair ergometer with resistance set to either an unloaded (level ground) or loaded (4% or 8% grade incline) condition. During the unloaded condition subjects experienced a range of motion of about 5 degrees in both the anterior/posterior and protraction-retraction directions. These ranges increased to 5-15° during the loaded condition. The upward/downward rotation range was approximately 5 degrees for both conditions. The average peak load experienced during the unloaded condition was 41 N and 101 N during the loaded conditions. At the point of peak handrim force, subjects with paraplegia experienced greater downward rotation and less retraction of the scapula during the loaded condition versus the unloaded condition. The scapula was also more anteriorly tilted during the loaded condition, though not significantly. As those with paraplegia, subjects with tetraplegia had significantly less scapula retraction during loading. Unlike those with paraplegia though, there were varying amounts of scapular upward and downward rotation at peak loading during both loading conditions. The scapular kinematics exhibited during loading are consistent with those associated with shoulder impingement. These kinematic patterns may be linked to particular muscle control issues due to subject impairment or disease. [49]

All of the previously discussed studies examined adult subjects; however, our interest lies in the pediatric population. While not related to wheelchair propulsion, Dayanidhi et al. described and compared scapular kinematics in healthy, able-bodied children and adults, hypothesizing that differences would be noted. There were a total of 29 subjects:

15 adults aged 25-45 years old and 14 children aged 4-9 years old. Subjects stood and elevated their arms in the scapular plane (40 degrees anterior to the frontal plane) along a plastic guide. Dayanidhi et al. focused on the arm elevation range from 25° to 125°, as accuracy decreases past 125°. In this range the pediatric group exhibited increasing external rotation, while the adults exhibited decreasing external rotation. As the arm elevated, both groups exhibited increases in scapular upward rotation and posterior tilt, and clavicular retraction and elevation. Significant differences between the two groups were also noted in the scapular resting position for scapular upward and external rotations and clavicular elevation. Dayanidhi et al. postulate that these differences are due to musculoskeletal development that occurs throughout adolescence and likely influences scapular stabilization and motion. Dayanidhi et al. concluded that the scapulothoracic joint had a greater contribution to arm elevation in children than adults and therapy focused on ST joint mobility and stabilization in children may improve functional outcomes. [19]

The only study the author is aware of that evaluated pediatric wheelchair kinematics was conducted by Bednarczyk et al. They studied the effects of wheelchair weight on stroke cycle kinematics in adult and pediatric MWU with SCI. They concluded that at low speed, level-ground propulsion, weight additions of 5 and 10 kg did not alter the kinematics of either group; however, the overall kinematics between the two populations were different [58].

Most of these studies were conducted with adult or non-pathological pediatric subjects and since it has been shown that differences exist between adult and pediatric populations, adult solutions cannot be assumed to work for the younger population. As

previously mentioned, there are almost 90,000 children using MW [1]. Since pathologies such as CTS and shoulder impingement develop over time the pediatric population needs to be examined before the onset of such secondary pathologies. Additionally, there are many pathologies and injuries that require manual wheelchair use amongst the pediatric population; while SCI is one of them, other pathologies should be analyzed.

1.3.3. Wheelchair Kinetics

1.3.3.1 The SmartWheel

Due to the recent development and commercialization of the SmartWheel in 2000/2001 [59], researchers are now able to study UE kinetics during wheelchair activities. The SmartWheel was designed to record the forces and moments applied by the subject to the wheel's handrim during wheelchair propulsion and other activities (see figure 1 below). The SmartWheel was first conceptualized in 1986 in order to better understand and improve wheelchair racing performance. In 1989 the first conference paper regarding the SmartWheel was presented, describing the initial design and mathematics. The first SmartWheel prototypes for a racing and standard wheelchair emerged in 1989 and 1991 respectively. The standard wheelchair prototype was the beginning of the shift in focus to understanding the biomechanics of manual wheelchair propulsion due to the high incidence of pain and pathology development. Data collection began in 1992 and 1993; however, without a wireless system design, the test set-ups required a stationary wheelchair propelled on a treadmill. Between 1994 and 1996 the A/D conversion was integrated within the SmartWheel, allowing for the use of a laptop and wireless connection. Three Rivers Holdings, LLC was created in 2000/2001 to provide technical support when the SmartWheel went commercial [59].

The SmartWheel replaces the wheelchair's current wheel on the side of interest (or one on each side). A dummy wheel replaces the wheel on the opposite side to maintain symmetry. Six strain gauges in the SmartWheel allow for the determination of the three forces and three moments applied to the handrim by the user. The 3D handrim values may then be used in inverse dynamic calculations to determine the forces and moments occurring at each upper extremity joint. Other measurements recorded or calculated by the SmartWheel system include: wheelchair speed, distance travelled, push length (in degrees), peak and average forces, and push frequency. The SmartWheel records forces and moments in a constant "global" coordinate system: the x-axis always pointing in the direction of wheelchair motion, the y-axis pointing superiorly and the z-axis always pointing laterally out of the plane of the wheelchair. If the wheelchair traverses an incline, this coordinate system will rotate in accordance with the incline. [60]



Figure 5: The SmartWheel (Outfront.com) [60]

1.3.3.2 Wheelchair Kinetics

In gait analysis, joint kinematics is only part of the picture. Through the use of force plates, ground reaction forces are obtained and used to calculate joint kinetics of the lower extremity. Instrumented wheelchair handrims or wheels, such as the SmartWheel, allow for the same ability to obtain reaction forces required for the calculation of joint

kinetics of the UE during manual wheelchair propulsion. Forces and moments occurring at the wrist, elbow and glenohumeral joints during wheelchair use have been documented; however, many of the studies evaluated wheelchair transfers [61, 62] or other wheelchair related activities [62, 63]. Fewer studies have examined UE kinetics during propulsion, and at the time of writing there are no studies that the author is aware of that have attempted to characterize UE joint kinetics during wheelchair propulsion for the pediatric population.

Boninger et al.'s 1997 study looked at wrist biomechanics of six wheelchair athletes, 5 with traumatic SCI and one with spina bifida, during wheelchair propulsion. All subjects used the same lightweight wheelchair without adjusting any settings. At the slower propulsion speed of 1.3m/s, peak forces were found to be 21.6N directed from the radial to ulnar styloid, 24.4N directed palm to dorsum and 50.9N along the superior/inferior axis in compression. During the propulsive phase there were primarily shear forces acting from the radial to ulnar styloid and from the palm to the dorsum of the hand. The largest wrist joint force was compressive and occurred throughout the stroke cycle. During the slower propulsion speed, 1.3 m/s, the average maximum moments were 10.4 Nm of extension, 16.6 Nm of ulnar deviation and 10.2 Nm of supination. During the majority of the propulsive phase, there were extension, pronation and radial deviation moments acting on the wrist, with the latter as the largest. With increased speed, the average peak extension and flexion moments increased and the average compressive force and ulnar to radial styloid shear force increased. Boninger et al. also noted that the peak forces and moments usually occurred during extreme wrist angles. [35].

A 1996 study by Robertson et al. compared the net joint forces and moments of MWUs and non-MWUs during wheelchair propulsion at a speed between 0.67 and 0.89 m/s. All subjects used the same wheelchair. The non-MWUs experienced a peak wrist moment of 2.29Nm, while the MWUs experienced a peak of 5.78Nm; not significantly different. The MWUs took longer than the non-MWUs to reach the peak net moment value. The values reported here were lower than Boninger et al., likely due to the slower propulsion speed. [64]

Finley et al. investigated the biomechanics of wheelchair propulsion between wheelchair users with and without upper extremity impairments. Subjects all used the same wheelchair, adjusted to match their personal wheelchair set-up. Propulsion was performed at 0.94 m/s on a wheelchair ergometer. Average peak wrist forces occurred as anterior shear and lateral shear for both groups, without any significant differences. Significant differences were observed along the superior/inferior axis, with the peak wrist force in compression with values of 72.0N for the un-impaired group and 49.5N for the impaired group, which was significantly different. There were also no significant differences observed among the ulnar deviation moment or the average wrist flexion/extension moments though it was interesting that the un-impaired individuals experienced a greater wrist flexion moment (11.9 Nm) than the impair group (5.7Nm). In summary, Finley et al. found that subjects with upper extremity impairment had decreased compressive wrist joint forces, while no significant differences were noted amongst the moments of the two groups. These values, with the exception of the ulnar deviation moment, appear to be comparable to Boninger et al.'s values, keeping in mind Boninger et al.'s subjects propelled at a faster speed. [43]

Desroches et al. described the 3D UE joint moments of subjects with SCI during overground wheelchair propulsion in the same non-adjustable wheelchair. Dimensionless net joint moments were reported. The peak moments were largest in extension (at 20% propulsive cycle), then ulnar deviation (at 13% cycle) and last, external rotation (at 25% cycle). 50% stroke cycle was identified as the transition point from propulsion phase to recovery phase. However, the peak wrist moments observed by Boninger et al. were in extension, radial deviation and internal rotation. These differences may be explained by the different subject groups or testing set-ups: SCI subjects propelled overground in the Desroches et al. study while Paralympic athletes propelled on a dynamometer in the Boninger et al. study. [65]

Another study, conducted by Gil-Agudo et al., investigated upper extremity kinetics among four groups of subjects with different levels of SCI: high and low paraplegia and C6 and C7 tetraplegia. The same wheelchair was used for all subjects, with the wheelchair adjusted such that each subject would have an elbow flexion value of 100 degrees. Subjects propelled on a wheelchair treadmill at 0.833 m/s. The magnitude of the superiorly directed wrist force was significantly greater in the C6 tetraplegia group than the low level paraplegia group; while the inferiorly directed wrist forces were significantly smaller for the C6 tetraplegia group than the paraplegia groups. Significant differences were also found between the tetraplegia and paraplegia groups for all peak moments in all three planes of motion, with peak ulnar deviation, pronation and flexion moments smaller for the tetraplegia group. Gil-Agudo et al. found no significant differences between the two paraplegia groups or between the two tetraplegia groups. [66]

In addition to the wrist data analyzed, Robertson et al. [64], Finley et al. [43], Gil-Agudo et al. [66], and Desroches et al. [65] also analyzed elbow joint biomechanics.

Robertson et al., who studied propulsion between able-bodied individuals and MWUs, observed that the maximum elbow moment for non-MWUs, -21.31 Nm, was significantly higher than for wheelchair users, -12.31 Nm. [64]

Finley et al., who observed subjects with and without upper limb impairments, reported average maximum elbow forces as: 50.7N of anterior shear, 42.1N of lateral shear and 50.7 N of compression in the un-impaired subject group and 46.6 N of anterior shear, 32.9 N of lateral shear and 33.3 N of compression for the impaired subjects. Additionally, the peak moments were 36.2 Nm and 30.8 Nm of elbow extension in the un-impaired and impaired subjects, respectively. The subjects with upper limb impairment had significantly reduced elbow compressive and lateral shear forces compared to the non-impaired group. [43]

Gil-Agudo et al., who investigated MWU with different levels of SCI, observed significantly greater elbow forces directed superiorly and medially in the C6 tetraplegia subjects than the paraplegia subjects. The anteriorly directed forces were significantly lower for the C6 tetraplegia subjects compared to the high level paraplegia group. Lastly, the adduction moment was significantly greater in the tetraplegia groups than the paraplegic groups. In conclusion Finley et al. state that while subjects with upper extremity impairment were able to successfully propel a manual wheelchair, their inability to produce larger forces resulted in the need to apply lower forces at an increased cadence. This may be a possible indicator of future upper extremity overuse joint pain and pathology. [66]

Desroches et al., who evaluated MWUs with SCI, reported that the highest elbow joint moment was in flexion, followed by adduction and pronation. The peak flexion and pronation moments both occurred at 10% stroke cycle, and peak adduction at 20%. Desroches et al. comment on the similarity between elbow and knee joints in their restriction of adduction/abduction movement. The passive structures responsible for stabilizing the elbow joint against adduction and abduction may increase its ability to accept higher loads. This may explain the unlikely nature of developing overuse injuries at the elbow joint during wheelchair propulsion. [65]

Compared to the wrist and elbow joints, more kinetic research has been focused on the “shoulder” joint, as a large percentage of MWU develop shoulder pain or pathology.

Robertson et al. reported the peak vertical force at the shoulder joint for non-MWUs, 81.9N was significantly larger than for MWUs, 56.9N. For both MWUs and non-MWUs amongst wrist, elbow and shoulder joints, the moments at the shoulder joint were significantly larger than at the other joints. Additionally, the non-MWUs experienced a significantly larger shoulder moment, -34.87Nm than the MWUs, -19.60 Nm. [64]

Finley et al. reported maximum shoulder joint forces as follows: 58.0 N of anterior shear, 51.9 N of tension, and 31.7 N of lateral shear in MWUs without impairment and 53.1 N of anterior shear, 47.1 N of tension and 23.2 N of lateral shear for MWUs with impairment. The maximum shoulder joint moments were reported as: 52.1 Nm of flexion and 35.2 Nm of adduction for the un-impaired group and 46.0 Nm of flexion and 27.3Nm of adduction. Therefore, while those with upper limb impairment were able to propel a manual wheelchair, they exhibited increased biomechanical variables versus subjects without impairment. [43]

Koontz et al. described shoulder joint biomechanics of 27 SCI subjects in their own wheelchairs at two different propulsion speeds, 0.9 m/s and 1.8 m/s. It was determined that the largest forces occurred during the push phase for both speeds: 90.0N and 108.2N inferiorly directed, 59.9N and 86.6N anteriorly directed and 34.0 and 50.4 N medially directed. After the peaks were reached (between 45% and 64% of the stroke cycle), the anterior force decreased becoming a posterior force at the end of push phase and the inferior force decreased to a constant value equaling the limb weight. The forces along the anterior-posterior and medial-lateral axes all became close to zero. All the peak shoulder forces were found to be significantly larger at the faster propulsion speed and occur earlier in the stroke cycle (except for the lateral force component). When evaluating shoulder joint moments, the largest moment caused shoulder flexion in the sagittal plane of 28.6 Nm at 0.9m/s and 36.5 Nm at 1.8m/s. The internal rotation moment were the next largest at 21.6Nm and 31.9Nm for each speed respectively, then the adduction moments 21.3Nm and 31.1Nm and lastly the horizontal flexion moments 10.9Nm and 21.0 Nm. At the beginning of the push phase, the GH moments were all relatively small and peaked about halfway through the push phase, except for the horizontal flexion moment which peaked close to the end of push phase. All the moments approached zero after transitioning to the recovery phase. All the peak shoulder joint moments were significantly larger at the faster propulsion speed and the adduction moment occurred earlier in the stroke cycle. In summary, Koontz et al. found differences amongst individuals in shoulder joint range of motion, peak kinetics and the point at which the peak kinetics occurred within the stroke cycle. They concluded that the association between the timing of the peak kinetics and shoulder pathology should be

investigated as it may be used to determine risk of shoulder pain and pathology development. [67]

In 2001 Kulig et al. investigated the effects of SCI level on shoulder kinetics through an evaluation of 69 males with low level or high level paraplegia and C6 or C7 tetraplegia. Subjects propelled a common wheelchair at a self-selected speed on a wheelchair ergometer simulating level surface propulsion. The kinetic patterns of the shoulder joint exhibited over the stroke cycle were similar amongst all groups. At initial contact the forces on the shoulder joint were posteriorly and inferiorly directed. Moving through the beginning of push phase the horizontal force increased posteriorly, reached its peak between 5-10% stroke cycle and remained at this level until about 20% stroke cycle. Then it rapidly decreased and became an anterior force by the end of the push phase, at 30 % stroke cycle. In recovery phase the anterior force reached its peak by 40% stroke cycle and was superiorly directed once again by 70% stroke cycle. The vertical force became superiorly directed around 10-15% of the propulsive cycle, with peak force reached at 15-19% stroke cycle. The vertical force then abruptly switched directions and reached peak inferior force soon after transitioning to recovery phase (33-37%). Kulig et al. found no significant differences in shoulder joint forces among the four levels of SCI. There were significant differences in propulsion speed, with the two tetraplegia groups propelling slower than the low level paraplegia group. Once the forces were adjusted for velocity, it was determined that the superior force was significantly greater for the C7 tetraplegia group than both paraplegia groups, and the anterior force was significantly greater for the C7 group than the C6 and high paraplegia groups. [68]

The shoulder moments at initial contact were in extension, abduction and internal rotation. The peak extension moment occurred when the hand reached the top handrim position (11% stroke cycle), then began to decrease. Just before recovery phase, the extension moment became a flexion moment, which peaked at 38-40% stroke cycle, early in the recovery phase. The peak abduction moment occurred early in the push phase and then gradually decreased to zero by the end of the push phase. The peak adduction moment occurred early in recovery phase (37-44%), and then became an abduction moment that increased slowly. In the first 5-10% of the stroke cycle the peak internal rotation moment was reached which continued throughout the push phase. In recovery phase, the moment reached a steady low value which began increasing at 90% stroke cycle. [68]

Kulig et al. discuss the impact of superior forces on subacromial structure compression, particularly when the humerus is abducted and internally rotated. They also discuss how internal rotation of the humerus increases the risk of impingement due to the close proximity of the greater tuberosity and supraspinatus tendon with the acromion. Both of these conditions occur during wheelchair propulsion and likely explain the prevalence of shoulder impingement in MWUs. Additionally it was noted that the C7 tetraplegia group experienced greatest superiorly directed shoulder joint force. Kulig et al. conjecture that this is due to the group's reduced ability to grasp. The subjects increased their effort at the end of the push phase to compensate for the inability to effectually pull up on the handrim at the beginning of propulsion. [68]

In a related study, Mercer et al. studied the relationship between joint kinetics experienced during manual wheelchair propulsion and shoulder pathologies in subjects

with paraplegia. Motion capture occurred as they propelled their wheelchairs at two different propulsion speeds (0.9 and 1.8 m/s) on a dynamometer. At the faster propulsion speed the subjects experienced higher shoulder joint forces and moments and increased cadence. Mercer et al. found that subjects with greater internal rotation and superior forces showed indications of shoulder pathology during a physical examination and MRI scan. In agreement with Kulig et al., Mercer et al. discuss superior force and internal rotation moment contribution to shoulder impingement syndrome. Particularly, the superiorly directed shoulder force as an impingement risk factor since it pushes the humerus up towards the acromion, which may compress the rotator cuff. Additionally, propelling a wheelchair with higher internal rotation moments can create an imbalance of the internal and external shoulder rotator muscles, increasing the risk of shoulder impingement. [23]

A 2008 multi-site study conducted in part by Collinger et al. also evaluated shoulder biomechanics in a paraplegia subject population during three speeds (self-selected, 0.9 and 1.8m/s) of wheelchair propulsion on a dynamometer. As with Kulig and Mercer [68, 23] significant increases in shoulder kinetics were observed at the faster propulsion speed. Body weight was determined to be a primary factor affecting joint forces though while pain increased with propulsion velocity, it had no biomechanical effect. Peak shoulder joint loading occurred with the humerus extended and internally rotated. Collinger et al. conclude that body weight management and other force reducing interventions should be implemented to reduce pain and pathology development. [44]

When evaluating shoulder biomechanics of SCI subjects, Desroches et al. found the flexion, internal rotation and abduction shoulder joint moments were the highest. Peak

moments for each plane occurred at 19%, 21% and 48% of the propulsive cycle, respectively. The shoulder incurred a flexion moment for the entire push phase, driving the arm forward, which Desroches et al. termed a propulsive configuration, while the smaller abduction and internal rotation moments provided joint stabilization. Near the end of the push phase, (about 40% stroke cycle), the shoulder primarily exhibited internal rotation and abduction moments, a stabilization configuration. Assuming the moments are created by muscle activity, Desroches et al. state that the stabilizing internal rotation moment would be a result of active rotator cuff muscles. Desroches et al. cite studies that found rotator cuff muscles to be active at a high level during wheelchair propulsion, which many believe leads to fatigue and risk of shoulder joint overuse injury. [65]

Gil-Agudo et al. evaluated 16 subjects with SCI during manual wheelchair propulsion on a treadmill at 3 and 4 km/hr. Although the shoulder joint forces and moments were lower than in similar studies (likely due to the lower friction encountered on the treadmill), they were still strongly dependent on speed, as in those studies conducted with dynamometer and ergometer. Gil-Agudo et al. discovered a peak anterior force during recovery phase that was higher than the peak posterior force noted during the push phase. They conclude that it is important to evaluate the recovery phase since different mechanical action occurs at these joints which may result in greater peaks occurring in recovery phase versus push phase. [69]

As with the inclusion of SC and AC joints in the kinematic evaluation of MWUs, the understanding of SC and AC joint kinetics would complete the biomechanical information of the shoulder joint complex. Due to the structure of the shoulder girdle, the typical inverse dynamic approach cannot be applied.

Only one study of which the author is aware has attempted to determine the AC and SC joint kinetics [70]. 17 total subjects (5 able-bodied, 8 paraplegia and 4 tetraplegia) were evaluated during one minute of wheelchair propulsion on a treadmill at 0.83 m/s, and during a vertical weight relief lift while 3D kinematics of the thorax, scapula, humerus, etc. were collected. The segment orientations as well as the applied forces and moments at the handrim were used as inputs to the Delft Shoulder and Elbow Model (a SIMM model created by van der Helm et al. [71]), which provided force and moment outputs for the GH, AC and SC joints. From the model, van Drongelen et al. calculated that the moments occurring at the SC joint are higher than the GH and AC joints. The mean forces acting on the GH joint were significantly higher than those acting on the AC and SC joints, which were less than one third those acting on the GH joint. Amongst the groups, there were no significant differences for any of the joint forces. The average net moments for all of the subjects observed were between 4.2 and 6.6 Nm with peaks between 6.7 and 10.3Nm. During wheelchair propulsion the mean and peak SC moments were significantly higher than those about the AC and GH joints, though no differences were found amongst the subject groups. Van Drongelen et al. suggested that the measure of moments about the AC and SC joints are better for loading definition at these joints. [70]

Many other studies, not described here have examined UE biomechanics during manual wheelchair activities. Weight relief and transfers performed throughout the day are also repetitive and cause high loading of the UEs. The joint kinematics and kinetics of these tasks have been evaluated [61, 62, 72]. A recent study evaluated the differences between testing MWUs on a treadmill versus overground [73]. Other studies have

examined effects of fatigue [74], wheelchair set-up [12, 13], and training programs and exercise [75, 76] on joint biomechanics. Lastly, a recent publication suggests redefining the stroke cycle to further describe the push phase [77].

Baseline studies have been completed with control subjects and non-wheelchair users [42]. Biomechanical differences during wheelchair propulsion between able-bodied individuals and those who are experienced manual wheelchair users have also been identified [78, 43]. Experienced wheelchair users show greater propulsion proficiency [78]. Additionally, although adult and pediatric anatomies differ, adult data is more prevalent in the literature [70]. This may be problematic as children have not reached musculoskeletal maturity, and may experience differences in propulsive technique. Also, the ratio of occupant weight to wheelchair weight is higher for children than adults [58], possibly altering biomechanics and effort during propulsion. Few studies have been conducted on pediatric wheelchair dynamics [19].

In order to prevent long-term pathologies, pediatric subjects should be analyzed as they are establishing their wheelchair habits and developing their musculoskeletal system. Our custom biomechanical model will accommodate pediatric manual wheelchair users. Knowledge obtained may assist in the delay or prevention of UE pathology and improve transitional care.

In order to prevent long-term pathologies, pediatric subjects should be analyzed as they are establishing their wheelchair habits and developing their musculoskeletal system. Our custom biomechanical model will accommodate manual pediatric wheelchair users. Knowledge obtained may assist in the delay or prevention of UE pathology in later life and improve transitional care.

1.4 Specific Aims

Better knowledge of upper extremity dynamics during wheelchair propulsion can improve understanding of the onset and propagation of UE pathologies. This may lead to improvements in wheelchair prescription, design, training, and long-term/transitional care. Thereby, pathology onset may be slowed or prevented, and quality of life restored.

In order to better understand and model the UE joints (wrist, elbow and shoulder) during wheelchair mobility three main goals must be accomplished:

1. Create an updated kinematic model of the upper extremity including:
additional segments, more accurate representations of segments and joint locations, consideration of ease of use in the clinical setting with children.
2. Based on the kinematic model, create the corresponding kinetic model in order to collect information about the forces and moments occurring at each joint.
3. Implement the model and collect preliminary data from children with UE pathology.

CHAPTER 2: UPPER EXTREMITY MODEL FEATURES

2.1. Previous Research / Slavens Model

The biomechanical model developed in this thesis is based on the 3D kinematic models created by Slavens et al. [79-81], in which seven total segments (thorax, humeri, forearms and hands) were represented by sixteen total anatomical landmarks. Slavens' model described the 3D kinematics of the wrist, elbow and shoulder joints, as well as the thorax. While the model proved a valuable starting point [79, 82], it did not provide joint kinetics. The model developed in this thesis includes upper extremity joint kinetics, as well as additional improvements for greater accuracy in segment and joint center representation and pediatric specific body segment parameters.

Several modifications were incorporated into this new biomechanical model for pediatric evaluation. The addition of clavicle and scapula segments was included to provide further information regarding the shoulder girdle complex. A method developed by Senk et al. was utilized to determine the positions of certain scapula markers that would otherwise prove difficult to track [83]. The marker sets of the forearm and upper arm were altered to follow a model previous developed by Hingtgen et al. [84], in order to avoid elbow marker contact/interference with the wheelchair during propulsion. The rotational center of the glenohumeral joint was located using regression equations as developed by Meskers et al. and updated by the International Shoulder Group (ISG) involving five scapular markers [45, 46]. The thorax marker set was also altered to follow work developed by Nguyen et al. for greater model accuracy [85]. Each of these modifications is discussed in detail in the following sections.

2.2. Addition of Scapula and Clavicle Segments

As discussed in the first chapter, the shoulder girdle comprises the glenohumeral, acromioclavicular (AC) and sternoclavicular (SC) joints. Due to the difficulty of tracking the scapulae and clavicles with external markers, it is common in upper extremity models to only track the glenohumeral joint by looking at the position of the humerus relative to the thorax [22, 86]. While this may be a reasonable assumption for some models, several studies have begun tracking the scapulae and clavicles in order to determine kinematics of the acromioclavicular and sternoclavicular joints [19, 20 76]. Some studies have researched the kinematics of the acromioclavicular and/or sternoclavicular joints during wheelchair activities [49, 54, 72]. By fully characterizing the joint kinematics of the shoulder girdle, a more comprehensive understanding of the complex motion that comprises shoulder movement may be gained. This knowledge may reveal specific motions at the AC or SC joints indicative of UE pain and pathology during wheelchair propulsion. Findings by some groups have shown that there are differences in scapular kinematics with increased load, which could be an indicator of shoulder impingement syndrome and pain development [49, 54]. Further research into scapular and clavicular motions may lead to propulsion modifications, strength training or other measures that could slow or prevent upper extremity injury [49, 54]. Therefore, these segments were included within the development of this model.

The scapula and clavicle segments were modeled to follow ISB recommendations as closely as possible. Markers were placed on the following bony landmarks in order to define the scapula according to ISB: trigonum spinae scapulae (the root of the scapula spine) (TS), inferior angle (AI), acromial angle (AA), and the coracoid process (CP) [47].

However, due to possible/likely TS and AI marker interaction with the wheelchair seat back, as well as a large amount of skin motion artifact at these locations, the TS and AI markers are only used during a static trial prior to the dynamic trial. A method developed by Senk et al. is then employed to determine the TS and AI locations and is described later [83]. The scapula coordinate system follows ISB recommendations [47].

The clavicle segment can only be defined by two bony landmarks, the most ventral point of the sternoclavicular joint and the most dorsal point of the acromioclavicular joint [47]. Markers were placed on both the left and right acromioclavicular joints. However, placing two markers on the sternoclavicular joints as well as on the incisura jugularis, required for the thorax segment, requires three markers placed extremely close to one another, where they may interfere with one another and be difficult to distinguish from one another at some camera angles. Therefore, instead of using the sternoclavicular joint as a marker placement point, the incisura jugularis was used to define the most medial point of both the left and right clavicles. Van der Helm et al. also used this strategy after determining that the difference in the resulting clavicle angles between marker placement on the sternoclavicular joint or the incisura jugularis was small [21]. The clavicle coordinate system then followed the ISB recommendations with the IJ marker replacing both the SC markers of the left and right sides [47].

2.3. Scapula Markers Tracking Technique

The next step was to determine how to accurately track the motions of the scapulae. The ISB recommendation is to place four markers over the following scapular landmarks: trigonum spinae (TS), inferior angle (AI), acromial angle (AA) and coracoid process (CP) and capture the 3D motions. The origin is coincident with the AA landmark

with the z-axis directed from the TS to the AA, the x-axis perpendicular to the AA, TS and AI plane, pointing forward and the y-axis perpendicular to both the x and z axes, pointing upward [47] (see Appendix 4, Figure 3). However, there are two main issues when using this method during wheelchair mobility evaluation. First, due to the low location of the TS and AI markers on the test subject's back, there is a high possibility of the wheelchair seat back either blocking the markers from the cameras or interacting with the marker and disturbing their actual location. Secondly, there is a significant amount of skin motion artifact due to the tissue covering the scapulae and obscuring the subcutaneous motion, particularly during large ranges of motions, thereby making the tracking of scapular bony landmarks difficult to do with accuracy [83].

Methods other than the optoelectronic approach of tracking the scapular motion have been validated: electromagnetic capture devices and a scapular locator/acromion method [83, 87]. Karduna et al. (2001) compared the use of both an electromagnetic tracking device and a scapular tracker for calculating scapular kinematics to results obtained from bone pins drilled into the scapular spine. Karduna found that both methods proved sufficient for capturing the motion patterns, specifically when the arm elevation is below 120 degrees. However, the scapula tracker method has lower root mean squared (RMS) errors for scapular posterior tilting and external rotation as well as much lower maximum RMS errors within single subjects for scapular posterior tilting and external rotation. The electromagnetic method appeared to only be superior, with lower rms errors, during scapular upward rotations. In the end, Karduna postulates that in a static environment, palpating the scapular bony landmarks may provide greater accuracy of scapular motion, though its accuracy had of yet not been studied. [87]

In order to more accurately determine the location of all the ISB required landmarks using an optoelectronic motion capture system Senk et al. [83] developed a new method “merging” the electromagnetic and tracker methods. The electromagnetic method was represented by the acromioclavicular (AC) and AA landmarks; however, three non-co-linear markers are required to represent a segment for the optoelectronic method, therefore an additional marker was placed on the scapular spine (SS), as done with the tracker method, halfway between the TS and AA markers. Thus the scapula segments are represented, like the other upper extremity bone segments, by three non-colinear markers: the AC, AA and SS markers. From the position and orientation of these scapular markers, the positions of the TS and AI markers can be determined at any point in time using rigid body dynamics. Rigid body theory basically states that the relationship between two points on a non-deformable body remains constant with time and movement of the body. Additionally, the coordinates of any one point of the rigid body in one position, P_1 can be related to the coordinates of that same point of the rigid body in a successive position, P_2 , by the following equation:

$$P_2 = RP_1 + t \quad (1)$$

where R and t represent the rotation matrix and translation vector of the rigid body [88-Cheze]. Senk used this principle to determine where the positions of the TS and AI markers would be during a dynamic trial based on position and orientation knowledge of the AA, AC and SS markers. [83]

In order to accurately use rigid body dynamics the assumption of body rigidity needs to be reasonable. For the purpose of motion analysis, the assumption of rigid bone segments is reasonable; however, due to skin motion artifact, etc. the bony landmark

markers representing the bone segment do not maintain constant a rigid shape, resulting in less accurate rigid body dynamics [88]. In order to rectify the problem, a trajectory correction procedure is commonly used [83, 88]. These procedures replace the three (or more) measured marker coordinates that represent the bone segment with solidified marker coordinates that maintain a rigid shape. While there are multiple procedures used to achieve this, the method used by Senk et al. to solidify the three scapular markers (AA, AC and SS) was an un-weighted least squares algorithm, as described by Veldpaus et al. [83, 89]. This algorithm minimized the least-square difference between the measured vectors of the AA, AC and SS markers and the proposed AA, AC and SS marker vectors comprising the scapular solid [89].

Markers were placed on the palpated locations of the TS and AI, as well as the AA, AC and SS, while the subject was in anatomical position. A static trial was performed with the optoelectronic system to capture the position of all of these points. Next a coordinate system is created using the AA, AC and SS markers (the scapular solid) and the position and orientation of the TS and AI markers relative to this coordinate system are determined. Since the scapulae are assumed to be non-deformable solids, as are all modeled bone segments, the position and orientation of the TS and AI relative to the scapular solid are constant for all time. This principle allows for the removal of the TS and AI markers during dynamic motion and their positions to be calculated based upon the position and orientation of the scapular solid. A simple mathematical equation may be applied to determine the TS and AI marker locations during the dynamic trial based upon the information obtained during the static trial and

the dynamic trial locations of the AA, AC and SS markers. The equation presented by Senk et al. follows [83]:

$$[C_O M]_{NEW} = [{}^O_S T]_{NEW} \times [{}^O_S T]_{STAT}^{-1} \times [C_O M]_{STAT} \quad (2)$$

Where $[{}^O_S T]_{NEW}$ represents the homogeneous matrix containing position and orientation of the scapular solid in the new position, $[{}^O_S T]_{STAT}^{-1}$ represents the inverse of the homogeneous matrix containing the reference position and orientation of the scapular solid in the initial position, and $[C_O M]_{STAT}$ and $[C_O M]_{NEW}$ represent the global coordinates of the marker M in the reference position and the new position, respectively [83].

Senk et al. then examined the scapula in multiple static arm positions and compared the calculated TS and AI positions, as determined through his new method, to TS and AI marker positions unmoved from the original palpated positions (as done during motion analysis), and to TS and AI marker positions palpated at each static location. The results showed that the average distance between the calculated TS, AI positions and the re-palpated TS, AI position was half that of the average distance between the originally palpated TS, AI marker positions and the re-palpated TS, AI marker positions. Additionally, Senk found low RMS errors for their recalculation optoelectronic method, similar to those presented by Karduna [87] for the electromagnetic acromion approach and the tracker approach. Thus suggesting this method is valid for tracking the three-dimensional motions of the scapula [83].

The method created by Senk et al. was determined to be appropriate for studying scapular kinematics for wheelchair users for the following reasons: arm elevation remains below the controversial 120 degree position; the TS and AI markers do not need to be

present during the dynamic trial, where blocking or interference could disturb the accuracy of the results; and the optoelectronic system may be utilized, all without compromising data accuracy. [83]

2.4. Body Segment Parameters

In order to determine the joint kinematics and kinetics, an inverse dynamics model was created, in which the motion of interest is fully defined and used to determine the forces and moments responsible for causing that motion. This method models the body as a chain of rigid body segments, often referred to as the link-segment model. The link-segment model makes the following assumptions: 1. Each segment has a constant mass located at its center of mass, 2. COM location, mass moments of inertia, and segment lengths remain constant during motion, 3. Joints are modeled as either hinge or ball and socket (spherical) joints [90]. In order to implement this model the following data must be known or collected: anthropometric measurements, kinematic information, and the external forces [90, 91] (here specifically the reaction forces recorded by the SmartWheel). Accuracy of this data will directly affect the accuracy of the resulting calculations of joint forces and moments [92, 93] however the specific influence of the anthropometric information on the resulting kinetic data is somewhat controversial [93]. The anthropometric data required by the Newton-Euler equations (detailed in Chapter 3) include: segment mass, segment center of mass location, segment mass moment of inertia, and the location of joint centers. These values must either be directly measured or determined through an estimation technique [90]. Since live subjects are usually used for motion analysis, directly measuring the anthropometric data is not possible. Instead there are a few, commonly used methodological categories that may be explored:

cadaver-specific techniques, volumetric and geometric modeling techniques, medical imaging techniques [93, 94] and predictive techniques [95, 96]. The three most notable names in cadaver based body segment parameter determination are Dempster, Clauser and Chandler. Each dissected a small sample size of adult male cadavers into segments to analyze segment properties; however, Clauser pointed out that due to the small sample sizes, the resulting regression equations should not be applied to the general public [97, 98, 99]. However, many studies have used their data by “matching” their subject to the cadaver subject, or scaling the cadaver data to more closely approximate the test subject. Among other reasons that make the cadaver data inaccurate and inappropriate for use here, the cadaver data does not match our pediatric subject population. Also, due to constant non-uniform growth trends in the children segments, the work by Jensen et al. (1986) shows that simple scaling of adult data is inaccurate for the pediatric population [95].

Additionally, the volumetric and geometric techniques, which typically involve determining segment volume by incrementally submerging the segments of interest in water and/or approximating limb shape as common geometric figure with a few simple subject measurements are usually expensive, time-consuming and require either a uniform density assumption or a complex model [94]. Also, most medical imaging techniques (CT scanning, dual energy X-ray absorptiometry and MRI scanning), include some or all of the following complications: expense, provide only 2-D views, high levels of radiation, time-consuming and limited availability in the clinical setting [94]. All of these methods were thus rejected due to the pediatric subject population, time and expense.

It was determined that predictive techniques, namely regression equations developed based upon data from a similar population to predict the body segment parameters were the best option. Much work has been done by Jensen et al. to research the body segment parameters of children, who states that the “in the case of children and adolescents the commonly used parameters based on cadaver studies do not apply due to the changes in proportions which occur with growth” [100]. As body segment size and shape is altered as a child grows [101], Jensen et al. chose to examine the effects that growth had on segment mass, center of mass location, moments of inertia, etc., from the ages of 4 to 20 years old in a 9 year study [100]. Jensen et al. determined that there were developmental trends in segment mass, center of mass locations and moments of inertia, in which simply scaling adult proportion data is inappropriate [100]. For example, Jensen et al. found that the head mass proportion began around 20% and decreased to 6.8% around the age of 16, when the growth effects no longer result in differences between the adolescent and the adult head mass proportions [100]. From the data collected, Jensen et al. derived polynomial regression equations based on age (in years) to more accurately determine the segment mass and segment center of mass location proportions. The equations used in this model for the hand, forearm and upper arm are listed below [100].

The equations for the mass of the hand (H), forearm (FA) and upper arm (UA) provide the proportion of the segment mass to the entire body mass, which then multiplied by the body mass results in the mass of the individual segment.

$$UA_{mass} = (0.02344 + 0.00069558 * AGE) * W \quad (3)$$

$$FA_{mass} = (0.01340 + 0.00031268 * AGE) * W \quad (4)$$

$$H_{mass} = (0.00880) * W \quad (5)$$

Where AGE is in years (4-20) and W is the subject's weight. The units for weight are up to the user, as the regression equations provided calculated a percentage.

Jensen et al. also developed polynomial regression equations based on age for the calculation of center of mass location. The equations provide the distance from the proximal joint to the mass center as a proportion of the segment length. The equations for center of mass of the hand, forearm and upper arm follow:

$$UA_{COM} = (0.44180) * (UA_{length}) \quad (6)$$

$$FA_{COM} = (0.43223 - 0.00092718 * AGE) * (FA_{length}) \quad (7)$$

$$H_{COM} = (0.40850) * (H_{length}) \quad (8)$$

Where $SEGMENT_{COM}$ is the length from the proximal joint to the center of mass of the segment, AGE is the subject age in years and $SEGMENT_{length}$ is the length of the segment from proximal joint center to distal joint center. It is notable that for these three segments only the forearm is dependent upon the age of the subject [100].

Jensen also developed polynomial regression equations for calculating the principal moments of inertia with age once again as the independent variable. However, it was noted that there were considerable differences amongst subjects in their individual growth patterns of the principal moments of inertia, especially after 10 years of age. Therefore it was recommended to not use regression equations with age as the variable [102]. Therefore an approach developed by Yeadon and Morlock was chosen [96]. Yeadon and Morlock chose to investigate the differences in segmental moments of inertia estimates between linear regression equations and non-linear equations, based upon data provided by Chandler et al. [99]. Yeadon and Morlock postulated that the non-linear equations would still be appropriate for populations that differ from Chandler's cadavers

since the equations geometrically modeled the body segments, though segmental densities and segmental shape should be comparable between the populations. They cite Jensen's work in that the radius of gyration to segment length ratio remained relatively constant between boys 4 to 15 year of age. The results showed average standard error estimates of 21% for the linear equations and 13% for the non-linear equations. Additionally, in order to test the equation sets for an individual outside of the sample population range of Chandler's subjects, anthropometric measurements of a 10 year old boy were used to determine the segmental moments of inertia using the inertia model of Yeadon [96], which were then compared to the linear and non-linear equations estimates. The average percentage residuals from these estimates were 286% for the linear equations and 20% for the non-linear equations, leading Yeadon and Morlock to conclude that the non-linear equations are a viable and preferable option to the linear regression equations, even for subject populations that do not match Chandler's cadaver population. The non-linear equations provided by Yeadon and Morlock for determination of segmental moments of inertia were used for this model, but are too extensive to list here, see Appendix 1 [96].

At this time it was determined that the above equations provided the most safe, time and cost effective and accurate manner for determining the body segment parameters for the pediatric population.

2.5. Locations of Joint Centers

2.5.1 Elbow Joint Center

Many upper extremity marker sets include the bony landmarks of the medial and lateral epicondyles of the distal humerus in order to define the humerus and forearm

segments [39, 49, 50, 63, 65, 76, 87, 103, 105]. However, some studies have placed markers only on the lateral epicondyles [41, 44] and still others have used both the lateral epicondyles and the olecranons as marker placement sites [33, 36]. Additionally many models define the elbow joint center as the midpoint of the epicondyle markers [39, 63, 103, 104, 105], as is ISB recommended [47]. However, there is some concern of medial epicondyle marker interaction with the wheelchair during subject propulsion, and other wheelchair tasks or activities. Therefore, it was decided to alter the marker set and remove the medial and lateral epicondyle markers and replace them with one marker on the olecranon, and then determine the location of the elbow joint center based on the olecranon marker location.

Rab et al. and Hingtgen et al. both placed markers on the olecranons instead of the medial and lateral epicondyles [84, 86], although different offset values from the olecranon marker to the elbow joint center were used. Hingtgen et al. calculated the elbow joint center as anterior to the olecranon marker by a distance of half the width of the elbow in the anterior posterior direction [84]. Rab et al. calculated offset values as a fraction of the forearm segment length. Forearm length was defined as the distance between the olecranon and ulnar styloid markers. The offset values located the elbow joint center as 6% anterior and 13% superior of the olecranon, based upon measurements of one normal adult male [86], which does not match the pediatric subject population of interest for the new model developed in this thesis. As discussed by Jensen et al., there are significant differences between child and adult measurements as well as differences within a single child during growth [95, 100, 102].

Striffling et al., who studied the kinematics and kinetics of children using walkers, also used the olecranon marker when determining elbow joint center. Striffling et al. defined the elbow joint center as anterior of the olecranon marker by an offset equal to half of the sum of the marker and elbow diameters. [106]

It was decided to use a method previously presented and used by Hingtgen et al. who were studying the upper extremity kinematics of a pathologic pediatric population. Here, the elbow joint center is determined to be located anterior of the olecranon by a distance of half the measurement of elbow's anterior-posterior width [84].

2.5.2 Glenohumeral Joint Center

There are currently multiple methods used to model the location of the glenohumeral joint center. While some of them are very simple and easy to apply, they are not thoroughly validated and do not follow the recommendations of the ISB [45]. Campbell et al. recently sought to determine and compare the accuracy of these well-established methods as well propose two new predictive methods. The methods Campbell chose for comparison include: the 7 cm drop method [107], the two Vicon standard method versions, the UWA (University of Western Australia) method [105], and the original and updated ISB recommended regression equation methods [46, 47]. Schmidt et al. used a ruler to determine the average distance between the acromion marker and the shoulder joint center. The shoulder joint center was then assumed to be inferior to the acromion marker by the 7 cm average [107]. Vicon (Vicon Oxford Metrics, Inc.) developed two methods similar to that of Schmidt for glenohumeral joint center determination. The first method takes a two dimensional measurement of the distance between the acromioclavicular joint and the glenohumeral joint and subtracts this amount from the

AC joint location. The second Vicon method measures the two dimensional shoulder width and subtracts half of this value from the AC joint location [45]. The UWA method uses markers placed on shoulder to represent the anterior and posterior portion of the glenohumeral joint. Lloyd et al. then used the point halfway between these markers to designate the glenohumeral joint center [105]. Campbell et al. uses the intersection of the vector between these markers and a vector perpendicular to it from the center of the acromial lateral ridge [45]. The last method(s) included in Campbell's investigation are the original predictive method as developed by Meskers et al. [46] and an updated version put forth by the International Shoulder Group (ISG). Both methods require the use of multiple scapula marker locations in three regression equations to determine the glenohumeral joint location [45]. Meskers et al.'s original equations that were developed used the positions of the acromioclavicular, trigonum spinae, inferior angle, acromial angle and coracoid process of 36 sets of cadaver scapulae and humeri. The location of the glenohumeral joint center was then estimated using a sphere fitting technique. The three dimensional positions of the scapular bony landmarks, as well as all 10 distances between the markers were then used as potential variables in the linear regression model to predict the estimated location of the glenohumeral joint center. The resulting regression equations determine the x, y and z location of the glenohumeral joint center in the scapula coordinate system defined by Meskers as: x-axis from the TS to the AC; z-axis perpendicular to the plane formed by the AC, TS and AI markers, pointing backwards; y-axis perpendicular to the x and z axes, pointing upwards.

The regression equations follow:

$$GH_{Cxl} = 18.9743 + 0.2434(m_{CPx}) + 0.2341(m_{AIx}) + 0.1590(m_{AI} - m_{AA}) + 0.0558(m_{CPy}) \quad (9)$$

$$GH_{Cyl} = -3.8791 - 0.3940(m_{AC} - m_{AA}) + 0.1732(m_{CPy}) + 0.1205(m_{AIx}) - 0.1002(m_{AC} - m_{CP}) \quad (10)$$

$$GH_{Czl} = 9.2629 + 1.0255(m_{CPz}) - 0.2403(m_{PCy}) + 0.1720(m_{TS} - m_{CP}) \quad (11)$$

Where GH_{Cxl} is the x-coordinate of the glenohumeral joint center in the local scapular coordinate system, $\bar{m}_{markerx}$ is the denoted axis coordinate of the specified marker and $(m_{marker1} - m_{marker2})$ is the Euclidean distance (ED, equation below) between marker 1 and marker 2.

$$ED = \sqrt{(x_1 - x_2)^2 + (y_1 - y_2)^2 + (z_1 - z_2)^2} \quad (12)$$

The resulting low fitting and validation errors led Meskers et al. to conclude that this model adequately predicts the location of the glenohumeral joint center for upper arm coordinate system creation [46]. Lastly, Campbell included the amended version of Meskers regression equations by the ISG. They proposed the following regression equations:

$$GH_{Cxl} = 26.896 + 0.614(m_{TSx}) + 0.295(m_{AI} - m_{CP}) \quad (13)$$

$$GH_{Cyl} = -16.307 + 0.825(m_{ACy}) + 0.293(m_{CPz}) \quad (14)$$

$$GH_{Czl} = -1.740 - 0.899(m_{AA} - m_{CP}) - 0.229(m_{TSx}) \quad (15)$$

Additionally, Campbell et al. sought to create two new predictive methods to compare to these six established methods. First, a new regression model was created based on the following five possible predictive variables: subject height, subject mass, the Euclidean distance between the IJ and C7, the Euclidean distance between the midpoint

of the lateral ridge of the acromial plateau and the midpoint of the IJ and C7 markers, and lastly the Euclidean distance between a marker on the anterior portion of the shoulder and a marker on the posterior portion of the shoulder (in line with the glenohumeral joint).

The stepwise linear regression provided the following three equations: [45]

$$GH_{Cx} = 96.2 - 0.302(m_{IJ} - m_{C7}) - 0.364(\text{subject height}) + 0.385(\text{subject mass}) \quad (16)$$

$$GH_{Cy} = -66.32 + 0.30(m_{IJ} - m_{C7}) - 0.432(\text{subject mass}) \quad (17)$$

$$GH_{Cz} = 66.468 - 0.531(m_{AcRLR} - m_{CP}) + 0.571(\text{subject mass}) \quad (18)$$

Where GH_{Cx} is the x-coordinate of the glenohumeral joint center location with respect to an acromion reference technical coordinate system (TCS), $(m_{marker1} - m_{marker2})$ is the Euclidean distance between marker 1 and marker 2 (in mm), the subject height is in cm and the subject mass is in kg. Secondly, Campbell et al. created a three dimensional simple offset method, also relative to the acromion reference TCS, based on the average MRI glenohumeral joint locations of the participants. The resulting x, y, and z offsets were 12, -49, and 6 mm, respectively. [45]

All methods were then applied to the test subjects with the resulting estimated glenohumeral joint locations compared to the MRI determined glenohumeral joint location. It was determined that the 2 dimensional offset methods (Vicon 1, Vicon 2 and 7 cm offset) were significantly less accurate than the other three dimensionally based methods (Scapula 1, Scapula 2 and UWA), with average error between the method calculated glenohumeral joint location and the MRI glenohumeral joint location of 45, 46 and 50 mm compared to 32, 16 and 14 mm respectively. Additionally it was noted the Meskers' original regression equations were significantly less accurate than the ISG

updated equations and the UWA method. Lastly, Campbell reported the error of the new regression model and the new simple three-dimensional offset method and found errors of 13 and 12 mm respectively. Both of Campbell's methods therefore slightly outperforming the two best established methods: the UWA offset method and the ISG updated version of Meskers' regression equations. Though Campbell does point out the 3D generic offset method is most dependent upon subject population and therefore less desirable than the regression models. [45]

Based upon this study by Campbell et al., it was decided to use the regression equations updated by ISG for this model. The accuracy of the ISG regression equations is not significantly different from the UWA and Campbell methods and the required marker set concurs well with the markers required to track the scapulae and clavicles. Additionally, Campbell's method would require the use of an acromion triad, which would have to be replicated. At this point the ISG updated version of Meskers' regression equations for determination of the glenohumeral joint center location was chosen to be simplest to employ while still providing a validated accurate outcome.

2.6. Thorax Kinematics

A study by Nguyen et al. [85] compared the differences in resulting joint angles when modeling the thorax with markers placed on landmarks either directly on the thorax or indirectly on the shoulder girdle. Since many clinically used models have indirectly placed markers, Nguyen et al. suggest quantifying how the shoulder girdle movements relative to the thorax affect the accuracy of the thorax measurements. Additionally, as the order of rotation has been shown by many previous studies to result in large angular differences of other joints, Nguyen et al. explored the effects of rotation order on the

resulting thorax orientation angles. Nguyen et al. specifically studied the effects of modeling and rotation sequence on thorax kinematics during gait in the pediatric population with myelomeningocele. Usually the thorax angles are expressed with the same rotation order as the limb joints: flexion/extension, lateral bending and axial rotation; however, a new rotation order for the pelvis was proposed by Baker et al. (2001) [108] that claimed to be more consistent with clinical terminology. Baker et al.'s sequence was: rotation (transverse plane), followed by obliquity (coronal plane) and then tilt (sagittal plane), which Nguyen et al. compares to the “conventional” sequence. Markers were placed on the following bony landmarks of each subject: the midpoints of each the left and right clavicles (C_L and C_R), the seventh cervical vertebra ($C7$) and the xiphoid process (or sternal notch, STRN). The markers on each of the clavicle midpoints are then averaged to find their midpoint, C_{mid} . For both the indirect and direct models, the origin was located at the midpoint of $C7$ and C_{mid} . The axes of the indirect model were defined as: lateral axis from C_R to C_L , anterior axis perpendicular to the lateral axis and passing through the origin in the plane containing C_R , C_L , and $C7$, proximal axis perpendicular to the lateral and anterior axes. The axes of the direct model were defined as: anterior axis from $C7$ to C_{mid} , proximal axis perpendicular to the anterior axis and passing through the origin in the plane containing C_{mid} , $C7$, and STRN, lateral axis perpendicular to the anterior and proximal axes. For each subject the thorax angles were calculated using each modeling method in combination with each rotation sequence, for a total of four different thorax angle results. Nguyen et al. concludes that changing the model produced greater differences in thorax angles than changing the rotation sequence. While the changing the modeling method resulted in angular changes of less than 5

degrees in the sagittal plane, the maximum offsets in the coronal and transverse planes are greater than 10 degrees and approximately 5 degrees, respectively. When comparing the effects of rotation sequence, it was determined that changing the rotation order results in about 6 degrees of difference in all three planes. It is explained that the difference between Nguyen et al.'s thoracic rotation order and Baker et al.'s pelvic rotation order is which axis is defined as primary. Nguyen et al. defines the proximal-distal axis as primary, as is custom with the long bones of the extremities. Baker et al.'s primary axis is the medio-lateral axis, which is more appropriate for the orientation and function of the pelvis relative to the legs. Therefore, Nguyen et al. recommends that the conventional sequence of flexion/extension, lateral bending and transverse rotation be used as the thorax rotation sequence. Nguyen et al. further suggests that while the four markers of the direct method were chosen since they are regularly used in their laboratory; future models should only place markers directly on the thorax in order to eliminate shoulder movement effects entirely. [85]

Based upon Nguyen et al.'s conclusions, it was decided to use a direct method of marker placement when designing the thorax marker set, to reduce the impact/influence of the shoulder girdle on the thorax kinematics. While Nguyen et al. used markers on each of clavicles, which were then averaged to a midpoint that was used for axes definitions; this process was simply replaced with marker located on the IJ. This approximates the same general location as Nguyen et al.'s averaged clavicle midpoint but removes all influence of the shoulder girdle and reduces the total number of markers for the model since the IJ marker is already being used. [85]

The thorax coordinate system was then created using only the IJ, C7 and STRN markers. In order to do so a temporary coordinate system had to be created first in order to create a point located laterally to the plane of these three markers. The origin of the temporary CS was located at the sternum; the temporary y-axis was superior from the STRN to the C7; the temporary z-axis was a vector perpendicular to the plane containing the IJ, C7 and STRN markers, pointing laterally right; and the temporary x-axis was perpendicular to the temporary y and z-axes. The origin of the thorax coordinate system was located at the midpoint between the IJ and C7 markers. A temporary point is then created 10 units from this origin along the temporary z-axis, so it is located perpendicularly to the right of the plane created by the IJ, C7 and STRN markers. The thorax coordinate system could then be defined as follows: x-axis anterior from C7 to IJ; y-axis is created by crossing a vector pointing laterally from the thorax origin to the temporary point with the anteriorly directed x-axis, resulting in a superiorly pointing y-axis; lastly the z-axis is perpendicular to both the x and y axes.

While this thorax coordinate system definition does not perfectly match the ISB recommendation since the marker on the eighth thoracic vertebra cannot be used with many wheelchair backs, it is much closer to the ISB recommended method than those that incorporate the use of shoulder girdle markers (such as clavicles or acromioclavicular joints). Thus, this method is deemed acceptable for the research for which this model is being developed.

CHAPTER 3: BIOMECHANICAL MODEL OF PEDIATRIC UPPER EXTREMITY DYNAMICS DURING WHEELCHAIR MOBILITY

A version of this chapter is planned for submission to a professional journal.

3.1 Introduction / Model Aims

While biomechanical modeling of the lower extremity is well established with standard marker sets/models such as the Helen Hayes and Cleveland Clinic [110], this is not the case for upper extremity (UE) joint modeling. Although more and more work requiring upper extremity modeling is being conducted, there are no current standard marker sets established for UE. This is likely partially due to the wide array of UE tasks being studied and the need for custom marker sets in order to accurately represent these motions. However, steps have been made by many to improve the accuracy and repeatability of UE model design. The International Society of Biomechanics (ISB) has provided recommendations on UE modeling, in hopes to make data analysis and comparison more accurate across studies.

The UE model developed here was designed specifically to evaluate children during wheelchair mobility. Recommendations from ISB, and other research, were incorporated to meet the specific needs of this model.

Pain and pathology have been shown to be prevalent in 30-73% of manual wheelchair users. These issues reduce an individual's independence and quality of life. If the UE problems persist, instead of being able to use a manual wheelchair, the patient may require the use of an electric wheelchair, which decreases the individual's daily exercise, further decreasing the quality of life. For individuals who use manual

wheelchairs regularly at a young age, development of upper extremity pain and pathologies could occur as early as in their twenties. In order to help prevent or reduce the development of pain and pathology, a greater understanding of the UE joint biomechanics during wheelchair mobility is required. While many studies have quantified UE kinematics during wheelchair mobility of adult wheelchair users, few have observed the UE joint kinematics or kinetics during pediatric manual wheelchair use.

Therefore, the focus of this research is the design and application of a three dimensional UE biomechanical model for the evaluation of pediatric manual wheelchair mobility. The model will be used to analyze multiple pediatric pathologies resulting in manual wheelchair use, including: spina bifida, spinal cord injury, cerebral palsy and osteogenesis imperfecta. The model is capable of quantifying UE joint angular data as well as joint forces and moments during manual wheelchair propulsion. The knowledge gained may help advance wheelchair prescription, propulsion techniques, treatment and long term care within the pediatric population.

3.2 Methods

3.2.1 Kinematic Model

The kinematic model was adapted and modified from previous work done by Slavens et al. [82], whose model consisted of a wheelchair segment and 7 rigid body segments for kinematic evaluation of the wrist, elbow and glenohumeral joints bilaterally as well as the thorax. Many alterations were made in order to increase data accuracy, obtain kinematic information for more joints and obtain kinetic data for the pediatric population. Four additional segments and four additional joints were added to the model including: left and right clavicles and scapulae and the left and right acromioclavicular and sternoclavicular

joints. The determination of the location of the shoulder (glenohumeral) joint center of rotation was altered for greater accuracy [45]. Also, the markers used at the elbow joint were modified, following work previously validated by Hingtgen et al. [84], in order to avoid elbow marker contact with the wheelchair during mobility. Additionally, the thorax segment was modeled based upon Nguyen et al.'s work with children with MM, in which a more direct method of analyzing thorax kinematics was developed in order to reduce the effects of shoulder movement [85]. Lastly, body segment parameters were determined through the use of regression equations developed specifically for the pediatric population by Jensen et al. [95, 100, 102].

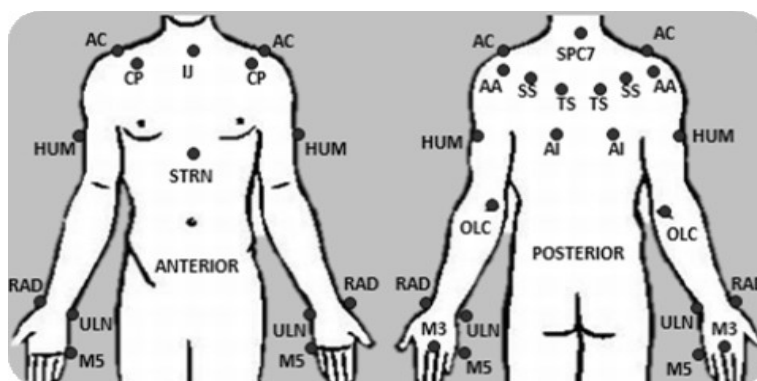


Figure 6: UE model marker set. Corresponding bony landmarks and marker names are described in Table 1.

The upper extremities were modeled using eleven rigid body segments: thorax, clavicles, scapulae, upper arms, forearms and hands. The bilateral joints of interest include: sternoclavicular, acromioclavicular, glenohumeral, elbow and wrist. Twenty-seven reflective, passive markers were placed on bony anatomical landmarks and specific reference points to represent the segments of interest (see Figure 6 and Table 1). The wheelchair was also modeled as one rigid segment by four markers as well as one marker

on the SmartWheel hub. Joint centers were calculated using subject specific anthropometric data and the related markers, with joint axes embedded at this point.

Segment and joint coordinate axes followed ISB recommendations: X-axis anterior, Y-axis superior and Z-axis laterally to the right [47]. All joints were assumed to have fixed centers of rotation. Z-X-Y Euler angle rotation sequences were used to determine segment rotations, with the distal coordinate system defined with respect to the proximal coordinate system. The upper arm and the scapula were also defined with respect to the thorax in order to more accurately compare results to current literature. The thorax and wheelchair were defined with respect to the global coordinate system. Matlab (MathWorks, Inc., Massachusetts, USA) was used for model development.

Table1. Upper extremity kinematic model segments and corresponding marker names and locations.

Segment	Marker (\bar{m}_{NAME})	Marker Location
Thorax	SPC7	Spinal process, C7
	STRN	Sternum, xiphoid process
	IJ	Incisura jugularis (suprasternal notch)
Clavicle	IJ	Incisura jugularis (suprasternal notch)
	AC (R/L)	Acromioclavicular Joint
Scapula	AC (R/L)	Acromioclavicular Joint
	AA (R/L)	Acromial Angle
	SS (R/L)	Scapular Spine, halfway between AC and AA
	TS (R/L)	Trigonum Spine (Static Only)
	AI (R/L)	Inferior Angle (Static Only)
	CP (R/L)	Coracoid Process
Upper Arm	HUM (R/L)	Humerus technical marker
	OLC (R/L)	Olecranon
Forearm	OLC (R/L)	Olecranon
	RAD (R/L)	Radial Styloid
	ULN (R/L)	Ulnar Styloid
Hand	RAD (R/L)	Radial Styloid
	ULN (R/L)	Ulnar Styloid
	M3 (R/L)	Third Metacarpal
	M5 (R/L)	Fifth Metacarpal

3.2.1.1 Joint Centers

Determining the location of the joint centers is the next step in defining the model. The positions of the joint centers are the origins for the local coordinate systems for all of the segments except the scapulae.

Thorax:

A study done by Nguyen et al. analyzing pediatric thorax kinematics was the basis for the thorax model. Nguyen et al. defined thorax movement via four markers: one at the “mid-point” of each clavicle bone, the spinous process C7 and the xiphoid process. The thorax center was calculated as the halfway point between the C7 marker and the middle of the two clavicle markers [85]. However, in order to reduce the total number of markers in this model, while still incorporating Nguyen’s direct method of thorax tracking, the IJ marker was used in place of both the clavicle markers. The thorax center was then determined as the halfway point between the IJ and C7 markers.

$$\bar{t}_c = \frac{(\bar{m}_{IJ} + \bar{m}_{C7})}{2} \quad (19)$$

Where \bar{t}_c represents the thorax joint center location and $\bar{m}_{\text{subscript}}$ refers to the marker from Table #. All markers and joint centers were composed of three dimensional coordinates (X, Y and Z) in the global reference frame.

Sternoclavicular Joint:

Both SC joints were represented by the IJ marker.

Acromioclavicular Joint:

The AC joints were represented by the AA markers.

Glenohumeral Joint:

The glenohumeral joint was modeled as a ball and socket joint without joint center translation. The joint center was located through the use of regression equations developed by Meskers et al. [46]. These equations require the coordinates of 5 scapular markers: AC, TS, AI, AA and CP. The marker locations in the global coordinate system were translated and rotated to a coordinate system fixed to the scapula, defined as:

Origin: AC

$$\bar{s}_x: \frac{\bar{m}_{AC} - \bar{m}_{TS}}{\|\bar{m}_{AC} - \bar{m}_{TS}\|} \quad (20)$$

$$\bar{s}_z: \text{perpendicular to the plane containing AC, TS and AI, pointing posteriorly} \quad (21)$$

$$\bar{s}_y: \bar{s}_z \times \bar{s}_x \quad (22)$$

The following regressions equations were then applied to determine the location of the glenohumeral joint center, as discussed in the previous chapter:

$$GH_{Cx} = 18.9743 + 0.2434(\bar{m}_{CPx}) + 0.2341(\bar{m}_{AIx}) + 0.1590(\bar{m}_{AI} - \bar{m}_{AA}) + 0.0558(\bar{m}_{CPy}) \quad (23)$$

$$GH_{Cy} = -3.8791 - 0.3940(\bar{m}_{AC} - \bar{m}_{AA}) + 0.1732(\bar{m}_{CPy}) + 0.1205(\bar{m}_{AIx}) - 0.1002(\bar{m}_{AC} - \bar{m}_{CP}) \quad (24)$$

$$GH_{Cz} = 9.2629 + 1.0255(\bar{m}_{CPz}) - 0.2403(\bar{m}_{PCy}) + 0.1720(\bar{m}_{TS} - \bar{m}_{CP}) \quad (25)$$

The glenohumeral joint center coordinates in the local scapula coordinate system were then transformed back to the global coordinate system.

Elbow Joint:

The elbow joint center was assumed to be located anterior to the olecranon process, at half the width of the elbow. An offset measurement, e_{offset} , summing half the width of the elbow and half the marker diameter was used.

$$e_{offset} = \frac{1}{2}(w + d) \quad (26)$$

Where w is the elbow width and d is the marker diameter.

A temporary axis was set up to determine the position of the elbow joint center as such:

Origin: olecranon marker

$$\bar{e}_{t,y} = \frac{\bar{m}_{C7} - \bar{m}_{OLC}}{\|\bar{m}_{C7} - \bar{m}_{OLC}\|} \quad (27)$$

$$\bar{e}_{t,x} = \frac{\bar{m}_{HUM} - \bar{m}_{OLC}}{\|\bar{m}_{HUM} - \bar{m}_{OLC}\|} \times \bar{e}_{t,y} \quad (28)$$

The elbow joint center \bar{e}_c was thus defined as

$$\bar{e}_c = \bar{m}_{OLC} + (e_{offset})\bar{e}_{t,x}, \quad (29)$$

using the olecranon marker and the distance of the elbow offset in the x direction of the temporary axis.

Wrist Joint:

The wrist joint center was located halfway between the ulnar and radial styloid processes as follows:

$$\bar{w}_c = \frac{1}{2}(\bar{m}_{ULN} + \bar{m}_{RAD}) \quad (30)$$

where \bar{w}_c is the wrist joint center and $\bar{m}_{subscript}$ refers to the markers.

3.2.1.2 Segment Coordinate Systems

Segment coordinate systems were determined for each of the model's eleven segments. Please refer to Appendix 4 for each corresponding figure. The joint angles were determined by the relative motion between the segment coordinate systems of two adjacent segments, distal relative to proximal. The segment coordinate systems follow the right-hand rule with the X-axis pointed anteriorly (abduction/adduction axis), the Y-axis pointed superiorly (internal/external rotation axis) and the Z-axis pointed laterally to the right (flexion/extension axis). Anatomical position was considered the neutral position. ISB recommendations were followed during segment coordinate system development [47].

Thorax Coordinate System:

A temporary origin was located at the xiphoid process marker

$$\bar{t}_{t,y} = \frac{\bar{m}_{SPC7} - \bar{m}_{STRN}}{\|\bar{m}_{SPC7} - \bar{m}_{STRN}\|} \quad (31)$$

$$\bar{t}_{t,x} = \frac{\bar{m}_{IJ} - \bar{m}_{STRN}}{\|\bar{m}_{IJ} - \bar{m}_{STRN}\|} \times \bar{t}_{t,y} \quad (32)$$

$$\bar{t}_{t,z} = \bar{t}_{t,x} \times \bar{t}_{t,y} \quad (33)$$

$$\text{Temporary thorax point, } \bar{p}_t = \bar{t}_c + 10(\bar{t}_{t,z}) \quad (34)$$

The temporary thorax point was then used to calculate the actual thorax coordinate system:

The origin was located at the thorax joint center, \bar{t}_c , as determined earlier

$$\bar{t}_x = \frac{\bar{m}_{IJ} - \bar{m}_{SPC7}}{\|\bar{m}_{IJ} - \bar{m}_{SPC7}\|} \quad (35)$$

$$\bar{t}_y = \frac{\bar{p}_t - \bar{t}_c}{\|\bar{p}_t - \bar{t}_c\|} \times \bar{t}_{t,x} \quad (36)$$

$$\bar{t}_z = \bar{t}_{t,x} \times \bar{t}_{t,y} \quad (37)$$

Clavicle Coordinate System:

The origin was located at the IJ marker, \bar{m}_{IJ} .

$$\bar{c}_z = \frac{\bar{m}_{AC} - \bar{m}_{IJ}}{\|\bar{m}_{AC} - \bar{m}_{IJ}\|} \quad (38)$$

$$\bar{c}_x = \bar{t}_y \times \bar{c}_z \quad (39)$$

$$\bar{c}_y = \bar{c}_z \times \bar{c}_x \quad (40)$$

Scapula Coordinate System:

The origin was located at the AA marker, \bar{m}_{AA} .

$$\bar{s}_z = \frac{\bar{m}_{AA} - \bar{m}_{TS}}{\|\bar{m}_{AA} - \bar{m}_{TS}\|} \quad (41)$$

$$\bar{s}_x = \frac{\bar{m}_{AA} - \bar{m}_{AI}}{\|\bar{m}_{AA} - \bar{m}_{AI}\|} \times \bar{s}_z \quad (42)$$

$$\bar{s}_y = \bar{s}_z \times \bar{s}_x \quad (43)$$

Upper Arm Coordinate System:

The origin was located at the glenohumeral joint center, \overline{GH}_C .

$$\overline{ua}_y = \frac{\overline{GH}_C - \bar{e}_c}{\|\overline{GH}_C - \bar{e}_c\|} \quad (44)$$

$$\overline{ua}_z = \frac{\bar{m}_{ULN} - \bar{e}_c}{\|\bar{m}_{ULN} - \bar{e}_c\|} \times \overline{ua}_y \quad (45)$$

$$\overline{ua}_x = \overline{ua}_y \times \overline{ua}_z \quad (46)$$

Forearm Coordinate System:

The origin was located at the ulnar styloid marker, \bar{m}_{ULN} .

$$\bar{f}_y = \frac{\bar{e}_c - \bar{m}_{ULN}}{\|\bar{e}_c - \bar{m}_{ULN}\|} \quad (47)$$

$$\bar{f}_x = \frac{\bar{m}_{ULN} - \bar{m}_{RAD}}{\|\bar{m}_{ULN} - \bar{m}_{RAD}\|} \times \bar{f}_y \quad (48)$$

$$\bar{f}_z = \bar{f}_x \times \bar{f}_y \quad (49)$$

Hand Coordinate System:

A temporary axis was set up to determine the location of the third metacarpal joint center.

The origin for the temporary axis was located at the ulnar styloid marker.

$$\overline{hand}_{t,y} = \frac{\overline{m}_{ULN} - \overline{m}_{M5}}{\|\overline{m}_{ULN} - \overline{m}_{M5}\|} \quad (50)$$

$$\overline{h}_{t,x} = \frac{\overline{m}_{ULN} - \overline{m}_{RAD}}{\|\overline{m}_{ULN} - \overline{m}_{RAD}\|} \times \overline{h}_{t,y} \quad (51)$$

$$\overline{h}_{t,z} = \overline{h}_{t,x} \times \overline{h}_{t,y} \quad (52)$$

$$\text{Third metacarpal joint center, } \overline{m}_{3c} = \overline{m}_{M5} + 0.5(t + d)(\overline{h}_{t,x}) \quad (53)$$

The hand coordinate system was defined using the third metacarpal joint center as follows:

$$\overline{h}_y = \frac{\overline{w}_c - \overline{m}_{3c}}{\|\overline{w}_c - \overline{m}_{3c}\|} \quad (54)$$

$$\overline{h}_x = \frac{\overline{m}_{ULN} - \overline{m}_{RAD}}{\|\overline{m}_{ULN} - \overline{m}_{RAD}\|} \times \overline{h}_y \quad (55)$$

$$\overline{h}_z = \overline{h}_x \times \overline{h}_y \quad (56)$$

3.2.1.3 Euler Angle Sequence

It was determined that the order of the Euler angle sequence should be ZXY, placing the most importance and accuracy on the Z axis rotations, or those in the sagittal plane, followed by the rotations about the x-axis, or coronal plane, and lastly the y-axis rotations, those occurring in the transverse plane. This sequence follows ISB recommendations [47]. The rotation matrix used is as follows:

$$[R_Z(\alpha)] = \begin{bmatrix} \cos \alpha & -\sin \alpha & 0 \\ \sin \alpha & \cos \alpha & 0 \\ 0 & 0 & 1 \end{bmatrix} \quad (57)$$

$$[R_X(\beta)] = \begin{bmatrix} 1 & 0 & 0 \\ 0 & \cos \beta & -\sin \beta \\ 0 & \sin \beta & \cos \beta \end{bmatrix} \quad (58)$$

$$[R_Y(\gamma)] = \begin{bmatrix} \cos \gamma & 0 & \sin \gamma \\ 0 & 1 & 0 \\ -\sin \gamma & 0 & \cos \gamma \end{bmatrix} \quad (59)$$

Since the proximal axes are considered to be fixed in space as the distal axes are rotated about them, the individual rotations are post multiplied, ie the Z rotation matrix, multiplied by the X rotation matrix and finally multiplied by the Y rotation matrix. This creates the overall rotation matrix as seen below, as used when determining the Euler angles between body segments.

$$[R] = [R_Y(\gamma)][R_X(\beta)][R_Z(\alpha)] \quad (60)$$

$$[R] = \begin{bmatrix} \cos \alpha \cos \gamma - \sin \alpha \sin \beta \sin \gamma & -\sin \alpha \cos \beta & \cos \alpha \sin \gamma + \sin \alpha \sin \beta \cos \gamma \\ \sin \alpha \cos \gamma + \cos \alpha \sin \beta \sin \gamma & \cos \alpha \cos \beta & \sin \alpha \sin \gamma - \cos \alpha \sin \beta \cos \gamma \\ -\cos \beta \sin \gamma & \sin \beta & \cos \beta \cos \gamma \end{bmatrix} \quad (61)$$

3.2.2 Kinetics

The kinetic portion of the dynamic upper extremity model followed the kinematic portion of the model. The kinetic model was developed to determine the upper extremity forces and moments using the Newton-Euler inverse dynamics method. The reactionary forces and moments at the hand – handrim interface (provided by the SmartWheel, see section 2.2.2.1) were used in conjunction with subject specific body segment parameters and the kinematics to determine the three-dimensional forces and moments at the wrist, elbow and glenohumeral joints. These joint forces and moments were expressed in the local coordinate systems.

3.2.2.1 Instrumentation

In order to obtain the required reactionary forces and moments a transducer was required to determine these values as the upper extremities propel the wheelchair. Three Rivers Holdings developed the SmartWheel for just that purpose. Raw voltages obtained by six strain gauges on spokes of the SmartWheel were converted to meaningful forces and moments. The SmartWheel coordinate system, in which the resulting forces and moments were defined, was similar to the global coordinate system of the lab. When the SmartWheel was located on the right side of the wheelchair, only the moment in the Z-axis needed to be flipped in order to align with global.

A SmartWheel, manufactured and acquired from Three Rivers Holdings LLC (Mesa, AZ), was used to capture kinetic data simultaneously with the motion data collection, see Appendix 5. The SmartWheel replaced the standard wheel on a wheelchair, either right or left side (or both). A “dummy” wheel was provided to replace the other wheel to ensure symmetry. The SmartWheel enabled the collection of 6-axis data (three forces and three moments) as applied to the handrim during wheelchair movement. The calibration constants converted the raw voltages provided by six strain gauges to forces (in Newtons) and moments (in Newton Meters) [60]. Using Newton-Euler inverse dynamics, this data allowed for the custom model to determine the forces and moments occurring at each UE joint of interest.

3.2.2.2 Kinetic Model Inputs

The Newton-Euler equations of motion used in the inverse dynamics method for joint force and moment calculations required many inputs. In addition to the reactionary forces and moments, body segment parameters and joint kinematics had to be known.

Subject specific body segment parameters required include each segment's: mass, inertia matrix and center of mass location. Segment mass proportion was determined through the use of polynomial regression equations developed by Jensen et al. [100]. These equations used age as the independent variable and were developed to more accurately estimate segment mass proportions throughout pediatric development to adulthood. Jensen et al. also developed polynomial regression equations based on age for the calculation of center of mass location. Lastly, to determine each subject's segment inertias, equations developed by Yeadon and Morlock et al. [96] were utilized. These equations, seen in Appendix 1, required multiple subject specific measurements.

The joint angles determined by the kinematic model were used to calculate the joint angular velocities and accelerations. Angular velocities and accelerations were calculated as described by Winter [90].

$$\omega_{JT\ i} = \frac{\theta_{JT\ i+1} - \theta_{JT\ i-1}}{2/SR} \quad (62)$$

Where $\omega_{JT\ i}$ is the joint angular velocity at the i^{th} point in time, $\theta_{JT\ i+1}$ is the joint angle at the next time point, $\theta_{JT\ i-1}$ is the joint angle at the previous time point and SR is the data sampling rate in Hz. Thus the derivative was being calculated over two time intervals.

Angular acceleration was similarly calculated:

$$\alpha_{JT\ i} = \frac{\omega_{JT\ i+1} - 2*\omega_{JT\ i} + \omega_{JT\ i-1}}{(1/SR)^2} \quad (63)$$

Where $\alpha_{JT\ i}$ is the joint angular acceleration at the i^{th} point in time, $\omega_{JT\ i+1}$ is the joint angular velocity at the next time point, $\omega_{JT\ i}$ is the angular velocity at the current, i^{th} time point and $\omega_{JT\ i-1}$ is the joint angular velocity at the previous time point. This derivative was also being calculated over two time intervals [90].

Similar equations were used to calculate the velocity and acceleration of the center of mass of each segment.

3.2.2.3 Inverse Dynamics

Then the segment mass, segment center of mass acceleration and the distal joint forces and moments were used in Newton-Euler inverse dynamics equations to determine the forces and moments occurring at the more proximal joint. This was first applied at the hand-wheelchair handrim interface and continued up the kinematic chain for evaluation at each sequential joint of interest.

The Newton-Euler equations of motion are as follows from Zatsiorsky [109]:

$$F_i - F_{i+1} + m_i g - m_i a_i = 0 \quad (64)$$

$$\dot{H} = [I_i] \ddot{\theta}_i + \dot{\theta}_i \times ([I_i] \dot{\theta}_i) = \bar{M}_R \quad (65)$$

$$T_i - T_{i+1} + r_i \times F_i - r_{i+1} \times F_{i+1} - [I_i] \ddot{\theta}_i - \dot{\theta}_i \times ([I_i] \dot{\theta}_i) = 0 \quad (66)$$

Where F_i and F_{i+1} are the forces acting on the link (or in our case segment) i at joint i and $i + 1$ respectively; m_i is the mass of segment i ; a_i is the acceleration of the center of mass of segment i and g is the acceleration due to gravity. In the second equation, T_i and T_{i+1} are the torques acting on segment i at joint i and $i + 1$ respectively; r_i and r_{i+1} are

the moment arms which are the distance from the center of mass of segment i to the joint centers i and $i + 1$ respectively; $[I_i]$ is the inertia matrix and $\dot{\theta}_i$ and $\ddot{\theta}_i$ are the angular velocity and angular acceleration of segment i respectively.

3.2.2.4 Kinetic Model Equations

SmartWheel: Subject Hand – Handrim Interface

The forces at the subject hand – handrim interface \bar{F}_{SW} were directly determined by the SmartWheel transducer and were aligned with the laboratory's global reference system: X-axis pointing anteriorly, Y-axis pointing superiorly and Z-axis pointing laterally to the right. The moments occurring at the hand – handrim interface \bar{M}_{SW} were also directly determined by the SmartWheel transducer and were primarily aligned with the global coordinate system. When the SmartWheel was placed on the right side of the wheelchair, adduction and internal rotations about the X- and Y-axes respectively were positive and the moment value about the Z-axis needed to be negated for coordinate system agreement: flexion rotation was positive. When the SmartWheel was placed on the left side of the wheelchair there was an additional discrepancy between the transducer coordinate system and the global reference system: the moment about the X-axis also needed to be negated to follow convention. See images below from the SmartWheel User's Guide 2010 [60], to confirm.

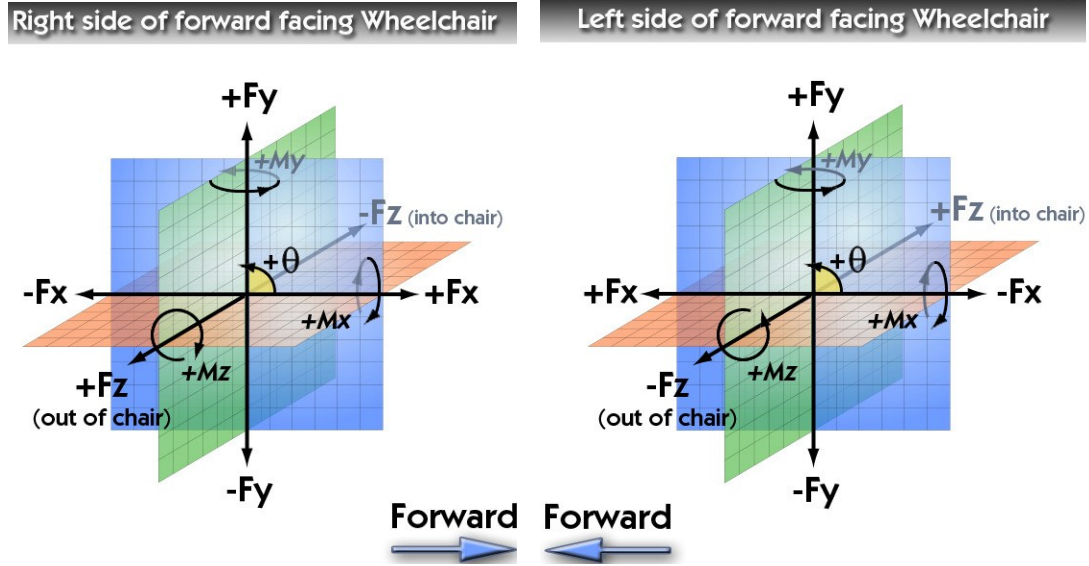


Figure 7: From SmartWheel User's Guide 2010 – Three Rivers [60].

The dynamic equations were formed via Zatsiorsky's equations [109] and solved with the inverse dynamics approach, as described above. The SmartWheel provided the crucial force and moment values occurring at the hand-handrim interface, reducing the amount of unknown forces and moments acting on the hand segment to only one, those occurring at the wrist joint. Thus the unknown wrist force and moment, acting at the proximal end of hand segment could be calculated by Zatsiorsky's force balance equation (64). The positive and negative signs of the wrist force and moment were then negated and the values used as inputs at the distal end of the next segment in order to determine the joint force and moment at the proximal end of that next segment. This was continued until joint dynamics were calculated for the wrist, elbow and glenohumeral joints.

Wrist Joint

By rearranging equation (64), the wrist force, \bar{F}_W , was computed by summing the force due to the linear acceleration of the hand center of mass, the force of the hand due to gravity and the force applied by the hand.

$$\bar{F}_W = -mass_H(\bar{a}_H - \bar{g}) - \bar{F}_{SW} \quad (67)$$

Where $mass_H$ is the subject specific mass of the hand, \bar{a}_H is the linear acceleration of hand center of mass and \bar{g} is the acceleration due to gravity (9.81m/s^2). \bar{F}_{SW} is the known reactionary hand force as provided by the SmartWheel transducer and \bar{F}_W is the unknown force being applied at the wrist joint.

By rearranging equation (66), the wrist moment, \bar{M}_W , was computed by subtracting the moment occurring about the hand center of mass of due to the force acting on the distal portion of the hand, \bar{M}_{DisH} , the moment occurring about the hand center of mass due to the force acting on the proximal end of the hand, \bar{M}_{ProxH} , and the known reactionary Smartwheel moment, \bar{M}_{SW} , from the rate of change of angular momentum for the hand, \dot{H}_H .

$$\bar{M}_W = \dot{H}_H + (-\bar{M}_{SW} - \bar{M}_{DisH} - \bar{M}_{ProxH}) \quad (68)$$

$$\bar{M}_{ProxH} = \bar{r}_{ProxH} \times \bar{F}_W \quad (69)$$

$$\bar{M}_{DisH} = \bar{r}_{DisH} \times \bar{F}_{SW} \quad (70)$$

Where \bar{r}_{ProxH} and \bar{r}_{DisH} are the moment arms from the center of mass of the hand to the wrist joint center and the third metacarpal joint, respectively.

Elbow Joint

The elbow joint force, \bar{F}_E , was computed by summing the force due to the linear acceleration of the forearm center of mass, the forearm force due to gravity and the force applied to the wrist by the hand.

$$\bar{F}_E = -mass_{FA}(\bar{a}_{FA} - \bar{g}) - (-\bar{F}_W) \quad (71)$$

Where $mass_{FA}$ is the subject specific mass of the forearm, \bar{a}_{FA} is the linear acceleration of forearm center of mass and \bar{g} is the acceleration due to gravity (9.81 m/s^2). $(-\bar{F}_W)$ is

the known reactionary wrist force and \bar{F}_E is the unknown force being applied at the elbow joint.

By rearranging equation (66), the elbow moment, \bar{M}_E , was computed by subtracting the moment occurring about the forearm center of mass of due to the force acting on the distal portion of the forearm, \bar{M}_{DisFA} , the moment occurring about the forearm center of mass due to the force acting on the proximal end of the forearm, \bar{M}_{ProxFA} , and the known reactionary wrist moment, $(-\bar{M}_W)$, from the rate of change of angular momentum for the forearm, \dot{H}_{FA} .

$$\bar{M}_E = \dot{H}_{FA} + (-(-\bar{M}_W) - \bar{M}_{DisFA} - \bar{M}_{ProxFA}) \quad (72)$$

$$\bar{M}_{ProxFA} = \bar{r}_{ProxFA} \times \bar{F}_E \quad (73)$$

$$\bar{M}_{DisFA} = \bar{r}_{DisFA} \times (-\bar{F}_W) \quad (74)$$

Where \bar{r}_{ProxFA} and \bar{r}_{DisFA} are the moment arms from the center of mass of the forearm to the elbow joint center and the wrist joint center, respectively.

Glenohumeral Joint

The glenohumeral joint force, \bar{F}_{GH} , was computed by summing the force due to the linear acceleration of the upperarm center of mass, the upperarm force due to gravity and the force applied to the elbow by the forearm.

$$\bar{F}_{GH} = -mass_{UA}(\bar{a}_{UA} - \bar{g}) - \bar{F}_E \quad (75)$$

Where $mass_{UA}$ is the subject specific mass of the upperarm, \bar{a}_{UA} is the linear acceleration of upperarm center of mass and \bar{g} is the acceleration due to gravity (9.81 m/s²). $(-\bar{F}_E)$ is the known reactionary elbow force as provided by and \bar{F}_{GH} is the unknown force being applied at the glenohumeral joint.

By rearranging equation (66), the glenohumeral moment, \bar{M}_{GH} , was computed by subtracting the moment occurring about the upper arm center of mass of due to the force acting on distal portion of the upperarm, \bar{M}_{DisUA} , the moment occurring about the upper arm center of mass due to the force acting on the proximal end of the upperarm, \bar{M}_{ProxUA} , and the known reactionary elbow moment, $(-\bar{M}_E)$, from the rate of change of angular momentum for the upperarm, \dot{H}_{UA} .

$$\bar{M}_{GH} = \dot{H}_{UA} + (-(-\bar{M}_E) - \bar{M}_{DisUA} - \bar{M}_{ProxUA}) \quad (76)$$

$$\bar{M}_{ProxUA} = \bar{r}_{ProxUA} \times \bar{F}_{GH} \quad (77)$$

$$\bar{M}_{DisUA} = \bar{r}_{DisUA} \times (-\bar{F}_E) \quad (78)$$

Where \bar{r}_{ProxUA} and \bar{r}_{DisUA} are the moment arms from the center of mass of the upperarm to the glenohumeral joint center and the elbow joint center, respectively.

3.2.3 Application to Patient Population

The biomechanical model was implemented at Shriners Hospital for Children – Chicago for preliminary analysis of pediatric mobility in manual wheelchairs. A young adolescent male, 17 years of age, with SCI was evaluated. The motions of the wrist, elbow, shoulder, scapula, clavicle and thorax as well as the forces and moments at the wrist, elbow and shoulder were determined in all three planes of motion: sagittal, coronal and transverse. Preliminary results are presented.



Figure 8: Test subject propelling through lab.

3.2.3.1 Test Protocol

All subject specific measurements and marker placement were completed by a licensed physical therapist. A static calibration test was performed in order to capture the locations of the all the scapular markers with respect to one another, for implementation of Senk et al.'s method as previously discussed. The AI and TS markers were then removed from the test subject and the dynamic testing conducted. The subject propelled his wheelchair along a 15m pathway in the laboratory at comfortable, self-selected speed, which averaged 1.0m/s, Figure 8. The SmartWheel system collected the subject's right-hand side (dominant) 3D forces and moments occurring at the handrim interface at a sampling rate of 240 Hz during propulsion. The SmartWheel system triggered a Vicon MX motion capture system (Vicon Motion Systems, Ltd., Oxford, England), with 14 infrared cameras, to simultaneously collect synchronized 3D motion of reflective markers

placed on the subject and the wheelchair at a sampling rate of 120 Hz. The subject performed five trials and was allowed adequate rest between trials.

Vicon motion analysis software (Nexus) was used to process the 3D motion data of each reflective marker throughout the trial. This data was filtered using a Woltring Filter. The custom UE biomechanical model, as developed in Matlab, was applied to the motion and SmartWheel data to determine the joint motions (position, velocity, and acceleration), forces and moments. Matlab and Excel were used for further data processing and reporting.

3.3 Results

3.3.1 Upper Extremity Kinematics

For the five trials conducted, a total of 10 stroke cycles were obtained for analysis. The mean joint angles of the sternoclavicular, acromioclavicular, glenohumeral, elbow and wrist joints and thorax were characterized over the entire wheelchair stroke cycle. One hundred percent stroke cycle is defined by both the push and recovery phases, with 0% stroke cycle representing the initial contact at the beginning of the push phase. The transition point for each stroke cycle was determined as data is displayed in Table 2, along with the average transition point in terms of percent stroke cycle. The mean joint angles and +/- one standard deviation (STDEV) over the entire stroke cycle for each joint in all three planes of motion are depicted in the figures that follow, the subject's left side is in red and right side is in blue. Also, the average peak and minimum joint angles, as well as joint range of motion were calculated and are displayed in the tables below with their respective joint. Additionally, a paired T-Test was used to determine asymmetry between the left and right side kinematics and the results are also noted in the tables

below. Note that for the glenohumeral and acromioclavicular joints results are displayed for data derived both with respect to the proximal joint and to the thorax for each joint.

For further clarification see Appendix 2 for sign convention descriptions.

Table 2: The transition points from push phase to recovery phase in terms of percent stroke cycle for each stroke, as well as maximum, minimum, average and standard deviation (STDEV) statistics.

Stroke Number	Push to Recovery (% Cycle)
1	51.76
2	55.48
3	63.95
4	54.67
5	48.15
6	57.76
7	50.86
8	48.08
9	48.70
10	47.13
Maximum	63.95
Minimum	47.13
Average	52.65
STDEV	5.34

Wrist Joint Angle
Left (red) and Right (blue) Sides

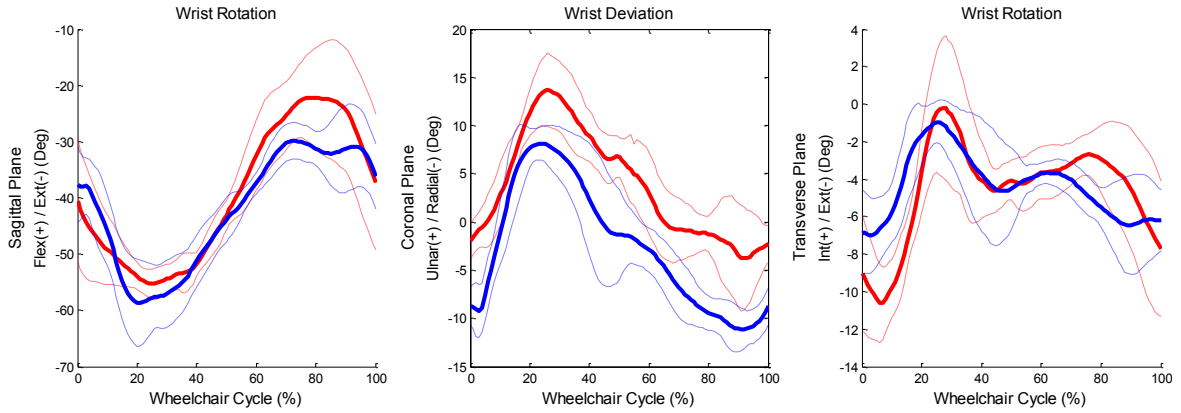


Figure 9: Mean (**bold**) and ± 1 STDEV (dashed) of bilateral wrist joint kinematics during the stroke cycle for 10 stroke cycles. *Left: red; Right: blue.

Table 3: Mean (STDEV) maximum and minimum angles and ROM for the wrists, in all planes of motion. (* and ** indicate statistically significant difference, with $p < 0.01$ and $p < 0.05$, respectively)

Sagittal Plane - Flexion (+), Extension (-)					
Joint	Max Angle (SD) (deg)	Location (SD) (%)	Min Angle (SD) (deg)	Location (SD) (%)	ROM (SD) (deg)
Right Wrist	-27.41 (4.15) **	86.7% (9.73)	-60.21 (6.76)	23.7% (6.29)	32.80 (6.18)
Left Wrist	-20.21 (8.92) **	82.2% (7.45)	-56.26 (2.82)	26.3% (7.01)	36.05 (9.19)
Coronal Plane - Ulnar Deviation (+), Radial Deviation (-)					
Joint	Max Angle (SD) (deg)	Location (SD) (%)	Min Angle (SD) (deg)	Location (SD) (%)	ROM (SD) (deg)
Right Wrist	8.89 (1.55) *	25.2% (6.55)	-12.47 (1.28) *	93.9% (7.31)	21.36 (2.18)
Left Wrist	14.42 (3.40) *	28% (3.68)	-6.18 (4.01) *	94.4% (10.36)	20.61 (3.83)
Transverse Plane - Internal Rotation (+), External Rotation (-)					
Joint	Max Angle (SD) (deg)	Location (SD) (%)	Min Angle (SD) (deg)	Location (SD) (%)	ROM (SD) (deg)
Right Wrist	-0.44 (1.16)	25.3% (6.68) **	-8.48 (2.28) *	41.4% (32.24) **	8.03 (2.32) *
Left Wrist	1.39 (2.66)	40% (24.26) **	-11.31 (1.61) *	10.8% (10.41) **	12.70 (3.04) *

Elbow Joint Angle
Left (red) and Right (blue) Sides

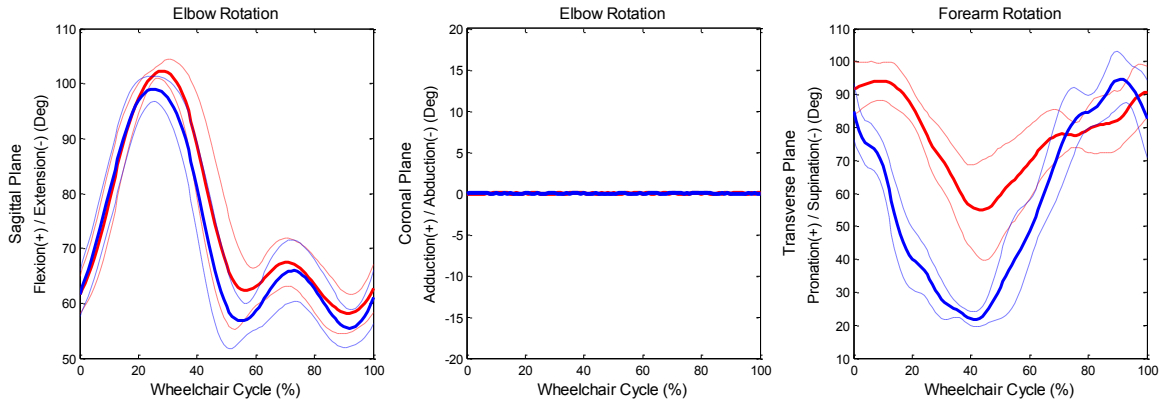


Figure 10: Mean (**bold**) and +/- 1 STDEV (dashed) of bilateral elbow joint kinematics during the stroke cycle for 10 stroke cycles. *Left: red; Right: blue.

Table 4: Mean (STDEV) maximum and minimum angles and ROM for the elbows, in all planes of motion. (* and ** indicate statistically significant difference, with $p < 0.01$ and $p < 0.05$, respectively)

Sagittal Plane - Flexion (+), Extension (-)					
Joint	Max Angle (SD) (deg)	Location (SD) (%)	Min Angle (SD) (deg)	Location (SD) (%)	ROM (SD) (deg)
Right Elbow	99.62 (2.32) *	26% (3.30) **	53.61 (1.92) **	69.9% (20.05)	46.01 (2.13)
Left Elbow	103.07 (1.51) *	28.9% (3.73) **	55.69 (2.28) **	81.1% (16.58)	47.38 (2.07)
Coronal Plane - Restrained					
Joint	Max Angle (SD) (deg)	Location (SD) (%)	Min Angle (SD) (deg)	Location (SD) (%)	ROM (SD) (deg)
Right Elbow	0.00 (0.00)	0.00 (0.00)	0.00 (0.00)	0.00 (0.00)	0.00 (0.00)
Left Elbow	0.00 (0.00)	0.00 (0.00)	0.00 (0.00)	0.00 (0.00)	0.00 (0.00)
Transverse Plane - Pronation (+), Supination (-)					
Joint	Max Angle (SD) (deg)	Location (SD) (%)	Min Angle (SD) (deg)	Location (SD) (%)	ROM (SD) (deg)
Right Elbow	97.57 (6.56)	92% (5.81) *	20.54 (2.75) *	41.2% (5.05) **	77.03 (8.02) *
Left Elbow	97.34 (7.18)	5.3% (9.82) *	49.68 (12.42) *	46.3% (6.18) **	47.66 (10.16) *

Glenohumeral Joint Angle – With Respect to the Scapula
Left (red) and Right (blue) Sides

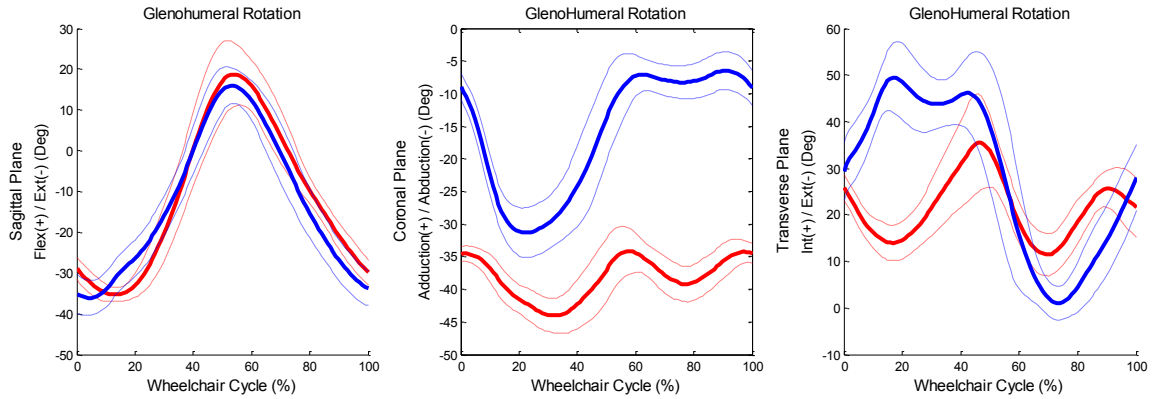


Figure 11: Mean (**bold**) and +/- 1 STDEV (dashed) of bilateral glenohumeral joint kinematics during the stroke cycle for 10 stroke cycles. *Left: red; Right: blue.

Table 5: Mean (STDEV) maximum and minimum angles and ROM for the glenohumeral joints, in all planes of motion. (* and ** indicate statistically significant difference, with $p < 0.01$ and $p < 0.05$, respectively)

Sagittal Plane - Flexion (+), Extension (-)					
Joint	Max Angle (SD) (deg)	Location (SD) (%)	Min Angle (SD) (deg)	Location (SD) (%)	ROM (SD) (deg)
Right Glenohumeral	17.72 (3.99)	54.2% (4.47)	-36.67 (3.95)	4.3% (3.13) *	54.39 (4.46)
Left Glenohumeral	20.93 (5.65)	55.1% (4.53)	-36.16 (1.41)	13.3% (5.50) *	57.09 (5.37)
Coronal Plane - Adduction (+), Abduction (-)					
Joint	Max Angle (SD) (deg)	Location (SD) (%)	Min Angle (SD) (deg)	Location (SD) (%)	ROM (SD) (deg)
Right Glenohumeral	-4.88 (2.28) *	73.9% (18.73)	-31.68 (3.80) *	23.6% (3.50) *	26.79 (2.94) *
Left Glenohumeral	-31.90 (2.75) *	83.3% (22.31)	-44.74 (3.17) *	33.3% (4.45) *	12.84 (4.42) *
Transverse Plane - Internal Rotation (+), External Rotation (-)					
Joint	Max Angle (SD) (deg)	Location (SD) (%)	Min Angle (SD) (deg)	Location (SD) (%)	ROM (SD) (deg)
Right Glenohumeral	52.30 (7.74) *	29.6% (14.62) **	-0.15 (4.06) *	75% (4.08) **	52.45 (10.00) *
Left Glenohumeral	37.97 (7.71) *	43.9% (15.48) **	9.76 (2.70) *	60.1% (23.63) **	28.21 (9.69) *

*Glenohumeral Joint Angle – With Respect to the Thorax
Left (red) and Right (blue) Sides*

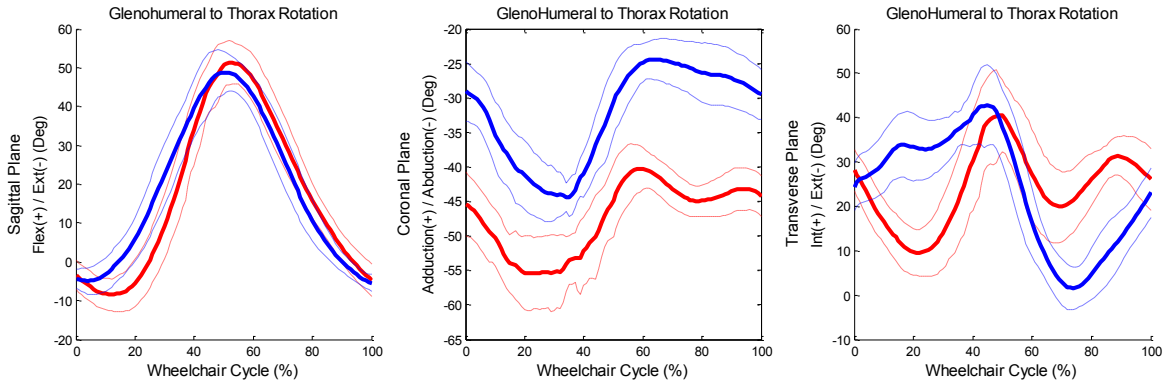


Figure 12: Mean (**bold**) and +/- 1 STDEV (dashed) of bilateral glenohumeral joint kinematics during the stroke cycle for 10 stroke cycles. *Left: red; Right: blue.

Table 6: Mean (STDEV) maximum and minimum angles and ROM for the glenohumeral joints, in all planes of motion. (* and ** indicate statistically significant difference, with $p < 0.01$ and $p < 0.05$, respectively)

Sagittal Plane - Flexion (+), Extension (-)					
Joint	Max Angle (SD) (deg)	Location (SD) (%)	Min Angle (SD) (deg)	Location (SD) (%)	ROM (SD) (deg)
Right GH to Thorax	50.22 (5.40)	52.3% (4.50)	-6.68 (2.82) **	1.5% (2.59) *	56.90 (4.11) *
Left GH to Thorax	52.82 (4.74)	52.9% (4.18)	-10.49 (3.52) **	10.9% (6.61) *	63.31 (4.55) *
Coronal Plane - Adduction (+), Abduction (-)					
Joint	Max Angle (SD) (deg)	Location (SD) (%)	Min Angle (SD) (deg)	Location (SD) (%)	ROM (SD) (deg)
Right GH to Thorax	-22.60 (1.85) *	69.6% (14.79)	-46.01 (2.50) *	31.7% (3.71) **	23.41 (1.76) *
Left GH to Thorax	-38.47 (2.08) *	68.1% (15.82)	-56.65 (5.59) *	24.8% (10.61) **	18.17 (5.41) *
Transverse Plane - Internal Rotation (+), External Rotation (-)					
Joint	Max Angle (SD) (deg)	Location (SD) (%)	Min Angle (SD) (deg)	Location (SD) (%)	ROM (SD) (deg)
Right GH to Thorax	44.62 (8.46)	42.6% (10.06) **	0.17 (5.28) *	75.6% (3.75) *	44.45 (10.98)
Left GH to Thorax	45.02 (6.94)	54.1% (13.82) **	7.82 (5.65) *	33.4% (20.03) *	37.20 (7.17)

Acromioclavicular Joint Angle – With Respect to the Clavicle
Left (red) and Right (blue) Sides

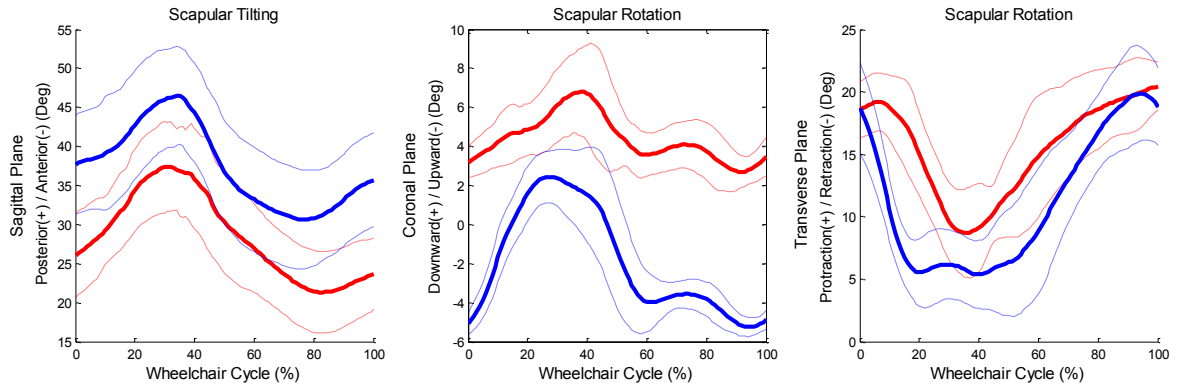


Figure 13: Mean (**bold**) and ± 1 STDEV (dashed) of bilateral acromioclavicular joint kinematics during the stroke cycle for 10 stroke cycles. *Left: red; Right: blue.

Table 7: Mean (STDEV) maximum and minimum angles and ROM for the acromioclavicular joints, in all planes of motion. (* and ** indicate statistically significant difference, with $p < 0.01$ and $p < 0.05$, respectively)

	Sagittal Plane - Flexion (+), Extension (-)				
Joint	Max Angle (SD) (deg)	Location (SD) (%)	Min Angle (SD) (deg)	Location (SD) (%)	ROM (SD) (deg)
Right Acromioclavicular	46.99 (6.19) *	33.1% (2.81)	30.26 (6.25) *	77% (6.16) *	16.73 (2.15)
Left Acromioclavicular	37.88 (6.02) *	33.9% (3.70)	21.02 (5.11) *	85% (6.86) *	16.85 (4.57)
	Coronal Plane - Adduction (+), Abduction (-)				
Joint	Max Angle (SD) (deg)	Location (SD) (%)	Min Angle (SD) (deg)	Location (SD) (%)	ROM (SD) (deg)
Right Acromioclavicular	2.76 (1.37) *	30.2% (5.33) *	-5.72 (0.51) *	83.6% (21.62)	8.49 (1.34) *
Left Acromioclavicular	7.48 (2.28) *	38.6% (6.08) *	2.05 (0.72) *	78.3% (19.70)	5.42 (2.48) *
	Transverse Plane - Internal Rotation (+), External Rotation (-)				
Joint	Max Angle (SD) (deg)	Location (SD) (%)	Min Angle (SD) (deg)	Location (SD) (%)	ROM (SD) (deg)
Right Acromioclavicular	21.54 (2.87)	95.7% (5.52)	3.31 (2.99) *	39.1% (13.80)	18.23 (2.78) *
Left Acromioclavicular	21.36 (2.28)	99.6% (9.37)	7.30 (2.60) *	42.6% (7.89)	14.06 (2.57) *

With Respect to the Thorax
Left (red) and Right (blue) Sides

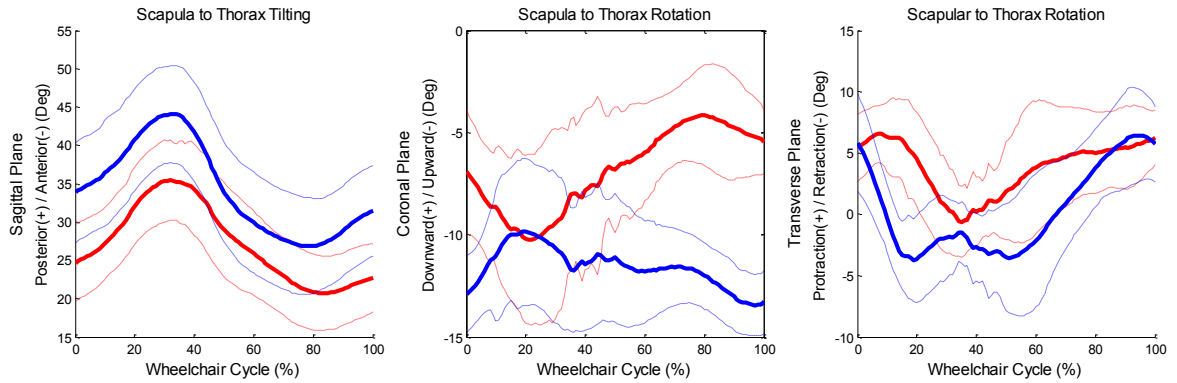


Figure 14: Mean (**bold**) and ± 1 STDEV (dashed) of bilateral acromioclavicular joint kinematics during the stroke cycle for 10 stroke cycles. *Left: red; Right: blue.

Table 8: Mean (STDEV) maximum and minimum angles and ROM for the acromioclavicular joints, in all planes of motion. (* and ** indicate statistically significant difference, with $p < 0.01$ and $p < 0.05$, respectively)

Sagittal Plane - Flexion (+), Extension (-)					
Joint	Max Angle (SD) (deg)	Location (SD) (%)	Min Angle (SD) (deg)	Location (SD) (%)	ROM (SD) (deg)
Right AC to Thorax	44.39 (6.34) *	32.7% (2.95)	26.48(6.25) **	77.6% (6.38) *	17.91 (2.38)
Left AC to Thorax	35.84 (5.49) *	34.3% (3.56)	20.43 (4.79) **	85.8 (6.53) *	15.41 (3.50)
Coronal Plane - Adduction (+), Abduction (-)					
Joint	Max Angle (SD) (deg)	Location (SD) (%)	Min Angle (SD) (deg)	Location (SD) (%)	ROM (SD) (deg)
Right AC to Thorax	-8.48 (2.84) *	40.7% (24.19) *	-14.32 (1.73)	89.2% (22.5) *	5.84 (2.43)
Left AC to Thorax	-3.19 (1.56) *	78.8% (14.92) *	-11.45 (4.59)	26% (15.60) *	8.26 (4.19)
Transverse Plane - Internal Rotation (+), External Rotation (-)					
Joint	Max Angle (SD) (deg)	Location (SD) (%)	Min Angle (SD) (deg)	Location (SD) (%)	ROM (SD) (deg)
Right AC to Thorax	8.02 (3.39)	96% (5.79)	-6.08 (3.75) **	33.7% (16.85)	14.09 (4.14) **
Left AC to Thorax	8.50 (1.95)	92% (20.41)	-2.22 (2.47) **	41.4% (8.87)	10.72 (2.32) **

Sternoclavicular Joint Angle
Left (red) and Right (blue) Sides

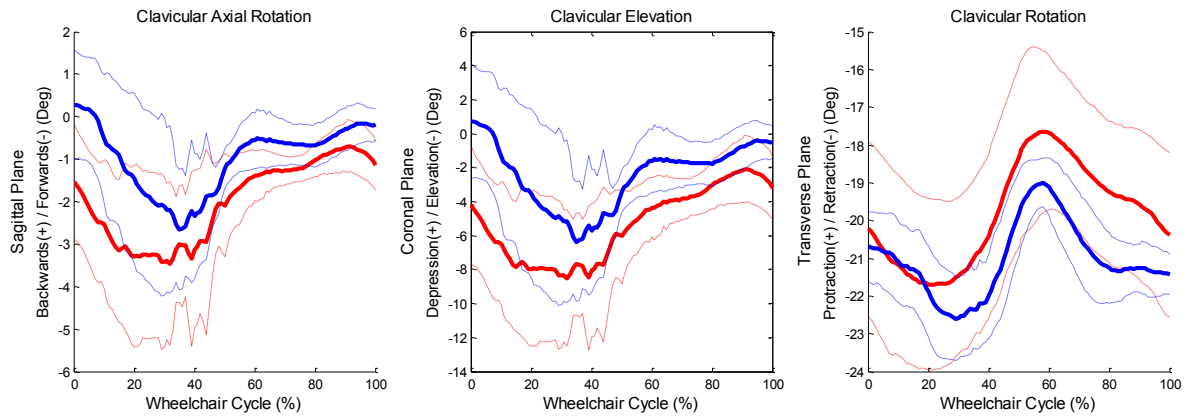


Figure 15: Mean (**bold**) and +/- 1 STDEV (dashed) of bilateral sternoclavicular joint kinematics during the stroke cycle for 10 stroke cycles. *Left: red; Right: blue.

Table 9: Mean (STDEV) maximum and minimum angles and ROM for the sternoclavicular joints, in all planes of motion. (* and ** indicate statistically significant difference, with $p < 0.01$ and $p < 0.05$, respectively)

	Coronal Plane - Adduction (+), Abduction (-)				
Joint	Max Angle (SD) (deg)	Location (SD) (%)	Min Angle (SD) (deg)	Location (SD) (%)	ROM (SD) (deg)
Right Sternoclavicular	2.14 (3.73) *	90.3% (21.42)	-7.81 (1.75)	38.6% (6.31)	9.95 (4.63)
Left Sternoclavicular	-1.66 (1.73) *	95.4% (4.84)	-10.09 (4.62)	30.9% (14.78)	8.44 (4.47)
	Transverse Plane - Internal Rotation (+), External Rotation (-)				
Joint	Max Angle (SD) (deg)	Location (SD) (%)	Min Angle (SD) (deg)	Location (SD) (%)	ROM (SD) (deg)
Right Sternoclavicular	-18.71 (0.85)	58.2% (4.32)	-22.99 (1.02)	39.2% (20.02)	4.28 (0.98)
Left Sternoclavicular	-17.31 (2.03)	58.5% (6.87)	-22.09 (2.25)	27.6% (21.69)	4.78 (1.12)

Thorax Angle

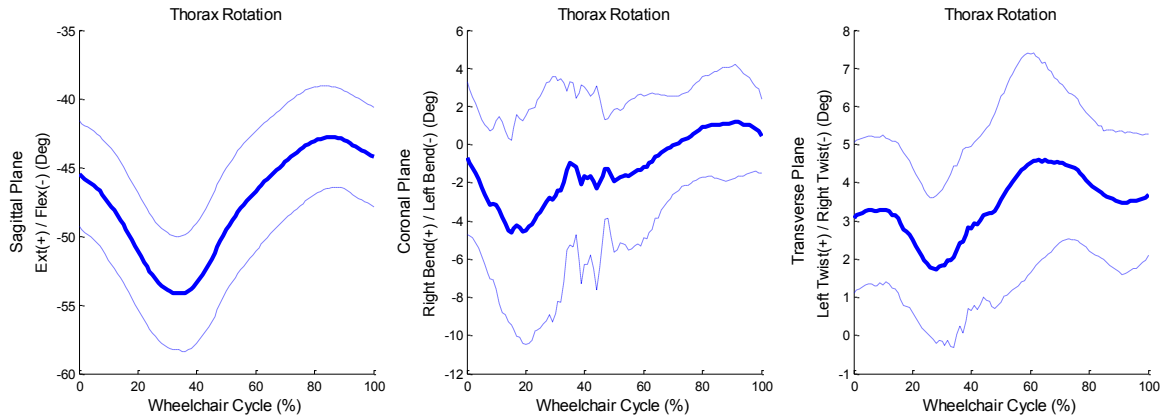


Figure 16: Mean (**bold**) and +/- 1 STDEV (dashed) of thorax kinematics during the stroke cycle for 10 stroke cycles.

Table 10: Mean (STDEV) maximum and minimum angles and ROM for the thorax, in all planes of motion.

Sagittal Plane - Flexion (+), Extension (-)					
Joint	Max Angle (SD) (deg)	Location (SD) (%)	Min Angle (SD) (deg)	Location (SD) (%)	ROM (SD) (deg)
Thorax	-42.56 (3.65)	87.5% (6.35)	-54.30 (4.15)	35.2% (2.25)	11.74 (1.70)
Coronal Plane - Right Bend (+), Left Bend (-)					
Joint	Max Angle (SD) (deg)	Location (SD) (%)	Min Angle (SD) (deg)	Location (SD) (%)	ROM (SD) (deg)
Thorax	2.57 (2.22)	75.3% (21.09)	-6.99 (5.81)	25.6% (17.15)	9.56 (5.54)
Transverse Plane - Left Twist (+), Right Twist (-)					
Joint	Max Angle (SD) (deg)	Location (SD) (%)	Min Angle (SD) (deg)	Location (SD) (%)	ROM (SD) (deg)
Thorax	5.97 (1.69)	77.4% (21.61)	0.92 (2.06)	48.4% (23.81)	5.05 (1.85)

3.3.2 Upper Extremity Kinetics

The mean joint forces and moments of the subject's right glenohumeral, elbow and wrist joints were characterized over the entire wheelchair stroke cycle. One hundred percent stroke cycle is defined by both the push and recovery phases, with 0% stroke cycle representing the initial contact at the beginning of the push phase. The mean joint forces and moments and +/- one standard deviation (STDEV) for each joint in all three planes of motion over the entire stroke cycle are depicted in the figures that follow.

Additionally, the average peak and minimum joint forces and moments, as well as joint and moment range, were calculated and are displayed in the tables below with their respective joint.

Wrist Joint Force – Right Side

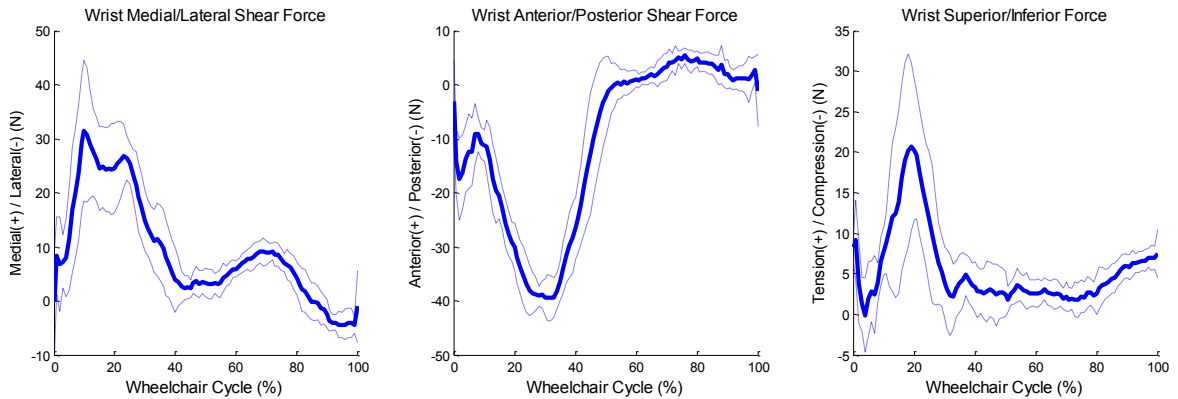


Figure 17: Mean (**bold**) and +/- 1 STDEV (dashed) right wrist joint forces during the stroke cycle for 10 stroke cycles.

Table 11: Mean (STDEV) maximum and minimum forces and force range for the right wrist, in all planes of motion.

Right Wrist Joint	Med (+) / Lat (-)	Location (SD) (%)	Ant (+) / Pos (-)	Location (SD) (%)	Sup (+) / Inf (-)	Location (SD) (%)
Max Force (SD) (N)	38.25 (6.75)	14.5% (5.42)	-43.03 (2.75)	30.5% (5.02)	24.44 (9.50)	19.9% (3.60)
Min Force (SD) (N)	-6.31 (1.81)	96.7% (3.97)	7.30 (1.62)	82.1% (8.24)	-4.49 (2.20)	20.1% (17.86)
Force Range (SD) (N)	44.57 (7.42)		50.34 (2.39)		28.93 (10.70)	

Elbow Joint Force – Right Side

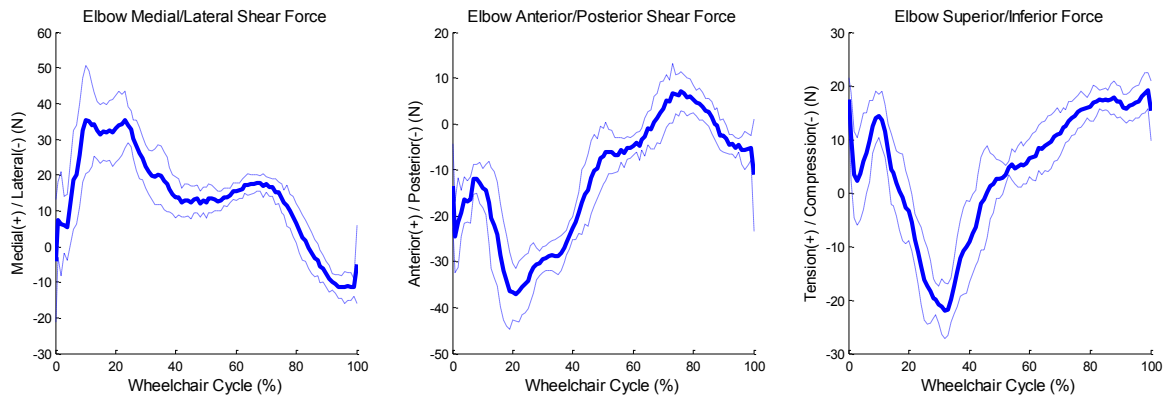


Figure 18: Mean (**bold**) and +/- 1 STDEV (dashed) right elbow joint forces during the stroke cycle for 10 stroke cycles.

Table 12: Mean (STDEV) maximum and minimum forces and force range for the right elbow, in all planes of motion.

Right Elbow Joint	Med (+) / Lat (-)	Location (SD) (%)	Ant (+) / Pos (-)	Location (SD) (%)	Sup (+) / Inf (-)	Location (SD) (%)
Max Force (SD) (N)	44.51 (6.38)	15% (4.71)	40.5 (7.29)	21..8% (8.30)	21.45 (2.76)	93.8% (11.11)
Min Force (SD) (N)	-14.23 (3.90)	97.1% (4.12)	-9.90 (3.21)	76.6% (4.27)	-24.75 (3.45)	31.5% (4.43)
Force Range (SD) (N)	50.40 (7.29)		46.20 (3.94)		58.74 (7.78)	

Glenohumeral Joint Force – Right Side

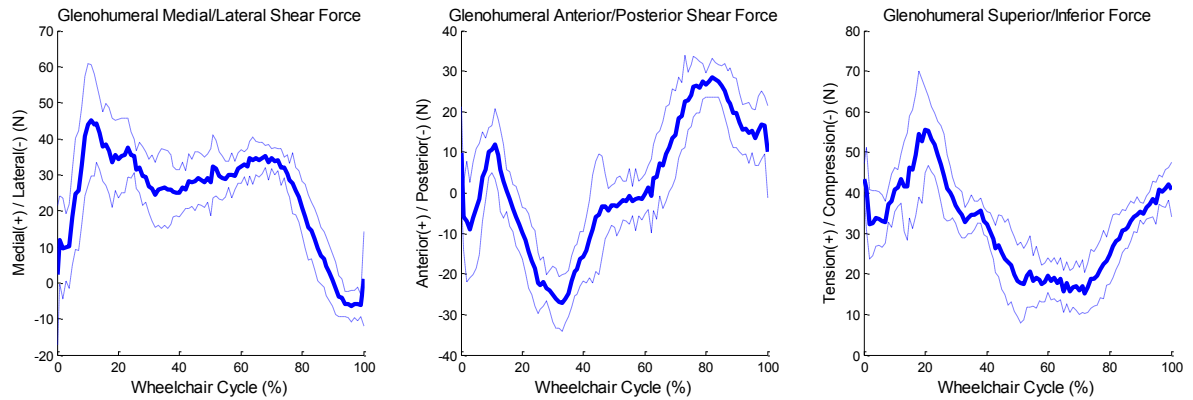


Figure 19: Mean (bold) and ± 1 STDEV (dashed) right glenohumeral joint forces during the stroke cycle for 10 stroke cycles.

Table 13: Mean (STDEV) maximum and minimum forces and force range for the right glenohumeral joint, in all planes of motion.

Right GH Joint	Med (+) / Lat (-)	Location (SD) (%)	Ant (+) / Pos (-)	Location (SD) (%)	Sup (+) / Inf (-)	Location (SD) (%)
Max Force (SD) (N)	54.24 (8.80)	23.4% (20.38)	31.20 (4.38)	27.2% (12.78)	61.86 (10.87)	20.3% (3.56)
Min Force (SD) (N)	-10.57 (3.74)	96.3% (3.65)	-33.52 (5.05)	82.1% (5.24)	8.98 (3.37)	59.8% (10.35)
Force Range (SD) (N)	64.72 (5.47)		52.88 (11.43)		64.81 (9.33)	

Wrist Joint Moment – Right Side

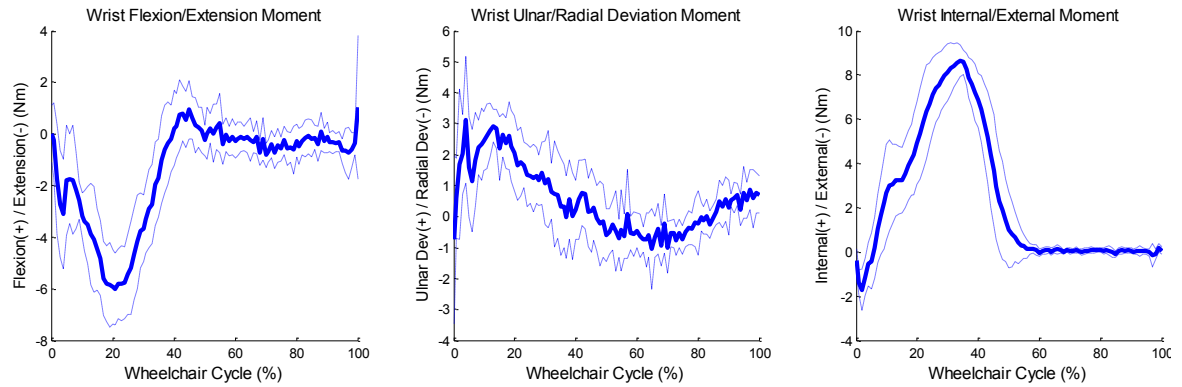


Figure 20: Mean (**bold**) and ± 1 STDEV (dashed) right wrist joint moments during the stroke cycle for 10 stroke cycles.

Table 14: Mean (STDEV) maximum and minimum moments and moment range for the right wrist, in all planes of motion.

Right Wrist Joint	Sagittal Plane	Location (SD) (%)	Coronal Plane	Location (SD) (%)	Transverse Plane	Location (SD) (%)
	Flexion (+) / Extension (-)		Ulnar Dev (+) / Radial Dev (-)		Internal (+) / External (-)	
Max Moment (SD) (Nm)	2.76 (2.03)	38.8% (21.26)	4.59 (0.96)	9.4% (7.18)	9.05 (0.72)	33.9% (4.20)
Min Moment (SD) (Nm)	-6.79 (1.46)	22.7% (3.80)	-3.09 (1.84)	45.1% (17.72)	-1.96 (0.54)	3% (1.25)
Moment Range (SD) (Nm)	9.55 (2.70)		7.68 (2.17)		11.01 (0.76)	

Elbow Joint Moment – Right Side

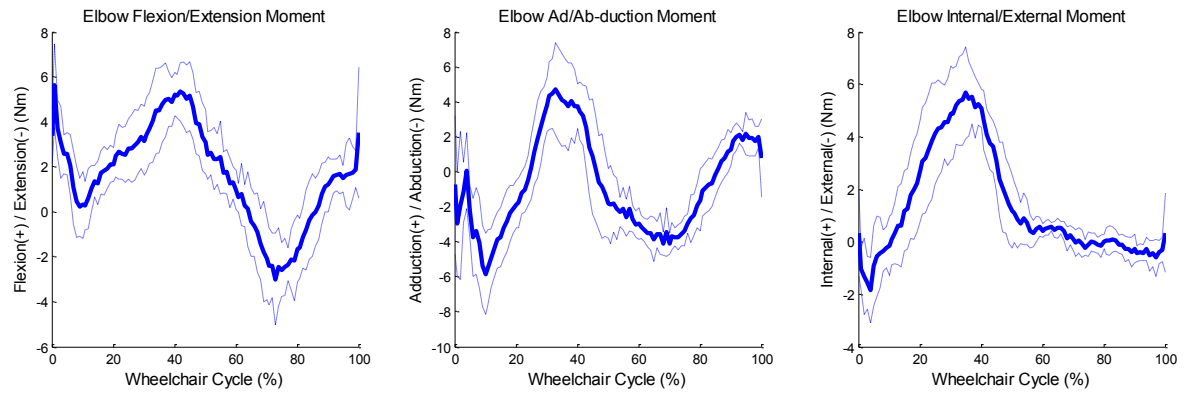


Figure 21: Mean (**bold**) and +/- 1 STDEV (dashed) right elbow joint moments during the stroke cycle for 10 stroke cycles.

Table 15: Mean (STDEV) maximum and minimum moments and moment range for the right elbow, in all planes of motion.

Right Elbow Joint	Sagittal Plane	Location (SD) (%)	Coronal Plane	Location (SD) (%)	Transverse Plane	Location (SD) (%)
	Flexion (+) / Extension (-)		Adduction (+) / Abduction (-)		Internal (+) / External (-)	
Max Moment (SD) (Nm)	7.26 (1.40)	22.2% (21.61)	6.00 (1.76)	41.3% (19.54)	6.36 (0.97)	38.8% (3.97)
Min Moment (SD) (Nm)	-4.20 (1.44)	75.8% (3.82)	-7.14 (2.17)	13.7% (14.10)	-2.58 (0.94)	4.4% (1.65)
Moment Range (SD) (Nm)	11.46 (1.70)		13.14 (2.03)		8.94 (1.30)	

Glenohumeral Joint Moment - Right Side

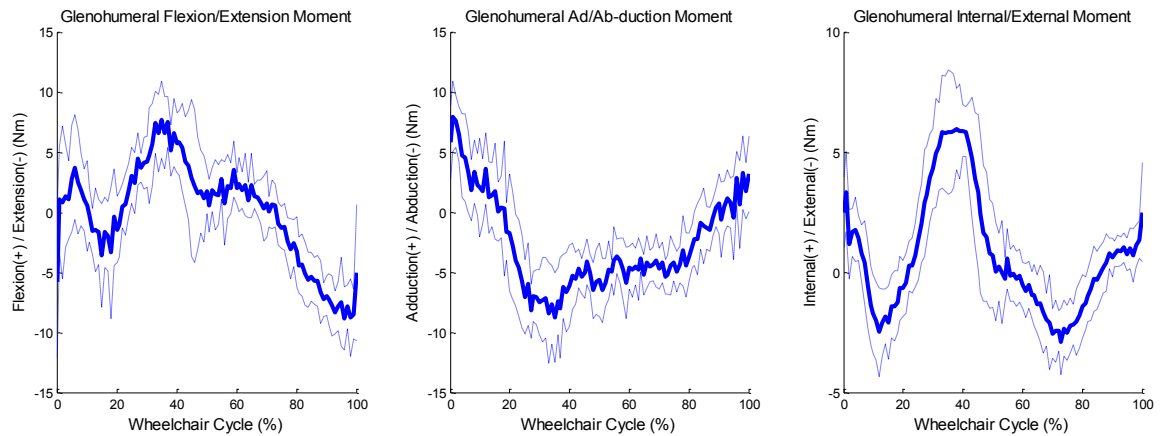


Figure 22: Mean (**bold**) and ± 1 STDEV (dashed) right glenohumeral joint moments during the stroke cycle for 10 stroke cycles.

Table 16: Mean (STDEV) maximum and minimum moments and moment range for the glenohumeral joint, in all planes of motion.

Right Glenohumeral Joint	Sagittal Plane	Location (SD) (%)	Coronal Plane	Location (SD) (%)	Transverse Plane	Location (SD) (%)
	Flexion (+) / Extension (-)		Adduction (+) / Abduction (-)		Internal (+) / External (-)	
Max Moment (SD) (Nm)	10.49 (1.87)	35.6% (12.04)	9.61 (2.85)	4.5% (5.36)	7.89 (1.23)	31.3% (16.26)
Min Moment (SD) (Nm)	-10.79 (3.02)	94% (18.32)	-11.76 (3.33)	42.2% (8.44)	-4.42(1.19)	43.8% (30.68)
Moment Range (SD) (Nm)	21.27 (4.48)		21.36 (5.64)		12.31 (1.49)	

2.4 Discussion

2.4.1 Kinematics

The wrist joint is always in a state of extension, with an average maximum and minimum angle of -27.41 (4.15) degrees and -60.21 (6.76) degrees respectively, on the subject's right side and -20.21 (8.92) degrees and -56.26 (2.82) degrees respectively, on the left side. The resulting wrist joint's average range of motion was 32.8 (6.18) degrees and 36.05 (9.19) degrees on the right and left sides respectively. It is interesting to note that the wrist is in its largest extension rotation and ulnar deviation occur at almost the same point, around 20 to 25% of the stroke cycle. The maximum and minimum angles in

the coronal plane (ulnar and radial deviations) of the left and right wrists are significantly different ($p<0.01$); however their ranges of motion are not significantly different, suggesting that the kinematic stroke pattern is similar, but shifted, particularly the left wrist towards ulnar deviation by about 6 degrees. This may be seen visually in the coronal plane wrist joint kinematic graph of Figure 9. Additionally, the minimum angle and range of motion of the left and right wrists are significantly different ($p<0.01$), at -11.31 (1.61) and 12.70 (3.04) degrees for the left side and -8.48 (2.28) and 8.03 (2.32) degrees for the right side. The left wrist experienced a greater minimum angle (greater external wrist rotation), and thus greater range of motion, than the right wrist.

The elbow joint is in a constant state of flexion and forearm pronation. The elbow flexion angle reaches an average maximum angle of 99.62 (2.32) degrees and 103.07 (1.51) degrees on the right and left sides respectively. The average minimum angle on the right and left sides is 53.61 (1.92) degrees and 55.69 (2.28) degrees respectively. The average peak elbow flexion angles also occurred around 20-25% of the stroke cycle, coinciding with the peak wrist extension and ulnar deviation angles. Additionally, the right forearm experiences a significantly greater ($P<0.01$) range of motion than the left forearm, 77.03 (8.02) degrees versus 47.66 (10.16) degrees respectively. This is a result of a significantly smaller ($p<0.01$) minimum pronation angle of the right forearm: 20.54 (2.75) degrees versus 49.68 (12.42) degrees of the left forearm.

The glenohumeral joint experiences its largest range of motion in the sagittal plane, with 54.39 (4.46) degrees on the right side and 57.09 (5.37) degrees on the left side. The average minimum glenohumeral angle for the right and left sides reaches -36.67 (3.95) degrees and -36.16 (1.41) degrees of extension respectively. The minimum glenohumeral

angle in the coronal plane for the right and left sides reached -31.68 (3.80) degrees and -44.74 (3.17) degrees of abduction. Additionally, the right glenohumeral joint reaches an average maximum angle of 52.30 (7.74) degrees of internal rotation. All three of these maximums occur almost simultaneously. This extreme position of glenohumeral extension, abduction and internal rotation occurs within the first 10-25% of the stroke cycle, almost coincident with the extreme positions of the elbow and wrist joints. While the sagittal plane motion of the glenohumeral joint may be considered the same for the left and right sides, the coronal and transverse plane motions are significantly different ($p < 0.01$) for the maximum and minimum angles, as well as the ranges of motion. In the coronal plane the right glenohumeral joint experiences a much greater range of motion, 26.79 (2.94) degrees, than the left glenohumeral joint, 12.84 (4.42) degrees, both entirely comprising abduction. This is largely in part due to the significant difference between the left and right maximum angles, -31.90 (2.75) degrees and -4.88 (2.28) degrees respectively. The transverse plane experiences a similar situation, with the right glenohumeral joint range of motion 52.48 (10.00), significantly larger than the left glenohumeral joint range of motion 28.21 (9.69), both almost exclusively internally rotation. Again this is due to the much greater maximum angle occurring at the right glenohumeral joint, 52.30 (7.74) degrees, versus 39.97 (7.71) degrees at the left glenohumeral joint.

The acromioclavicular joint experiences significant differences between the left and right sides for the maximum and minimum angles experienced in the sagittal and coronal planes, the minimum angle occurring in the transverse planes and the joint range of motion in both the coronal and transverse planes. The only measurements determined to

be similar between the left and right acromioclavicular joints are the range of motion experienced in the sagittal plane and the maximum angles experienced in the transverse plane. The sagittal plane acromioclavicular joint ranges of motion are 16.73 (2.15) degrees and 16.85 (4.57) degrees for the right and left sides respectively; however, there is approximately a 10 degree shift towards joint flexion for the right acromioclavicular joint, with a average maximum flexion angle of 46.99 (6.19) degrees. Additionally, while the average maximum angles for the left and right acromioclavicular joints in the transverse plane are similar, 21.54 (2.87) and 21.36 (2.28) respectively, the right acromioclavicular joint experiences a greater range of motion 18.23 (2.78) degrees versus 14.06 (2.57) degrees on the left side, due to a smaller average minimum angle. So, right acromioclavicular rotation in the sagittal plane is shifted to greater degree of flexion than the left side by about 10 degrees. The right acromioclavicular rotation in the coronal plane is shifted towards abduction by approximately 5 to 7 degrees versus the left acromioclavicular joint, which is adducted the entire stroke cycle.

While there was a great amount of discrepancies between the left and right acromioclavicular joint motions, the left and right sternoclavicular joint motions are very similar. The only significant difference ($p < 0.01$) was the average maximum angle experienced in the coronal plane, 2.14 (3.73) degrees and -1.66 (1.73) degrees for the right and left joints respectively. The right sternoclavicular joint experiences a small amount of depression, while the left sternoclavicular joint is slightly elevated over the entire stroke cycle.

The thorax, while not an actual joint, also had its motions analyzed. In the sagittal plane the thorax experienced an average range of motion of 11.74 (1.70) degrees and was

in a state of flexion (or forward bend) throughout the entire stroke cycle. Additionally, the thorax was consistently rotated in the transverse plane and laterally bent in the coronal plane to the subject's left side. This may suggest that the subject is working harder with his right side and incorporating his thorax to assist. This could account for the multitude of kinematic asymmetries observed between the joints of the left and right sides of the body.

2.4.2 Kinetics

The wrist joint experiences medial shear force (z-axis) and posterior shear force (x-axis) and tension in the superior/inferior direction (y-axis) during the push phase of the wheelchair stroke cycle. The average maximum forces for each plane: 38.25 (6.75) N medial shear, -43.03 (2.75) N posterior shear and 24.44 (9.50) N tension, were reached during 15-30% of the wheelchair stroke cycle. So although the amount of force in each plane is not a large amount, the fact that the peak forces are occurring during the same points as the extreme wrist rotations, is a cause for concern. The right wrist moments revealed that the wrist experiences an average maximum extension moment of -6.79 (1.46) Nm and an average maximum internal rotation moment of 9.05 (0.72) Nm. The peak extension moment occurs at approximately 23% of the stroke cycle, while the peak internal rotation moment occurs closer to 34% of the stroke cycle.

The elbow joint also experiences medial shear force and posterior shear force; however, it primarily experiences compression in the superior/inferior axis. The average peak forces at the elbow joint: 44.51 (6.38) N medial shear, -40.5 (7.29) N posterior shear and -24.75 (3.45) N compression along the superior/inferior axes respectively, all occur around 15-30% of the wheelchair stroke cycle. The moments occurring at the right elbow

exhibit an average maximum flexion moment in the sagittal plane of 7.26 (1.40) Nm at 22.2% of the stroke cycle, an average maximum adduction and abduction moments in the coronal plane of 6.00 (1.76) Nm at 41.3% stroke cycle and -7.14 (2.17) Nm at 13.7% cycle and an average internal rotation moment in the transverse plane of 6.36 (0.97) Nm at 38.8% cycle.

The right glenohumeral joint experiences primarily medial shear force along the medial/lateral axis and tension along the superior/inferior axis, and both anterior and posterior shear forces. Peak forces were: 54.24 (8.80) N medial shear force at 23.4% stroke cycle, 31.20 (4.38) N anterior shear force at 27.2% stroke cycle and 61.86 (10.87) N of tension at 20.3% cycle. All three peak forces occurred within 7% of the stroke cycle of one another. The moments experienced at the glenohumeral joint are the largest of the three kinetically analyzed joints. The sagittal plane has an average maximum flexion moment of 10.49 (1.87) Nm and extension moment of -10.79 (3.02) Nm. The flexion moment maximum occurs on average at 35.6% of the stroke cycle, similar to the peak elbow moment occurrences, while the peak glenohumeral extension moment occurs right around initial contact. In the coronal plane, the glenohumeral joint exhibits an average maximum adduction moment of 9.61 (2.85) Nm during initial contact and an average maximum abduction moment of -11.76 (3.33) Nm at 42.2% stroke cycle. Lastly, in the transverse plane, the glenohumeral joint experiences maximum internal and external rotation moments of 7.89 (1.23) Nm at 31.3% of the stroke cycle and -4.42 (1.19) Nm at 43.8% stroke cycle, respectively.

2.4.3 Summary

The data highlights the problematic area of about 20% wheelchair stroke cycle. This is believed to be approximately when the user's hand reaches top, center of the pushrim during the push phase of the stroke cycle. Additionally, when looking at the moment data, the elbow and glenohumeral joints experience peak moments near 40% stroke cycle, which is close to the end of the push phase, which transitioned to the recovery phase at 52.7% of the stroke cycle on average. This point in the propulsion cycle should also be considered problematic as these peak moments occurring simultaneously, and repetitively, may be indicative of elbow or shoulder pain and pathologies.

The extreme wrist joint angles, compounded with simultaneous peak loading on the wrist joint and the repetitive nature of wheelchair propulsion, suggested that this particular subject may benefit from an alternative pushing method. Due to the outcomes of this work, the subject received a push-activated power assist system in order to reduce the onset of wrist pathologies such as carpal tunnel syndrome.

Chapter 4: CONCLUSION

4.1 Summary

The primary goal of this work was to create a pediatric upper extremity biomechanical model in order to analyze wheelchair mobility. This goal has been accomplished. The model has been developed and used to analyze the UE motion of the thorax, AC, SC, GH, elbow and wrist joints, as well as the forces and moments at the GH, elbow and wrist joints of children whom use manual wheelchairs as their primary method of mobility. This data was described in all three planes of motion for each joint. It is hoped that this work will allow for further research and clinical opportunities in UE motion analysis of children using manual wheelchair to ultimately reduce or eliminate UE pathology and improve treatment, long-term outcomes and transitional care.

4.2 Future Work

With the amount of information that this model collects, many additions may be made to further knowledge of this pediatric population. A short list a potential future work is provided:

1. Obtain a second SmartWheel and use the model bilaterally, and investigate bilateral differences and effects due to hand dominance.
2. Analyze the effects of the shoulder girdle joints (AC, SC and GH) and the impact of each joint on the onset and development of shoulder pathology and pain.
3. Determine and implement a way to collect kinetic data for the AC and SC joints.
4. Assess energy demands and possible effects of conditioning.

5. Begin to assess various treatment possibilities. Examine what biomechanical differences occur when: different wheelchairs are used, wheelchair set-up is altered (seat height, camber, axle position, etc.), subject receives strength conditioning, etc.
6. Rework the assistive device; consider improvements to manual wheelchair design.
7. Optimization of wheelchair prescription.
8. EMG data collection of pertinent muscles.
9. SIMM modeling with extension to FE modeling of the shoulder girdle.
10. Monitor and provide feedback to the MWU during community or at-home use.

4.3 Concluding Remarks

This research described a three-dimensional biomechanical model of the upper extremities specifically for pediatric evaluation during manual wheelchair mobility. The repetitive nature of wheelchair propulsion increases the concern of peak joint forces and joint moments occurring simultaneously with extreme joint positioning. Further work investigating the contribution of joint biomechanics to UE pain and pathology is required to identify and reduce potential risk factors and restore the quality of life.

REFERENCES

- [1] Kaye, H.S. et al. 2000. Mobility Device Use in the United States. Disability Statistics Report (14): 1-60. Washington, DC: US Dept Education, NIDRR.
- [2] Marini JC. Osteogenesis imperfecta. In: Kliegman RM, Behrman RE, Jenson HB, Stanton BF, eds. Nelson Textbook of Pediatrics. 19th ed. Philadelphia, Pa: Saunders Elsevier; 2011:chap 692.
- [3] Bax, M., Goldstein, M., Rosenbaum, P., Leviton, A., Paneth, N., Dan, B., Jacobsson, B., et al. (2005). Proposed definition and classification of cerebral palsy, April 2005. *Developmental medicine and child neurology*, 47(8), 571–6.
- [4] Mitchell, L. E., Adzick, N. S., Melchionne, J., Pasquariello, P. S., Sutton, L. N., & Whitehead, A. S. (2004). Spina bifida. *Lancet*, 364(9448), 1885–95.
- [5] Sekhon, L. H., & Fehlings, M. G. (2001). Epidemiology, demographics, and pathophysiology of acute spinal cord injury. *Spine*, 26(24 Suppl), S2–12.
- [6] Lusardi, M. M., Nielsen, C. C. (2000). Orthotics and Prosthetics in Rehabilitation. Butterworth-Heinemann, Boston, MA.
- [7] Schmeler, M., & Buning, M. E. (1999). Evaluation of Wheelchair Mobility and Seating: Seating Biomechanics. *Lecture Series on Application and Use of Wheelchair Technology*. Retrieved from http://www.wheelchairnet.org/WCN_WCU/SlideLectures/Lectures/lectures.html
- [8] Cooper, R. a, Koontz, A. M., Ding, D., Kelleher, A., Rice, I., & Cooper, R. (2010). Manual wheeled mobility--current and future developments from the human engineering research laboratories. *Disability and rehabilitation*, 32(26), 2210–21.
- [9] Koontz, A. M., Pearlman, J. L., Impink, B. C., Cooper, R. A., & Wilkinson, M. (2007). Wheelchairs. In W. J. G. (Ed.), *An Introduction to Rehabilitation Engineering* (1st ed., pp. 129–155). Boca Raton: Taylor & Francis.
- [10] Karp, G. (1998). *Choosing a Wheelchair: A guide for optimal independence* (1st ed., p. 186). O'Reilly Media.
- [11] Schmeler, M., & Buning, M. E. (2000). Evaluation of Wheelchair Mobility and Seating: Properties of Seat Cushions. *Lecture Series on Application and Use of Wheelchair Technology1*. Retrieved from http://www.wheelchairnet.org/WCN_WCU/SlideLectures/Lectures/lectures.html
- [12] Boninger, M. L., Baldwin, M., Cooper, R. A., Koontz, A., & Chan, L. (2000). Manual Wheelchair Pushrim Biomechanics and Axle Position. *Archives of physical medicine and rehabilitation*, 81(May), 608–13.
- [13] van der Woude, L. H., Veeger, D. J., Rozendal, R. H., & Sargeant, T. J. (1989). Seat height in handrim wheelchair propulsion. *Journal of rehabilitation research and development*, 26(4), 31–50.
- [14] Crane, B. (2007). Chapter 19: Adaptive Seating in the Management of Neuromuscular and Musculoskeletal Impairment. In Lusardi, M. M., & Nielsen, C. C. (2nd), *Orthotics and Prosthetics in Rehabilitation* (pp. 489-516). St. Louis: Saunders Elsevier.

- [15] Muscolino, J. E. (2010). *The Muscular System Manual: The Skeletal Muscles of the Human Body* (3rd ed.). Mosby Elsevier.
- [16] Neumann, D. A. (2009). *Kinesiology of the Musculoskeletal System: foundations for rehabilitation* (2nd ed., p. 752). Mosby Elsevier.
- [17] Rothstein, J. M., Roy, S., Wolf, S., Scalzitti, D., & Wolf, S. L. (2005). *The Rehabilitation Specialist's Handbook* (3rd ed.). F. A. Davis Company.
- [18] Ebaugh, D. D., McClure, P. W., & Karduna, A. R. (2005). Three-dimensional scapulothoracic motion during active and passive arm elevation. *Clinical biomechanics (Bristol, Avon)*, 20(7), 700–9.
- [19] Dayanidhi, S., Orlin, M., Kozin, S., Duff, S., & Karduna, A. (2005). Scapular kinematics during humeral elevation in adults and children. *Clinical biomechanics (Bristol, Avon)*, 20(6), 600–6.
- [20] McClure, P. W. et al. (2006). Shoulder function and 3-dimensional scapular kinematics in people with and without shoulder impingement syndrome. *Physical therapy*, 86(8), 1075-90.
- [21] van der Helm, F. C. T., & Pronk, G. M. (1995). Three-Dimensional Recording and Description of Motions of the Shoulder Mechanism. *Journal of Biomechanical Engineering*, 117, 27–40.
- [22] Anglin, C., & Wyss, U. P. (2000). Review of arm motion analyses. *Proceedings of the Institution of Mechanical Engineers, Part H: Journal of Engineering in Medicine*, 214(5), 541–555.
- [23] Mercer, J. L., Boninger, M., Koontz, A., Ren, D., Dyson-Hudson, T., & Cooper, R. (2006). Shoulder joint kinetics and pathology in manual wheelchair users. *Clinical biomechanics (Bristol, Avon)*, 21(8), 781–9.
- [24] Veeger, H. E. J., Meershoek, L. S., van der Woude, L. H. V., & Langenhoff, J. M. (1998). Wrist motion in handrim wheelchair propulsion. *Journal of rehabilitation research and development*, 35(3), 305–13.
- [25] Pentland, W. E., & Twomey, L. T. (1991). The weight-bearing upper extremity in women with long term paraplegia. *Paraplegia*, 29(8), 521-30.
- [26] Ballinger, D. A. et al. (2000). The relation of shoulder pain and range-of-motion problems to functional limitations, disability, and perceived health of men with spinal cord injury: a multifaceted longitudinal study. *Archives of physical medicine and rehabilitation*, 81(12), 1575-81.
- [27] Lundqvist C. et al. (1991). Spinal cord injuries. Clinical, functional, and emotional status. *Spine*, 16, 78-83.
- [28] Shimada, S.D., Robertson, R.N., Bonninger, M.L., Cooper, R.A. (1998). Kinematic characterization of wheelchair propulsion. *Journal of Rehabilitation Research and Development*. 35 (2), 210-218.
- [29] Sanderson, D. J., & Sommer III, H. J. (1985). Kinematic features of wheelchair propulsion. *Journal of Biomechanics*, 18(6), 423–429.
- [30] Veeger, H. E. J., van der Woude, L. H. V., & Rozendal, R. H. (1989). Wheelchair propulsion technique at different speeds. *Scandinavian Journal of Rehabilitation Medicine*, 21(4), 197–203.
- [31] Boninger, M. L., Souza, A. L., Cooper, R. a., Fitzgerald, S. G., Koontz, A. M., &

- Fay, B. T. (2002). Propulsion patterns and pushrim biomechanics in manual wheelchair propulsion. *Archives of Physical Medicine and Rehabilitation*, 83(5), 718–723.
- [32] Koontz, Alicia M and Boninger, Michael L (2003) Proper propulsion. *Rehab management*, 16 (6). pp. 18-22.
- [33] Boninger, M. L., Koontz, A. M., Sisto, S. A., Dyson-Hudson, T. A., Chang, M., Price, R., & Cooper, R. A. (2005). Pushrim biomechanics and injury prevention in spinal cord injury: Recommendations based on CULP-SCI investigations. *Journal of Rehabilitation Research and Development*, 42(3), 9–20.
- [34] Betz, K. (2007). Pushing a Wheelchair: Simple Task — or Accomplished Skill. *Paraplegia News*, (March), 30–35.
- [35] Boninger, M. L., Cooper, R. A., Robertson, R. N., & Rudy, T. E. (1997). Wrist biomechanics during two speeds of wheelchair propulsion: an analysis using a local coordinate system. *Archives of physical medicine and rehabilitation*, 78(4), 364–72.
- [36] Corfman, T. A., Cooper, R. A., Boninger, M. L., Koontz, A. M., & Fitzgerald, S. G. (2003). Range of Motion and stroke frequency differences between manual wheelchair propulsion and pushrim-activated power-assisted wheelchair propulsion. *The Journal of Spinal Cord Medicine*, 26(2), 135–140.
- [37] Laurence, R., Sylvain, H., & Agnes, R.-B. (2006). Shoulder movements during the initial phase of learning manual wheelchair propulsion in able-bodied subjects. *Clinical biomechanics*, 21, S45–S51.
- [38] Vanlandewijck, Y. C., Spaepen, A. J., & Lysens, R. J. (1994). Wheelchair propulsion efficiency: movement pattern adaptations to speed changes. *Medicine and Science in Sports and Exercise*, 26(11), 1373–1381.
- [39] Rao, S. S., Bontrager, E. L., Gronley, J. K., Newsam, C. J., & Perry, J. (1996). Three-Dimensional Kinematics of Wheelchair Propulsion. *IEEE Transactions on Rehabilitation Engineering*, 4(3), 152–160.
- [40] Wei, S., Huang, S.-L., Jiang, C.-J., & Chiu, J.-C. (2003). Wrist kinematic characterization of wheelchair propulsion in various seating positions: implication to wrist pain. *Clinical Biomechanics*, 18(6), S46–S52.
- [41] Boninger, M. L., Cooper, R. A., Shimada, S. D., & Rudy, T. E. (1998). Shoulder and elbow motion during two speeds of wheelchair propulsion: a description using a local coordinate system. *Spinal cord*, 36(6), 418–26.
- [42] Davis, J. L., Growney, E. S., Johnson, M. E., Iuliano, B. A., & An, K. N. (1998). Three-dimensional kinematics of the shoulder complex during wheelchair propulsion: a technical report. *Journal of rehabilitation research and development*, 35(1), 61–72.
- [43] Finley, M. a, Rasch, E. K., Keyser, R. E., & Rodgers, M. M. (2004). The biomechanics of wheelchair propulsion in individuals with and without upper-limb impairment. *Journal of rehabilitation research and development*, 41(3B), 385–95.
- [44] Collinger, J. L., Boninger, M. L., Koontz, A. M., Price, R., Sisto, S. A., Tolerico,

- M. L., & Cooper, R. A. (2008). Shoulder Biomechanics During the Push Phase of Wheelchair Propulsion : A Multisite Study of Persons With Paraplegia. *Archives of physical medicine and rehabilitation*, 89(4), 667–76.
- [45] Campbell, a C., Lloyd, D. G., Alderson, J. a, & Elliott, B. C. (2009). MRI development and validation of two new predictive methods of glenohumeral joint centre location identification and comparison with established techniques. *Journal of biomechanics*, 42(10), 1527–32.
- [46] Meskers, C. G., van der Helm, F. C., Rozendaal, L. a, & Rozing, P. M. (1998). In vivo estimation of the glenohumeral joint rotation center from scapular bony landmarks by linear regression. *Journal of biomechanics*, 31(1), 93–6.
- [47] Wu, G., van der Helm, F. C. T., Veeger, H. E. J. D., Makhsous, M., Van Roy, P., Anglin, C., Nagels, J., et al. (2005). Recommendation on definitions of joint coordinate systems of various joints for the reporting of human joint motion - Part II: shoulder, elbow, wrist and hand. *Journal of Biomechanics*, 38, 981–992.
- [48] International Society of Biomechanics. (n.d.). Retrieved from <http://isbweb.org/>
- [49] Raina, S., McNitt-Gray, J. L., Mulroy, S., & Requejo, P. S. (2011). Effect of increased load on scapular kinematics during manual wheelchair propulsion in individuals with paraplegia and tetraplegia. *Human movement science*.
- [50] McClure, P. W., Michener, L. a, Sennett, B. J., & Karduna, a R. (2001). Direct 3-dimensional measurement of scapular kinematics during dynamic movements in vivo. *Journal of shoulder and elbow surgery / American Shoulder and Elbow Surgeons ... [et al.]*, 10(3), 269–77.
- [51] Lal, S. (1998). Premature degenerative shoulder changes in spinal cord injury patients. *Spinal Cord*, 36, 186–189.
- [52] Bayley, J. C., Cochran, T. P., & Sledge, C. B. (1987). The Weight-Bearing Shoulder. *The Journal of Bone and Joint Surgery*, 69-A(5), 676–678.
- [53] Lee, T. Q., & McMahon, P. J. (2002). Shoulder biomechanics and muscle plasticity: implications in spinal cord injury. *Clinical Orthopaedics and Related Research*, 403(Supplement), S26–36.
- [54] Morrow, M. M. B., Kaufman, K. R., & An, K.-N. (2011). Scapula kinematics and associated impingement risk in manual wheelchair users during propulsion and a weight relief lift. *Clinical biomechanics (Bristol, Avon)*, 26(4), 352–7.
- [55] Finley, M. a, McQuade, K. J., & Rodgers, M. M. (2005). Scapular kinematics during transfers in manual wheelchair users with and without shoulder impingement. *Clinical biomechanics (Bristol, Avon)*, 20(1), 32–40.
- [56] Ludewig, P. M., & Cook, T. M. (2000). Alterations in shoulder kinematics and associated muscle activity in people with symptoms of shoulder impingement. *Physical therapy*, 80(3), 276–91.
- [57] Koontz, A. M., Cooper, R. a., Boninger, M. L., Souza, A. L., & Fay, B. T. (2004). Scapular range of motion in a quasi-wheelchair push. *International Journal of Industrial Ergonomics*, 33(3), 237–248.
- [58] Bednarczyk, J. H., & Sanderson, D. J. (1995). Limitations of kinematics in the assessment of wheelchair propulsion in adults and children with spinal cord injury. *Physical therapy*, 75(4), 281-9.
- [59] Cooper, R. A. (2009). SMARTWheel: From concept to clinical practice.

- Prosthetics and orthotics international*, 33(3), 198-209.
- [60] SmartWheel User's Guide 2010. (2009). (3.0 ed., p. 61). Mesa, AZ: Three Rivers.
 - [61] Gagnon, D., Nadeau, S., Noreau, L., Dehail, P., & Pottie, F. (2008). Comparison of peak shoulder and elbow mechanical loads during weight-relief lifts and sitting pivot transfers among manual wheelchair users with spinal cord injury. *The Journal of Rehabilitation Research and Development*, 45(6), 863–874.
 - [62] van Drongelen, S., van der Woude, L. H., Janssen, T. W., Angenot, E. L., Chadwick, E. K., & Veeger, D. H. (2005). Glenohumeral Contact Forces and Muscle Forces Evaluated in Wheelchair-Related Activities of Daily Living in Able-Bodied Subjects Versus Subjects With Paraplegia and Tetraplegia. *Archives of Physical Medicine and Rehabilitation*, 86(7), 1434–1440.
 - [63] Morrow, M. M. B., Hurd, W. J., Kaufman, K. R., & An, K.-N. (2010). Shoulder Demands in Manual Wheelchair Users Across a Spectrum of Activities. *Journal of Electromyography and Kinesiology*, 20(1), 61–67.
 - [64] Robertson, R. N., Boninger, M. L., Cooper, R. A., & Shimada, S. D. (1996). Pushrim Forces and Joint Kinetics During Wheelchair Propulsion. *Archives of physical medicine and rehabilitation*, 77(September), 856–864.
 - [65] Desroches, G., Dumas, R., Pradon, D., Vaslin, P., Lepoutre, F.-X., & Chèze, L. (2010). Upper limb joint dynamics during manual wheelchair propulsion. *Clinical biomechanics (Bristol, Avon)*, 25(4), 299–306.
 - [66] Gil-Agudo, A., Del Ama-Espinosa, A., Pérez-Rizo, E., Pérez-Nombela, S., & Pablo Rodríguez-Rodríguez, L. (2010). Upper limb joint kinetics during manual wheelchair propulsion in patients with different levels of spinal cord injury. *Journal of biomechanics*, 43(13), 2508–15.
 - [67] Koontz, A. M., Cooper, R. a, Boninger, M. L., Souza, A. L., & Fay, B. T. (2002). Shoulder kinematics and kinetics during two speeds of wheelchair propulsion. *Journal of rehabilitation research and development*, 39(6), 635–49.
 - [68] Kulig, K., Newsam, C. J., Mulroy, S. J., Rao, S., Gronley, J. K., Bontrager, E. L., & Perry, J. (2001). The effect of level of spinal cord injury on shoulder joint kinetics during manual wheelchair propulsion. *Clinical biomechanics (Bristol, Avon)*, 16(9), 744–51.
 - [69] Gil-Agudo, A., Del Ama-Espinosa, A., Pérez-Rizo, E., Pérez-Nombela, S., & Crespo-Ruiz, B. (2010). Shoulder joint kinetics during wheelchair propulsion on a treadmill at two different speeds in spinal cord injury patients. *Spinal cord*, 48(4), 290–6.
 - [70] van Drongelen, S., van der Woude, L. H. V., & Veeger, H. E. J. (2011). Load on the shoulder complex during wheelchair propulsion and weight relief lifting. *Clinical biomechanics (Bristol, Avon)*, 26(5), 452–7.
 - [71] van der Helm, F. C. T. (1997). A three-dimensional model of the shoulder and elbow. *First Conference of the ISG* (pp. 65–70).
 - [72] Riek, L. M., Ludewig, P. M., & Nawoczenski, D. a. (2008). Comparative shoulder

- kinematics during free standing, standing depression lifts and daily functional activities in persons with paraplegia: considerations for shoulder health. *Spinal cord*, 46(5), 335–43.
- [73] Kwarciak, A. M., Turner, J. T., Guo, L., & Richter, W. M. (2011). Comparing handrim biomechanics for treadmill and overground wheelchair propulsion. *Spinal cord*, 49(3), 457–62.
- [74] Rice, I., Impink, B., Niyonkuru, C., & Boninger, M. (2009). Manual wheelchair stroke characteristics during an extended period of propulsion. *Spinal cord*, 47(5), 413–7.
- [75] Rodgers, M. M., Keyser, R. E., Rasch, E. K., Gorman, P. H., & Russell, P. J. (2001). Influence of training on biomechanics of wheelchair propulsion. *Journal of rehabilitation research and development*, 38(5), 505–11.
- [76] McClure, P. W., Bialker, J., Neff, N., Williams, G., & Karduna, A. (2004). Shoulder function and 3-dimensional kinematics in people with shoulder impingement syndrome before and after a 6-week exercise program. *Physical therapy*, 84(9), 832–48.
- [77] Kwarciak, A. M., Sisto, S. A., Yarossi, M., Price, R., Komaroff, E., & Boninger, M. L. (2009). Redefining the manual wheelchair stroke cycle: identification and impact of nonpropulsive pushrim contact. *Archives of physical medicine and rehabilitation*, 90(1), 20–6.
- [78] Brown, D. D., Knowlton, R. G., Hamill, J., Schnieder, T. L., & Hetzler, R. K. (1990). Physiological and biomechanical differences between wheelchair-dependent and able-bodied subjects during wheelchair ergometry. *European Journal of Applied Physics*, 60(3), 179–182.
- [79] Slavens, B., Graf, A., Krzak, J., Vogel, L., & Harris, G. F. (2011). Upper Extremity Wheelchair Kinematics in Children with Spinal Cord Injury. *Conference Proceedings IEEE Engineering in Medicine and Biology Society* (pp. 8158–8161).
- [80] Slavens, B., Sturm, P., Bajournate, R., & Harris, G. F. (2009). Upper extremity dynamics during Lofstrand crutch-assisted gait in children with myelomeningocele. *Gait & Posture*, 30(4), 511–517.
- [81] Slavens, B., Bhagchandani, N., Wang, M., Smith, P. A., & Harris, G. F. (2011). An Upper Extremity Inverse Dynamics Model for Pediatric Lofstrand Crutch-Assisted Gait. *Journal of Biomechanics*, 44(11), 2162–2167.
- [82] Slavens, B., Paul, A., Graf, A., Krzak, J., Vogel, L., & Harris, G. F. (2012). Upper extremity kinematics in children with spinal cord injury during wheelchair mobility. *Gait and Clinical Motion Analysis Society Annual Conference* (pp. 79–80).
- [83] Šenk, M., & Chèze, L. (2010). A new method for motion capture of the scapula using an optoelectronic tracking device: a feasibility study. *Computer methods in biomechanics and biomedical engineering*, 13(3), 397–401.
- [84] Hingtgen, B., McGuire, J. R., Wang, M., & Harris, G. F. (2006). An upper extremity kinematic model for evaluation of hemiparetic stroke. *Journal of biomechanics*, 39(4), 681–8.
- [85] Nguyen, T. C., & Baker, R. (2004). Two methods of calculating thorax

- kinematics in children with myelomeningocele. *Clinical biomechanics*, 19(10), 1060-5.
- [86] Rab, G., Petuskey, K., & Bagley, A. (2002). A method for determination of upper extremity kinematics. *Gait & posture*, 15(2), 113–9.
 - [87] Karduna, A. R., McClure, P. W., Michener, L. A., & Sennett, B. (2001). Dynamic Measurements of Three-Dimensional Scapular Kinematics: A Validation Study. *Journal of Biomechanical Engineering*, 123(2), 184–90.
 - [88] Cheze, L., Fregly, B. J., & Dimnet, J. (1995). A solidification procedure to facilitate kinematic analyses based on video system data. *Journal of Biomechanics*, 28(7), 879–884.
 - [89] Veldpaus, F. E., Woltring, H. J., & Dortmans, L. J. M. G. (1988). A least-squares algorithm for the equiform transformation from spatial marker co-ordinates. *Journal of Biomechanics*, 21(1), 45–54.
 - [90] Winter, D., 2005. *Biomechanics and Motor Control of Human Movement* (3rd ed.). Wiley-Interscience, Toronto, Ontario.
 - [91] Ganley, K. (2004). Determination of lower extremity anthropometric parameters using dual energy X-ray absorptiometry: the influence on net joint moments during gait. *Clinical Biomechanics*, 19(1), 50-56.
 - [92] Dillon, M. P., & Hons, B. P. O. (2008b). Effect of inaccuracies in anthropometric data and linked-segment inverse dynamic modeling on kinetics of gait in persons with partial foot amputation. *Changes*, 45(9), 1303-1316.
 - [93] Rao, G., Amarantini, D., Berton, E., & Favier, D. (2006). Influence of body segments' parameters estimation models on inverse dynamics solutions during gait. *Journal of Biomechanics*, 39(8), 1531–1536.
 - [94] Jaffrey, M. A. (2008). *Estimating Centre of Mass Trajectory and Subject-Specific Body Segment Parameters Using Optimisation Approaches*. Unpublished doctoral dissertation, Victoria University, Melbourne, Australia.
 - [95] Jensen, R. K. (1986). Body segment mass, radius and radius of gyration proportions of children. *Journal of Biomechanics*, 19(5), 359–368.
 - [96] Yeadon, M. R., & Morlock, M. (1989). The appropriate use of regression equations for the estimation of segmental inertia parameters. *Journal of Biomechanics*, 22(6/7), 683–689.
 - [97] Dempster, W. T. (1955). Space requirements of the seated operator. WADC Technical Report (TR-55-159). Wright-Patterson Air Force Base, OH.
 - [98] Clauser, C.E., McConville, J.T., Young, J.W. (1969) Weight, Volume and Center of Mass of Segments of the Human Body. AMRL Technical Report (TR-60-70), Wright-Patterson Air Force Base, Ohio.
 - [99] Chandler, R.F., Clauser, C.E., McConville, J.T., Reynolds, H.M., Young, J.W., (1975). Investigation of inertial properties of the human body. AMRL Technical Report (TR-74-137), Wright-Patterson Air Force Base, Ohio.
 - [100] Jensen, R. K. (1989). Changes in segment inertia proportions between 4 and 20 years. *Journal of Biomechanics*, 22(6/7), 529–536.
 - [101] Snyder, R. G., Schnieder, L. W., Owing, C. L., Reynolds, H. M., Golomb, D. H., & Schork, M. A. (1977). *Anthropometry of Infants, Children and Youths to Age 18 for Product Safety Design*. Society of Automotive Engineers (p. 640). Warrendale: Society of Automotive Engineers Inc.

- [102] Jensen, R. K., & Nassas, G. (1988). Growth of segment principal mometns of inertia between four and twenty years. *Medicine and Science in Sports and Exercise*, 20(6), 594–604.
- [103] Ming, D., Liu, X. Y., Bai, Y. R., Zhang, G. J., Cheng, L. L., Qi, H. Z., Xue, Z. J., et al. (2009). Measurement of upper extremity joint moments in walker-assisted gait. *IET Science, Measurement & Technology*, 3(5), 343–53.
- [104] Bachschmidt, R. a, Harris, G. F., & Simoneau, G. G. (2001). Walker-assisted gait in rehabilitation: a study of biomechanics and instrumentation. *IEEE transactions on neural systems and rehabilitation engineering : a publication of the IEEE Engineering in Medicine and Biology Society*, 9(1), 96–105.
- [105] Lloyd, D. G., Alderson, J., & Elliott, B. C. (2000). An upper limb kinematic model for the examination of cricket bowling: a case study of Mutiah Muralitharan. *Journal of sports sciences*, 18(12), 975–82.
- [106] Strifling, K. M. B., Lu, N., Wang, M., Cao, K., Ackman, J. D., Klein, J. P., Schwab, J. P., et al. (2008). Comparison of upper extremity kinematics in children with spastic diplegic cerebral palsy using anterior and posterior walkers. *Gait & posture*, 28(3), 412–419.
- [107] Schmidt, R., Disselhorst-Klug, C., Silny, J., & Rau, G. (1999). A marker-based measurement procedure for unconstrained wrist and elbow motions. *Journal of biomechanics*, 32(6), 615–21.
- [108] Baker, R. (2001). Pelvic angles: a mathematically rigorous definition which is consistent with a conventional clinical understanding of the terms. *Gait & posture*, 13(1), 1–6.
- [109] Zatsiorsky, V. M. (2002). *Kinetics of Human Motion*. Champaign, IL: Human Kinetics.
- [110] Sutherland, D. H. (2002). The evolution of clinical gait analysis Part II Kinematics. *Gait and Posture*, 16, 159–179.

Appendices

Appendix 1: Yeadon and Morlock Inertia Calculations

The following table describes the required subject specific measurements

Segment	Variable	Definition
Upper arm	h	Length: shoulder center to elbow center
	p_1	Perimeter: below axilla
	p_2	Perimeter: maximum
	p_3	Perimeter: elbow
Forearm	h	Length: elbow center to wrist center
	p_1	Perimeter: elbow
	p_2	Perimeter: maximum
	p_3	Perimeter: wrist
Hand	h	Length: wrist center to tip of finger III
	p_1	Perimeter: wrist
	p_2	Perimeter: metacarpal-phalangeal joints

For the upper arm and forearm the mean perimeter, p , is calculated as:

$$p = \frac{(p_1 + 2p_2 + p_3)}{4}$$

For the hand the mean perimeter, p , is calculated as:

$$p = \frac{(p_1 + p_2)}{2}$$

For each segment, the segmental moments of inertia, I_z and I_t , about the longitudinal and transverse axes are given by:

$$I_z = k_1 p^4 h$$

$$I_t = \frac{1}{2} I_z + k_2 p^2 h^3$$

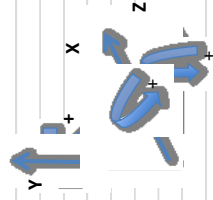
Where linear measurements are in meters and the moments of inertia are in kgm^2

The constants, k_1 and k_2 are given for each segment below:

Segment	k_1	k_2
Upper arm	0.979	6.11
Forearm	0.810	4.98
Hand	1.309	7.68

From Yeadon and Morlock [96].

Appendix 2: Sign Convention

Table 17: Explanation of sign convention used for joint angles, forces and moments			
	Plane		
Angle	X - Coronal		
Thorax (no sides)	Lean R +/Lean L -	Y - Transverse	Z - Sagittal
		Axial Rotation Left Twist +/Axial Rotation Right Twist -	Backward Extension +/ Forward Flexion -
Angle	Plane		
	X - Coronal	Y - Transverse	Z - Sagittal
Sternoclavicular	Depression +/ Elevation -	Internal Rotation +/External Rotation -	Restricted to zero, only two markers
Acromioclavicular	Downward Rotation + / Upward Rotation -	Protraction + / Retraction -	Posterior Tilt + / Anterior Tilt -
Glenohumeral	Adduction +/Abduction -	Internal Rotation +/External Rotation -	Flexion +/ Extension -
Elbow	Restricted to 0	Pronation +/Supination -	Flexion +/ Extension -
Wrist	Ulnar deviation +/Radial deviation -	Internal Rotation +/External Rotation -	Flexion +/ Extension -
Force	Plane		
	X - Coronal	Y - Transverse	Z - Sagittal
Glenohumeral	Anterior (Tension) +/ Posterior (Compression) -	Superior (Tension) +/ Inferior (Compression) -	Lateral (Tension) +/ Medial (Compression) -
Elbow	Anterior (Tension) +/ Posterior (Compression) -	Superior (Tension) +/ Inferior (Compression) -	Lateral (Tension) +/ Medial (Compression) -
Wrist	Anterior (Tension) +/ Posterior (Compression) -	Superior (Tension) +/ Inferior (Compression) -	Lateral (Tension) +/ Medial (Compression) -
Moment	Plane		
	X - Coronal	Y - Transverse	Z - Sagittal
Glenohumeral	Adduction +/Abduction -	Internal Rotation +/External Rotation -	Flexion +/ Extension -
Elbow	Adduction +/Abduction -	Pronation +/Supination -	Flexion +/ Extension -
Wrist	Ulnar deviation +/Radial deviation -	Internal Rotation +/External Rotation -	Flexion +/ Extension -
where	Z	lateral (right)	
	X	anterior	
	Y	superior	
			

Appendix 3: Source Code

A.3.1 Parameters

```

%%%%%%%%%%%%%%%%%%%%%%%%%%%%%%%%%%%%%%%%%%%%%%%%%%%%%%%%%%%%%%%%%%%%%%%%
%                               EDIT THIS FILE FOR EACH SUBJECT/TRIAL                               %
%%%%%%%%%%%%%%%%%%%%%%%%%%%%%%%%%%%%%%%%%%%%%%%%%%%%%%%%%%%%%%%%%%%%%%%%

%This file declares all of the subject specific variables to be used during
%the model calculations as global variables, so you may edit the values
%here without risk of altering the actual model file.

%All variables are being declared global so they may be used by other
%m-files associated with the model.
global Marker_Diam Subj_Age Subj_Height Subj_Weight
global Lls2e Lscircum LMaxhc Lecircum Ldiam Rls2e Rscircum RMaxhc Recircum
global Lle2w Rle2w LMaxfc RMaxfc Lwcircum Rwcircum Rdiam
global Llwp3 Rlwp3 Lmpcircum Rmpcircum Lhwidth Rhwidth
global SWSide SWDirection Vsamplerate SWsamplerate FShift StaticViconFP
global StartFrame EndFrame ViconFilename ViconSheetname FileOutName
global ViconFilePath SWFilename SWSheetname SDir AvgTrialFileName

%Enter data file information and the start and end frame of the vicon
%kinematic data as determined during labeling and editing marker
%trajectories.
ViconFilename = 'ENTER FILENAME';
ViconSheetname = 'ENTER FILENAME';
ViconFilePath = 'C:/Users/Alyssa/Documents/MATLAB/...ENTER PATH.c3d';
StaticViconFP = 'C:/Users/Alyssa/Documents/MATLAB/... ENTER PATH.c3d';
StartFrame = 1550;
EndFrame = 1940;

%the entire SW filename is too many characters for the sheet name, it cuts
%off after 31 characters. Only enter the first 31 characters of the
%SWFilename for the sheetname (unless you renamed the SW file), OR double
%check the sheetname by opening the SW file.
SWFilename = 'C:/Users/Alyssa/Documents/MATLAB/... ENTER PATH';
SWSheetname = ENTER SHEETNAME ';
AvgTrialFileName = 'C:/Users/Alyssa/Documents/MATLAB/... ENTER PATH';

%Provide a name for the Output file containing all angular, force and
%moment data
FileOutName = 'C:/Users/Alyssa/Documents/MATLAB/... ENTER PATH';

%Please enter what side of the Wheelchair the smartwheel is on:
%Enter 1 for Right side
%Enter 2 for Left Side
SWSide = 1;

%Plese enter which direction the Wheelchair was traveling in the lab
%Enter 1 if travel was in positive (+) Global X direction
%Enter 2 if travel was in negative (-) Global X direction
SWDirection = 1;

%SmartWheel Information
SWsamplerate = 240; %SmartWheel software sampling rate (Hz)
Vsamplerate = 120; %Vicon software sampling frequency (Hz)

FShift = 0; %Frame # difference between kinetic and kinematic

```

```

    %This value is zero if the Vicon data and SW data are synchronized
    %If FShift is something other than zero please enter the following:
    SDir = 'Forward'; %the direction the SW frames need to be shifted
        %If the SW frames are behind the Vicon frames enter 'Forward'.
        %If the SW frames are ahead the Vicon frames, enter 'Backward'.

%%%%%%%%%%%%%%%%%%%%%%%%%%%%%%%%%%%%%%%%%%%%%%%%%%%%%%%%%%%%%%%%%%%%%%%%%%%%%%
%                               Subject Specific Measurements and Data                               %
%%%%%%%%%%%%%%%%%%%%%%%%%%%%%%%%%%%%%%%%%%%%%%%%%%%%%%%%%%%%%%%%%%%%%%%%%%%%%%

%Marker diameter is in mm, age in years, height in meters, weight in pounds
%(will convert to newtons);
Marker_Diam = 14;
Subj_Age = 17;
Subj_Heightinches = 71.5;
Subj_Height = Subj_Heightinches*0.0254;
Subj_Weightlbs = 145;
Subj_Weight = Subj_Weightlbs*4.44822;

%For all of the following: L = Left Side and R = Right Side
%All measurements should be in METERS (NOT CM OR MM)

%Humerus Measurements
%Length from the shoulder joint center to the elbow joint center
Lls2e = 0.320;
Rls2e = 0.320;
%Shoulder circumference
Lscircum = 0.380;
Rscircum = 0.380;
%Maximum humerus circumference
LMaxhc = 0.250;
RMaxhc = 0.250;
%Elbow circumference
Lecircum = 0.240;
Recircum = 0.240;
%Elbow diameter
Lediam = 0.070;
Rediam = 0.070;

%Forearm Measurements
%Length from the elbow joint center to the wrist joint center
Lle2w = 0.280;
Rle2w = 0.290;
%Maximum forearm circumference
LMaxfc = 0.245;
RMaxfc = 0.245;
%Wrist circumference
Lwcircum = 0.170;
Rwcircum = 0.170;

%Hand Measurements
%Length from the wrist joint to the tip of third phalange
Llwp3 = 0.205;
Rlwp3 = 0.190;
%Metacarpal-phalangeal joint circumference - perimeter around.
Lmpcircum = 0.205;
Rmpcircum = 0.205;
%Hand width (or thickness)
Lhwidth = 0.025;
Rhwidth = 0.025;

%%%%%% You are done editing the parameter file! %%%%%%%%%%%%%%%
fprintf('Parameter file complete.  Now run Biomechanic Model\n');

```

A.3.2 Biomechanical Model

```
%Pediatric UE Wheelchair Model
test = c3dserver();

%Opens the c3d file in order to read in the kinematic data
%First argument: test is the name I gave to the c3d server when downloaded,
%Second argument: a number, any number other than one allows for the file
%name and path to be entered as a third argument
%Third argument: the path to the vicon file, ending with vicon filename
openc3d(test,3,ViconFilePath);

%Extra information obtained from the c3d file
framesum = nframes(test); %obtains total number of frames
vidfRate = GetVideoFrameRate(test); %obtains video frame rate in fps
vidfRatio = GetAnalogVideoRatio(test); %obtains ratio of video frame rate to
analog sampling frequency
analogRate = vidfRate*vidfRatio; %Analog data sampling frequency
numAnalog = GetAnalogChannels(test); %Obtain number of analog channels that
were used
analogIndexhuh = GetParameterIndex(test,'ANALOG','LABELS');
analogLengthhuh = GetParameterLength(test,analogIndexhuh);
nummarkersused = GetNumber3DPoints(test); %The number of markers for which
data was collected
NumInterpGapMax = GetMaxInterpolationGap(test); %Maximum gap over which
interpolation was used to fill

%Read in marker position data using 'get3dtarget' function
%First argument: call c3d server
%Second argument: the marker name as string
%Third argument: 0 means read in xyz position data as matrix,
%1 means xyz data and the residual,
%Optional 4th/5th arguments: Can enter desired start and end frames of data
%no numbers here and all data in the channel is obtained
SPC7 = get3dtarget(test,'SPC7',0,StartFrame,EndFrame);
STRN = get3dtarget(test,'STRN',0,StartFrame,EndFrame);
IJM = get3dtarget(test,'IJ',0,StartFrame,EndFrame);
RAA = get3dtarget(test,'RAA',0,StartFrame,EndFrame);
LAA = get3dtarget(test,'LAA',0,StartFrame,EndFrame);
RCP = get3dtarget(test,'RCP',0,StartFrame,EndFrame);
LCP = get3dtarget(test,'LCP',0,StartFrame,EndFrame);
RSS = get3dtarget(test,'RSS',0,StartFrame,EndFrame);
LSS = get3dtarget(test,'LSS',0,StartFrame,EndFrame);
RACR = get3dtarget(test,'RACR',0,StartFrame,EndFrame);
LACR = get3dtarget(test,'LACR',0,StartFrame,EndFrame);
RHUM = get3dtarget(test,'RHUM',0,StartFrame,EndFrame);
LHUM = get3dtarget(test,'LHUM',0,StartFrame,EndFrame);
ROLC = get3dtarget(test,'ROLC',0,StartFrame,EndFrame);
LOLC = get3dtarget(test,'LOLC',0,StartFrame,EndFrame);
RULN = get3dtarget(test,'RULN',0,StartFrame,EndFrame);
LULN = get3dtarget(test,'LULN',0,StartFrame,EndFrame);
RRAD = get3dtarget(test,'RRAD',0,StartFrame,EndFrame);
LRAD = get3dtarget(test,'LRAD',0,StartFrame,EndFrame);
RM3 = get3dtarget(test,'RM3',0,StartFrame,EndFrame);
LM3 = get3dtarget(test,'LM3',0,StartFrame,EndFrame);
RM5 = get3dtarget(test,'RM5',0,StartFrame,EndFrame);
LM5 = get3dtarget(test,'LM5',0,StartFrame,EndFrame);
RTOPC = get3dtarget(test,'RTOPC',0,StartFrame,EndFrame);
LTOPC = get3dtarget(test,'LTOPC',0,StartFrame,EndFrame);
RBOTC = get3dtarget(test,'RBOTC',0,StartFrame,EndFrame);
LBOTC = get3dtarget(test,'LBOTC',0,StartFrame,EndFrame);
WHEEL = get3dtarget(test,'WHEEL',0,StartFrame,EndFrame);
```

```

%The following incorporates Senk's method in order to determine the
%positions of the TS and AI markers during the dynamic trial.
[RTS,LTS,RAI,LAI,ThoraxAngS] =
ScapKinematicsCheck(SWDirection,StartFrame,EndFrame,ViconFilePath,StaticViconFP
);

```

```

%This section fixes global coordinate system mismatches
%UWM global and Shriners global do not match.
%Shriners: global X-axis is same, pointing anteriorly.
%Shriners: global y-axis points left, negate to equal UWM global z-axis,
%pointing right.
%Shriners: global z-axis points superior, which equals UWM global y-axis.
tempSPC7= SPC7(:,2); SPC7(:,2)= SPC7(:,3); SPC7(:,3)= -tempSPC7;
tempSTRN= STRN(:,2); STRN(:,2)= STRN(:,3); STRN(:,3)= -tempSTRN;
tempIJM= IJM(:,2); IJM(:,2)= IJM(:,3); IJM(:,3)= -tempIJM;
tempRSS= RSS(:,2); RSS(:,2)= RSS(:,3); RSS(:,3)= -tempRSS;
tempLSS= LSS(:,2); LSS(:,2)= LSS(:,3); LSS(:,3)= -tempLSS;
tempRAA= RAA(:,2); RAA(:,2)= RAA(:,3); RAA(:,3)= -tempRAA;
tempLAA= LAA(:,2); LAA(:,2)= LAA(:,3); LAA(:,3)= -tempLAA;

```

CONTINUED FOR ALL MARKERS

```

%X and Z directions will be flipped when traveling in reverse direction
if SWDirection == 1
elseif SWDirection == 2
%Flip marker x and z coordinates of marker positions.
SPC7(:,1) = -1*SPC7(:,1); SPC7(:,3) = -1*SPC7(:,3);
STRN(:,1) = -1*STRN(:,1); STRN(:,3) = -1*STRN(:,3);
IJM(:,1) = -1*IJM(:,1); IJM(:,3) = -1*IJM(:,3);
RSS(:,1) = -1*RSS(:,1); RSS(:,3) = -1*RSS(:,3);
LSS(:,1) = -1*LSS(:,1); LSS(:,3) = -1*LSS(:,3);
RTS(:,1) = -1*RTS(:,1); RTS(:,3) = -1*RTS(:,3);
LTS(:,1) = -1*LTS(:,1); LTS(:,3) = -1*LTS(:,3);

```

CONTINUED FOR ALL MARKERS

```
end
```

```

%Read in Kinetic Data collected from SmartWheel
%Columns A and B sample numbers
%Columns C and D, unconverted and converted angular position
%Column E 1/20 second running average velocity [deg/s]
%Column F - unused
%Columns G-L, raw data (fxyz and mxyz)
%Columns M-R, filtered data (fxyz and mxyz)
%Forces and Moments already filtered, F in N and Moments in Nm
[SWFx]=xlsread(SWFilename,SWSheetname,'S:S');
[SWFy]=xlsread(SWFilename,SWSheetname,'T:T');
[SWFz]=xlsread(SWFilename,SWSheetname,'U:U');
[SWF] = [SWFx,SWFy,SWFz];
[SWMx]=xlsread(SWFilename,SWSheetname,'V:V');
[SWMy]=xlsread(SWFilename,SWSheetname,'W:W');
[SWMz]=xlsread(SWFilename,SWSheetname,'X:X');
[SWM] = [SWMx,SWMy,SWMz];
[Frame] = xlsread(SWFilename,SWSheetname,'A:A');
[SWAng]=xlsread(SWFilename,SWSheetname,'D:D');
DataLength = length(SWFx);
%Corrected SW forces and moments to align with global.
if SWSide == 1
SWM(:,3) = -1*SWM(:,3); %Corrected b/c SW +Mz definition is opposite.
elseif SWSide == 2
SWM(:,1) = -1*SWM(:,1);
SWM(:,3) = -1*SWM(:,3);
end

```

```

%This section is used if synchronization between SW and Vicon is incorrect.
if FShift>0;
    if strcmp (SDir,'Forward')
        Addon = zeros(FShift,3);
        SWF = cat(1,Addon,SWF);
        SWM = cat(1,Addon,SWM);
        FrameNum = zeros(DataLength+FShift,1);
        for i=1:DataLength+FShift
            FrameNum(i) = i;
        end
    elseif strcmp (SDir,'Backward')
        for i=1:FShift
            SWF(1,:) = [];
            SWM(1,:) = [];
        end
        FrameNum = zeros(DataLength-FShift,1);
        for i=1:DataLength-FShift
            FrameNum(i)=i;
        end
    end
elseif FShift == 0;
    FrameNum = zeros(DataLength,1);
    for i=1:DataLength
        FrameNum(i) = i;
    end
end

%The following downsamples the SW data to match that of the kinematic data.
%Convert Sample Number to Time
FrameNum = FrameNum';
TimePt = FrameNum*(1/SWsamplerate);
%Create a time series containing the SW data and the corresponding time
%array
SWFseries = timeseries(SWF,TimePt);
SWMseries = timeseries(SWM,TimePt);
%Create a new time array to be the desired time the SW data will
%correspond to, based upon the sampling rate of the kinematic data
TrialLength = DataLength/SWsamplerate; %total time of SW data collection in
seconds
VTimeInc = 1/Vsamplerate; %time increments of the vicon sampling rate
t = (0:VTimeInc:TrialLength)'; %new time array
FNumNew = t*(Vsamplerate); %new frame number array
%Now can downsample the SW data according to the Vicon sampling rate
SWFnew = resample(SWFseries,t);
SWMnew = resample(SWMseries,t);
SWFnew = [SWFnew.data(:,1),SWFnew.data(:,2),SWFnew.data(:,3)];
SWMnew = [SWMnew.data(:,1),SWMnew.data(:,2),SWMnew.data(:,3)];
SWFfinal = SWFnew;
SWMfinal = SWMnew;

%Since only a certain range of Vicon data frames was read into the model
%(from startframe to endframe), the SW data contains a different number of
%data points than the Vicon data. The array lengths need to match in order
%for MatLab to perform mathematical functions.

%First, remove the extra data at the end of the SW arrays after the desired
%endframe
arraylengthdiff = length(SWFnew)-EndFrame-1;
blah = length(SWFnew)+1;
for i=1:arraylengthdiff
    SWFfinal(blah-i,:)=[];
    SWMfinal(blah-i,:)=[];
    FNumNew(blah-i,:)=[];
end

```

```

        t(blah-i,:)=[];
    end
    SWFreal = SWFfinal;
    SWMreal = SWMfinal;

%Now delete unnecessary SW data at beginning of trial, prior to the
%startframe of interest
for i=1:StartFrame
    SWFreal(1,:)=[];
    SWMreal(1,:)=[];
    FNumNew(1,:) = [];
    t(1,:) = [];
end

%NOTE:If wheelchair travels on flat ground, the SW coordinate system aligns
with
%global coordinate system. If the wheelchair is traveling on an incline the
%SW coordinate system is rotated about global Z-axis by the degree of incline.

%To improve Matlab performance and memory use, preallocate arrays that
%change size on each pass through a loop.
rows = length(RTOPC);
Incline = zeros(rows,1);
WCAnglesE = zeros(rows,3);
WC_Origin = (RBOTC+LBOTC)/2;
[WC_Xaxis,WC_Yaxis,WC_Zaxis] = Create_Wheelchair_Axes(RBOTC,LBOTC,LTOPC,RTOPC);
for i=1:rows
    Wheelchair_axes = [WC_Xaxis(i,:);WC_Yaxis(i,:);WC_Zaxis(i,:)];
    WC_axes = transpose(Wheelchair_axes);
    WCAnglesE(i,:) = Determine_Euler_Angles(Global_Axes,WC_axes,'ZXYsf');
end

%%%%%%%%%%%%%%%%%%%%%%%%%%%%%%%%%%%%%%%%%%%%%%%%%%%%%%%%%%%%%%%%%%%%%%%%%%%%%%
%                               KINEMATIC PORTION                               %
%%%%%%%%%%%%%%%%%%%%%%%%%%%%%%%%%%%%%%%%%%%%%%%%%%%%%%%%%%%%%%%%%%%%%%%%%%%%%%
%Calculate subject parameters using global inputs from the parameter file:
%parameters_EDIT.m

%Calculation of segment mass, from Jensen 1989; In N b/c Subj_Weight in N.
MUa = (0.00069558*Subj_Age + 0.02344)*Subj_Weight;
MFa = (0.00031268*Subj_Age + 0.01340)*Subj_Weight;
MHand = (0.00880)*Subj_Weight;

%Calculation of perimeters for Inertia calculations, from Yeadon and Morlock
1989
LPHum = (Lscircum+2*LMaxhc+Lecircum)/4;      %Humerus Perimeter
RPHum = (Rscircum+2*RMaxhc+Recircum)/4;      %Humerus Perimeter
LPFarm = (Lecircum+2*LMaxfc+Lwcircum)/4;      %Forearm Perimeter
RPFarm = (Recircum+2*RMaxfc+Rwcircum)/4;      %Forearm Perimeter
LPHand = (Lwcircum+Lmpcircum)/2;              %Hand Perimeter
RPHand = (Rwcircum+Rmpcircum)/2;              %Hand Perimeter

%Calculation of segmental moments of inertia (kg*m^2), from Yeadon & Morlock
'89
%Yeadon and Morlock coordinate system has X-axis in A/P direction, Y-axis
%in the lateral direction and the Z-axis vertical. Therefore, their Iz
%formula corresponds to our Iy, and their Iy equation equals Ix and Iz.
%Humerus
LHumIyk = 0.979*LPHum*LPHum*LPHum*LPHum*Lls2e;
LHumIyk = 0.5*LHumIyk+6.11*LPHum*LPHum*Lls2e*Lls2e*Lls2e;
LHumIy = LHumIyk*9.81; LHumIx = LHumIyk*9.81; %Convert to N*m2
LHumIz = LHumIx;
RHumIyk = 0.979*RPHum*RPHum*RPHum*RPHum*Rls2e;

```

```

RHumIxx = 0.5*RHumIyk+6.11*RPHum*RPHum*Rls2e*Rls2e*Rls2e;
RHumIy = RHumIyk*9.81; RHumIx = RHumIxx*9.81; %Convert to N*m2
RHumIz = RHumIx;

```

SIMILAR FOR FOREARM AND HAND

```

%Set-up segment coordinate systems
%Thorax and Clavicles, done simulataneously
T_Origin = (IJM+SPC7)/2;
ThoraxAng = zeros(rows,3); %Preallocating the matrix improves performance
[Tt_X,Tt_Y,Tt_Z] = Create_ThoraxTemp_Axes(STRN,IJM,SPC7);
C_Origin = IJM;
TPtemp = T_Origin+10*Tt_Z;
[T_X,T_Y,T_Z] = Create_Thorax_Axes(IJM,SPC7,TPtemp,T_Origin);

LClavAng = zeros(rows,3); %Preallocating the matrix improves performance
RClavAng = zeros(rows,3);
LC_X = zeros(rows,3); LC_Y = zeros(rows,3); LC_Z = zeros(rows,3);
RC_X = zeros(rows,3); RC_Y = zeros(rows,3); RC_Z = zeros(rows,3);

%Scapulae
RS_Origin = RAA;
LS_Origin = LAA;
RScapAng = zeros(rows,3); %Preallocating the matrix improves performance
RScaptoTAng = zeros(rows,3);
LScapAng = zeros(rows,3);
LScaptoTAng = zeros(rows,3);
[RS_X,RS_Y,RS_Z] = Create_Scapula_Axes(RAA,RTS,RAI,LAA,LTS,LAI,'Right');
[LS_X,LS_Y,LS_Z] = Create_Scapula_Axes(RAA,RTS,RAI,LAA,LTS,LAI,'Left');

for i=1:rows
    Thorax_Axes = [T_X(i,:);T_Y(i,:);T_Z(i,:)];
    T_Axes = transpose(Thorax_Axes);
    ThoraxAng(i,:) =
    Determine_Euler_Angles_RadAtan2(Global_Axes,T_Axes,'ZXYsf');

    [RC_X(i,:),RC_Y(i,:),RC_Z(i,:)] =
    Create_Clavicle_Axes(IJM(i,:),RACR(i,:),LACR(i,:),T_Y(i,:),'Right');
    RClav_Axes = [RC_X(i,:);RC_Y(i,:);RC_Z(i,:)];
    RC_Axes = transpose(RClav_Axes);
    RClavAng(i,:) = Determine_Euler_Angles_RadAtan2(T_Axes,RC_Axes,'ZXYsf');
    RScap_Axes = [RS_X(i,:);RS_Y(i,:);RS_Z(i,:)];
    RS_Axes = transpose(RScap_Axes);
    RScapAng(i,:) = Determine_Euler_Angles_RadAtan2(RC_Axes,RS_Axes,'ZXYsf');
    RScaptoTAng(i,:) = Determine_Euler_Angles_RadAtan2(T_Axes,RS_Axes,'ZXYsf');
end

SIMILAR FOR LEFT SIDE
end

```

```

%UpperArms
[RUAt_X,RUAt_Y,RUAt_Z] =
Create_TempUpperArm_Axes(ROLC,SPC7,RHUM,LOLC,LHUM,'Right');
[LUAt_X,LUAt_Y,LUAt_Z] =
Create_TempUpperArm_Axes(ROLC,SPC7,RHUM,LOLC,LHUM,'Left');

%Need to determine the elbow joint centers in order to obtain the upperarm
%axes.
REOffset = (Rediam*(1000)+Marker_Diam)/2;
LEOffset = (Lediam*(1000)+Marker_Diam)/2;
REJC = ROLC+REOffset.*RUAt_X;
LEJC = LOLC+LEOffset.*LUAt_X;

%Determination of scapular axes as used by Meskers for use with Meskers
%regression equations for location of GH joint.

```

```

[RSGH_X,RSGH_Y,RSGH_Z] = Create_ScapGH_Axes(RAA,RTS,RAI,LAA,LTS,LAI,'Right');
[LSGH_X,LSGH_Y,LSGH_Z] = Create_ScapGH_Axes(RAA,RTS,RAI,LAA,LTS,LAI,'Left');
%Must translate and rotate marker positions from the global coordinate
%system to the local scapular system just created so may apply equations.
RACGH = zeros(rows,3); RCPGH = zeros(rows,3); RTSGH = zeros(rows,3);
LACGH = zeros(rows,3); LCPGH = zeros(rows,3); LTSGH = zeros(rows,3);
for i=1:rows
    RScapGH_Axes = [RSGH_X(i,:);RSGH_Y(i,:);RSGH_Z(i,:)];
    RSGH_Axes = transpose(RScapGH_Axes);
    RACGH(i,:) = RScapGH_Axes*transpose((RACR(i,:)-RAA(i,:)));
    RCPGH(i,:) = RScapGH_Axes*transpose((RCP(i,:)-RAA(i,:)));
    RTSGH(i,:) = RScapGH_Axes*transpose((RTS(i,:)-RAA(i,:)));
    SIMILAR FOR LEFT SIDE
end
%Now the location of the glenohumeral joint center may be determined using
%the regression equations derived through sphere fitting techniques by
%Meskers et al. These equations use locations of five scapular markers.
RCP2RAIlength = sqrt((RAI(:,1)-RCP(:,1)).^2+(RAI(:,2)-RCP(:,2)).^2+(RAI(:,3)-
RCP(:,3)).^2);
RCP2RAAlength = sqrt((RCP(:,1)-RAA(:,1)).^2+(RCP(:,2)-RAA(:,2)).^2+(RCP(:,3)-
RAA(:,3)).^2);
SIMILAR FOR LEFT SIDE

%The ISG revised version of Meskers shoulder joint center location equations
RSJCx = 26.896+0.614*RTSGH(:,1)+0.295*(RCP2RAIlength);
RSJCy = -16.307+0.825*RACGH(:,2)+0.293*RCPGH(:,3);
RSJCz = -1.740-0.899*(RCP2RAAlength)-0.229*RTSGH(:,1);
SIMILAR FOR LEFT SIDE

%Lastly, the location of the glenohumeral joint centers need to be
%translated and rotated back into the global coordinate system for use in
%the remainder of the model.
RSJC = zeros(rows,3); LSJC = zeros(rows,3);
for i=1:rows
    RSGHJC = [RSJCx(i);RSJCy(i);RSJCz(i)];
    RScapGH_Axes = [RSGH_X(i,:);RSGH_Y(i,:);RSGH_Z(i,:)];
    RSJC(i,:) = RSGH_Axes*RSGHJC+transpose(RAA(i,:));
    SIMILAR FOR LEFT SIDE
end

RUA_Origin = RSJC; LUA_Origin = LSJC;
[RUArm_X,RUArm_Y,RUArm_Z] =
Create_UpperArm_Axes(RSJC,REJC,RULN,LSJC,LEJC,LULN,'Right');
[LUArm_X,LUArm_Y,LUArm_Z] =
Create_UpperArm_Axes(LSJC,REJC,RULN,LSJC,LEJC,LULN,'Left');

RGHAng = zeros(rows,3); %Preallocating the matrix improves performance
LGHAng = zeros(rows,3);
RGHtoTAng = zeros(rows,3); LGHtoTAng = zeros(rows,3);
for i=1:rows
    Thorax_Axes = [T_X(i,:);T_Y(i,:);T_Z(i,:)];
    T_Axes = transpose(Thorax_Axes);

    RScap_Axes = [RS_X(i,:);RS_Y(i,:);RS_Z(i,:)];
    RS_Axes = transpose(RScap_Axes);
    RUArm_Axes = [RUArm_X(i,:);RUArm_Y(i,:);RUArm_Z(i,:)];
    RUA_Axes = transpose(RUArm_Axes);
    RGHAng(i,:) = Determine_Euler_Angles_RadAtan2(RS_Axes,RUA_Axes,'ZXYsf');
    RGHtoTAng(i,:) = Determine_Euler_Angles_RadAtan2(T_Axes,RUA_Axes,'ZXYsf');
    SIMILAR FOR LEFT SIDE
end

```



```

%Upper Arm segment center of gravity calculations, from Jensen 1989
RHumCG = RSJC-0.4418*(RSJC-REJC);
LHumCG = LSJC-0.4418*(LSJC-LEJC);

%Forearms
RFA_Origin = RULN; LFA_Origin = LULN;
RElbAng = zeros(rows,3); %Preallocating the matrix improves performance
LElbAng = zeros(rows,3);
[RFA_X,RFA_Y,RFA_Z] =
Create_Forearm_Axes(RULN,RRAD,REJC,LULN,LRAD,LEJC,'Right');
[LFA_X,LFA_Y,LFA_Z] =
Create_Forearm_Axes(RULN,RRAD,REJC,LULN,LRAD,LEJC,'Left');

for i=1:rows
    RUArm_Axes = [RUArm_X(i,:);RUArm_Y(i,:);RUArm_Z(i,:)];
    RUA_Axes = transpose(RUArm_Axes);
    RForearm_Axes = [RFA_X(i,:);RFA_Y(i,:);(RFA_Z(i,:))];
    RFA_Axes = transpose(RForearm_Axes);
    RElbAng(i,:) = Determine_Euler_Angles_RadAtan2(RUA_Axes,RFA_Axes,'ZXYsf');

```

SIMILAR FOR LEFT SIDE

```

end

%Need to determine the wrist joint center
RWJC = (RULN+RRAD)./2;
LWJC = (LULN+LRAD)./2;
%Forearm segment center of gravity calculations, from Jensen 1989
RFaCG = REJC-((0.43223-0.00092718*Subj_Age).*(REJC-RWJC));
LFaCG = LEJC-((0.43223-0.00092718*Subj_Age).*(LEJC-LWJC));

%Hands
%Need to determine the Third Metacarpal joint centers
[RHT_X,RHT_Y,RHT_Z] =
Create_HandTemp_Axes(RULN,RRAD,RM5,LULN,LRAD,LM5,'Right');
[LHT_X,LHT_Y,LHT_Z] = Create_HandTemp_Axes(RULN,RRAD,RM5,LULN,LRAD,LM5,'Left');
RM3JC = RM3 + ((Rhwidth+Marker_Diam)/2).*RHT_X;
LM3JC = LM3 + ((Lhwidth+Marker_Diam)/2).*LHT_X;
RH_Origin = RM3JC; LH_Origin = LM3JC;
[RH_X,RH_Y,RH_Z] =
Create_Hand_Axes(RM3JC,RWJC,RULN,RRAD,LM3JC,LWJC,LULN,LRAD,'Right');
[LH_X,LH_Y,LH_Z] =
Create_Hand_Axes(RM3JC,RWJC,RULN,RRAD,LM3JC,LWJC,LULN,LRAD,'Left');

RWrAng = zeros(rows,3); %Preallocating the matrix improves performance
LWrAng = zeros(rows,3);
for i=1:rows
    RForearm_Axes = [RFA_X(i,:);RFA_Y(i,:);(RFA_Z(i,:))];
    RFA_Axes = transpose(RForearm_Axes);
    RHand_Axes = [RH_X(i,:);RH_Y(i,:);(RH_Z(i,:))];
    RH_Axes = transpose(RHand_Axes);
    RWrAng(i,:) = Determine_Euler_Angles_RadAtan2(RFA_Axes,RH_Axes,'ZXYsf');

```

SIMILAR FOR LEFT SIDE

```

end

%Negate the coronal and transverse plane left side angles in order to match
%the convention of the right side (internal = +, external = -) etc.
LWrAng(:,1:2) = -1*LWrAng(:,1:2);
LElbAng(:,1:2) = -1*LElbAng(:,1:2);
LGHAng(:,1:2) = -1*LGHAng(:,1:2);
LGHtoTAng(:,1:2) = -1*LGHtoTAng(:,1:2);
LScapAng(:,1:2) = -1*LScapAng(:,1:2);

```

```

LScaptoTAng(:,1:2) = -1*LScaptoTAng(:,1:2);
LClavAng(:,1:2) = -1*LClavAng(:,1:2);

%Hand segment center of gravity calculations, from Jensen 1989
RHandCG = RWJC-0.808.*(RWJC-RM3);
LHandCG = LWJC-0.808.*(LWJC-LM3);

%Angular Velocities and Accelerations Calculations from Euler Angles
%Equations from Winters Text
ThoraxAngVel =
CalculateAngVel(ThoraxAng(:,1),ThoraxAng(:,2),ThoraxAng(:,3),VsampleRate);
ThoraxAngAcc =
CalculateAngAcc(ThoraxAng(:,1),ThoraxAng(:,2),ThoraxAng(:,3),VsampleRate);
RScapAngVel =
CalculateAngVel(RScapAng(:,1),RScapAng(:,2),RScapAng(:,3),VsampleRate);
RScapAngAcc =
CalculateAngAcc(RScapAng(:,1),RScapAng(:,2),RScapAng(:,3),VsampleRate);
LScapAngVel =
CalculateAngVel(LScapAng(:,1),LScapAng(:,2),LScapAng(:,3),VsampleRate);
LScapAngAcc =
CalculateAngAcc(LScapAng(:,1),LScapAng(:,2),LScapAng(:,3),VsampleRate);
SIMILAR FOR ALL REMAINING ANGLE DATA

%Segment center of gravity velocity and acceleration calculations
%These are not angular calculations, though they use the same function
%as the one used to calculate the angular kinematics. In mm/s and mm/sec2
%then converted to m/s and m/s^2.
RHumCGVel =
(CalculateAngVel(RHumCG(:,1),RHumCG(:,2),RHumCG(:,3),VsampleRate))./1000;
RHumCGAcc =
(CalculateAngAcc(RHumCG(:,1),RHumCG(:,2),RHumCG(:,3),VsampleRate))./1000;
LHumCGVel =
(CalculateAngVel(LHumCG(:,1),LHumCG(:,2),LHumCG(:,3),VsampleRate))./1000;
LHumCGAcc =
(CalculateAngAcc(LHumCG(:,1),LHumCG(:,2),LHumCG(:,3),VsampleRate))./1000;
SIMILAR FOR FOREARM AND HAND

%Remove the first and last velocity and acceleration data points, because =
%0 due to lack of data points at the beginning and end of array.

%Remove the end point
arrayend = length(RWrAngVel);
RWrAngVel(arrayend,:) = []; RWrAngAcc(arrayend,:) = [];
LWrAngVel(arrayend,:) = []; LWrAngAcc(arrayend,:) = [];
RHandCGVel(arrayend,:) = []; RHandCGAcc(arrayend,:) = [];
LHandCGVel(arrayend,:) = []; LHandCGAcc(arrayend,:) = [];
SIMILAR FOR REMAINING JOINTS AND SEGMENTS

%Remove the first point
RWrAngVel(1,:) = []; RWrAngAcc(1,:) = [];
LWrAngVel(1,:) = []; LWrAngAcc(1,:) = [];
RHandCGVel(1,:) = []; RHandCGAcc(1,:) = [];
LHandCGVel(1,:) = []; LHandCGAcc(1,:) = [];
SIMILAR FOR REMAINING JOINTS AND SEGMENTS

%Done removing data points for Angular velocities and accelerations and CG
%accels and velocities.

%Now remove beginning and ending data points from the angular data and the
%SW force and moment data.

```

SIMILAR TO PREVIOUS SECTION, NOW FOR ANGLE, FORCE and MOMENT DATA

%Remove the last point of the axes and joint center arrays

SIMILAR TO PREVIOUS SECTION, NOW FOR JOINT AXES and JOINT CENTER DATA

%Remove last and first points of the frame number array and time array.

FNumNew(arrayend,:) = []; t(arrayend,:) = [];

FNumNew(1,:) = []; t(1,:) = [];

rows = rows-2;

%Force Calculations

if SWSide == 1

 %Right Side

 %Hand Forces in Global C.S. (Negate the SWF values so FRHand values are

 %the reactionary forces of the SW acting on the hand.

 FRHandxG = -SWFrealF(:,1);

 FRHandyG = -SWFrealF(:,2);

 FRHandzG = -SWFrealF(:,3);

 [FRHandG] = [FRHandxG,FRHandyG,FRHandzG];

 FRHandxL = zeros(rows,1); FRHandyL = zeros(rows,1); FRHandzL =

zeros(rows,1);

 for i=1:rows

 FRHandxL(i,1) = dot(-SWFrealF(i,:),RH_X(i,:));

 FRHandyL(i,1) = dot(-SWFrealF(i,:),RH_Y(i,:));

 FRHandzL(i,1) = dot(-SWFrealF(i,:),RH_Z(i,:));

 end

 FRHandL = [FRHandxL,FRHandyL,FRHandzL];

 FRHandLNorm = (FRHandL/Subj_Weight)*100;

 %[FRHandG] = -SWF;

 [FRHandGNorm] = ((FRHandG)/Subj_Weight)*100; %Normalized to Body Weight

 %Wrist Forces (Note: for F=ma, A newton has units kg*m/(s*s)

 %Global C.S

 [FRWristx] = -1*(MHand/9.81)*RHandCGAcc(:,1)-FRHandxG;

 [FRWristy] = -1*(MHand/9.81)*RHandCGAcc(:,2)+(MHand/9.81)*9.81-

FRHandyG;

 [FRWristz] = -1*(MHand/9.81)*RHandCGAcc(:,3)-FRHandzG;

 [FRWristG]=[FRWristx,FRWristy,FRWristz];

 [FRWristGNorm] = ((FRWristG)/Subj_Weight)*100;

 %Anatomical Joint forces

 FRWristxL = zeros(rows,1); FRWristyL = zeros(rows,1); FRWristzL =

zeros(rows,1);

 for i=1:rows

 FRWristxL(i,1) = dot(FRWristG(i,:),RH_X(i,:));

 FRWristyL(i,1) = dot(FRWristG(i,:),RH_Y(i,:));

 FRWristzL(i,1) = dot(FRWristG(i,:),RH_Z(i,:));

 end

 FRWristL = [FRWristxL,FRWristyL,FRWristzL];

 FRWristLNorm = (FRWristL/Subj_Weight)*100;

 %Elbow Forces

 %Global C.S.

 [FRElbowx] = -1*(MFa/9.81)*RFaCGAcc(:,1)-(-1*FRWristx);

 [FRElbowy] = -1*(MFa/9.81)*RFaCGAcc(:,2)+(MFa/9.81)*9.81-(-1*FRWristy);

 [FRElbowz] = -1*(MFa/9.81)*RFaCGAcc(:,3)-(-1*FRWristz);

 [FRElbowG]=[FRElbowx,FRElbowy,FRElbowz];

 [FRElbowGNorm]=((FRElbowG)/Subj_Weight)*100;

 %Anatomical Joint forces

 FRElbowxL = zeros(rows,1); FRElbowyL = zeros(rows,1); FRElbowzL =

zeros(rows,1);

 for i=1:rows

 FRElbowxL(i,1) = dot(FRElbowG(i,:),RFA_X(i,:));

```

        FRELbowyL(i,1) = dot(FRELbowG(i,:),RFA_Y(i,:));
        FRELbowzL(i,1) = dot(FRELbowG(i,:),RFA_Z(i,:));
    end
    FRELbowL = [FRELbowxL,FRELbowyL,FRELbowzL];
    FRELbowLNorm = (FRELbowL/Subj_Weight)*100;
    %Glenohumeral Forces
    %Global C.S.
    [FRGlenoHumx] = -1*(MUa/9.81)*RHumCGAcc(:,1)-(-1*FRELbowx);
    [FRGlenoHumy] = -1*(MUa/9.81)*RHumCGAcc(:,2)+(MUa/9.81)*9.81-(-
1*FRELbowy);
    [FRGlenoHumz] = -1*(MUa/9.81)*RHumCGAcc(:,3)-(-1*FRELbowz);
    [FRGlenoHumG]=[FRGlenoHumx,FRGlenoHumy,FRGlenoHumz];
    [FRGlenoHumGNorm]=(FRGlenoHumG)/Subj_Weight)*100;
    %Anatomical Joint forces
    FRGlenoHumxL = zeros(rows,1); FRGlenoHumyL = zeros(rows,1);
    FRGlenoHumzL = zeros(rows,1);
    for i=1:rows
        FRGlenoHumxL(i,1) = dot(FRGlenoHumG(i,:),RH_X(i,:));
        FRGlenoHumyL(i,1) = dot(FRGlenoHumG(i,:),RH_Y(i,:));
        FRGlenoHumzL(i,1) = dot(FRGlenoHumG(i,:),RH_Z(i,:));
    end
    FRGlenoHumL = [FRGlenoHumxL,FRGlenoHumyL,FRGlenoHumzL];
    FRGlenoHumLNorm = (FRGlenoHumL/Subj_Weight)*100;

elseif SWSide == 2
    %Left Side
    SIMILAR TO RIGHT SIDE
end

%Rate of Change of Angular Momentum Calculations, for Moment Calculations
if SWSide ==1
    %Right
    %Hand dH/dt
    [HRHandx] = RHandIx.*RWrAngAcc(:,1)-(RHandIy-
RHandIz).*RWrAngVel(:,2).*RWrAngVel(:,3);
    [HRHandy] = RHandIy.*RWrAngAcc(:,2)-(RHandIz-
RHandIx).*RWrAngVel(:,3).*RWrAngVel(:,1);
    [HRHandz] = RHandIz.*RWrAngAcc(:,3)-(RHandIx-
RHandIy).*RWrAngVel(:,1).*RWrAngVel(:,2);
    [HRHand]=[HRHandx,HRHandy,HRHandz];
    %Forearm dH/dt
    [HRFax] = RFaIx*RElbAngAcc(:,1)-(RFaIy-
RFaIz)*RElbAngVel(:,2).*RElbAngVel(:,3);
    [HRFay] = RFaIy*RElbAngAcc(:,2)-(RFaIz-
RFaIx)*RElbAngVel(:,3).*RElbAngVel(:,1);
    [HRFaz] = RFaIz*RElbAngAcc(:,3)-(RFaIx-
RFaIy)*RElbAngVel(:,1).*RElbAngVel(:,2);
    [HRFa]=[HRFax,HRFay,HRFaz];
    %Humerus dH/dt relative to Scapula coordinate system
    [HRHumx] = RHumIx*RGHAngAcc(:,1)-(RHumIy-
RHumIz)*RGHAngVel(:,2).*RGHAngVel(:,3);
    [HRHumy] = RHumIy*RGHAngAcc(:,2)-(RHumIz-
RHumIx)*RGHAngVel(:,3).*RGHAngVel(:,1);
    [HRHumz] = RHumIz*RGHAngAcc(:,3)-(RHumIx-
RHumIy)*RGHAngVel(:,1).*RGHAngVel(:,2);
    [HRHum]=[HRHumx,HRHumy,HRHumz];
    %Humerus dH/dt relative to thorax coordinate system
    [HRHumtoTx] = RHumIx*RGHtoTAngAcc(:,1)-(RHumIy-
RHumIz)*RGHtoTAngVel(:,2).*RGHtoTAngVel(:,3);
    [HRHumtoTy] = RHumIy*RGHtoTAngAcc(:,2)-(RHumIz-
RHumIx)*RGHtoTAngVel(:,3).*RGHtoTAngVel(:,1);
    [HRHumtoTz] = RHumIz*RGHtoTAngAcc(:,3)-(RHumIx-
RHumIy)*RGHtoTAngVel(:,1).*RGHtoTAngVel(:,2);

```

```

[HRHumtoT]= [HRHumtoTx,HRHumtoTy,HRHumtoTz];
elseif SWSide==2
    %Left
    SIMILAR TO RIGHT SIDE
end

%Moment Calculations
if SWSide == 1
    %Hand Moments (negate SWM output to get reactionary moment acting on hand)
    RHandMx = -1*SWMrealf(:,1);
    RHandMy = -1*SWMrealf(:,2);
    RHandMz = -1*SWMrealf(:,3);
    [RHandMG] = [RHandMx,RHandMy,RHandMz];
    %Wrist Moment Calculations
    %Wrist Moment Arms, converted from mm to meters.
    MaRWProx = (RWJC-RHandCG)/1000;
    MaRWDis = (RM3-RHandCG)/1000;
    %Wrist Residual Moment
    MRWrCGProx = cross(MaRWProx,FRWristG);
    MRWrCGDis = cross(MaRWDis,FRWristG);
    ResMRWristG = -1*RHandMG-MRWrCGDis-MRWrCGProx;
    %Translate to Local C.S. so can sum the hand rate of change of angular
    %momentum and the residual moment.
    ResMRWristXL = zeros(rows,1); ResMRWristYL = zeros(rows,1); ResMRWristZL =
zeros(rows,1);
    for i=1:rows
        ResMRWristXL(i,:) = dot(transpose(ResMRWristG(i,:)),RH_X(i,:));
        ResMRWristYL(i,:) = dot(transpose(ResMRWristG(i,:)),RH_Y(i,:));
        ResMRWristZL(i,:) = dot(transpose(ResMRWristG(i,:)),RH_Z(i,:));
    end
    ResMRWristL = [ResMRWristXL,ResMRWristYL,ResMRWristZL];
    %Wrist Moments in Local, hand coordinate system
    MRWristL = HRHand+ResMRWristL;
    MRWristLNorm = (MRWristL/(Subj_Weight*Subj_Height))*100;
    %Translate back to Global coordinate system and normalize
    MRWristG = zeros(rows,3);
    for i=1:rows
        RHand_Axes = [RH_X(i,:);RH_Y(i,:);RH_Z(i,:)];
        MRWristG(i,:) = MRWristL(i,:)*RHand_Axes;
    end
    MRWristGNorm = (MRWristG/(Subj_Weight*Subj_Height))*100;
    %Elbow Moment Calculations
    %Elbow Moment Arms
    MaREProx = (REJC-RFaCG)/1000;
    MaREDis = (RWJC-RFaCG)/1000;
    %Elbow Residual Moment
    MRElbCGProx = cross(MaREProx,FRElbowG);
    MRElbCGDis = cross(MaREDis,-1*FRWristG);
    ResMRElbowG = -(-1*MRWristG)-MRElbCGDis-MRElbCGProx;
    %Translate to Local C.S. in order to sum momentum/dt and moment
    ResMRElbowXL = zeros(rows,1); ResMRElbowYL = zeros(rows,1); ResMRElbowZL =
zeros(rows,1);
    for i=1:rows
        ResMRElbowXL(i,:) = dot(transpose(ResMRElbowG(i,:)),RFA_X(i,:));
        ResMRElbowYL(i,:) = dot(transpose(ResMRElbowG(i,:)),RFA_Y(i,:));
        ResMRElbowZL(i,:) = dot(transpose(ResMRElbowG(i,:)),RFA_Z(i,:));
    end
    ResMRElbowL = [ResMRElbowXL,ResMRElbowYL,ResMRElbowZL];
    %Elbow Moments
    MRElbowL = HRFa+ResMRElbowL;
    MRElbowLNorm = (MRElbowL/(Subj_Weight*Subj_Height))*100;
    %Translate back to Global coordinate system and normalize
    MRElbowG = zeros(rows,3);

```

```

for i=1:rows
    RForearm_Axes = [RFA_X(i,:);RFA_Y(i,:);(RFA_Z(i,:))];
    MRElbowG(i,:) = MRElbowL(i,:)*RForearm_Axes;
end
MRElbowGNorm = (MRElbowG/(Subj_Weight*Subj_Height))*100;
%GlenoHumeral Moment Calculations
%GlenoHumeral Moment Arms
    MaRGHProx = (RSJC-RHumCG)/1000;
    MaRGHDis = (REJC-RHumCG)/1000;
%GlenoHumeral Residual Moment
    MRGHCGProx = cross(MaRGHProx,FRGlenoHumG);
    MRGHCGDis = cross(MaRGHDis,-1*MRElbowG);
    ResMRGlenoHumG = -(-1*MRElbowG)-MRGHCGDis-MRGHCGProx;
%Translate to Local C.S.
    ResMRGlenoHumXL = zeros(rows,1); ResMRGlenoHumYL = zeros(rows,1);
ResMRGlenoHumZL = zeros(rows,1);
    for i=1:rows
        ResMRGlenoHumXL(i,:) =
dot(transpose(ResMRGlenoHumG(i,:)),RUArm_X(i,:));
        ResMRGlenoHumYL(i,:) =
dot(transpose(ResMRGlenoHumG(i,:)),RUArm_Y(i,:));
        ResMRGlenoHumZL(i,:) =
dot(transpose(ResMRGlenoHumG(i,:)),RUArm_Z(i,:));
    end
    ResMRGlenoHumL = [ResMRGlenoHumXL,ResMRGlenoHumYL,ResMRGlenoHumZL];
%GlenoHumeral Moments
    MRGlenoHumL = HRHum+ResMRGlenoHumL;
    MRGlenoHumLNorm = (MRGlenoHumL/(Subj_Weight*Subj_Height))*100;
%Translate back to Global coordinate system and normalize
    MRGlenoHumG = zeros(rows,3);
    for i=1:rows
        RUArm_Axes = [RUArm_X(i,:);RUArm_Y(i,:);RUArm_Z(i,:)];
        MRGlenoHumG(i,:) = MRGlenoHumL(i,:)*RForearm_Axes;
    end
    MRGlenoHumGNorm = (MRGlenoHumG/(Subj_Weight*Subj_Height))*100;
end

if SWSide == 2
    SIMILAR TO RIGHT SIDE
end

%Convert Angle measurements from radians to degrees
RWrAngD = RWrAng*(180/pi); LWrAngD = LWrAng*(180/pi);
RElbAngD = RElbAng*(180/pi); LElbAngD = LElbAng*(180/pi);
    SIMILAR FOR REMAINING ANGULAR DATA

reply = input('Do you wish to write the data to an excel file? Y or N\n','s');
if strcmp (reply, 'Y')
    %Output Data to an Excel File
        CODE HERE WRITES ALL DATA TO AN EXCEL SPREADSHEET

```

A.3.3 Scapula Kinematics

A.3.3.1 – Main Scapular Kinematics

ScapKinematicsCheck.m is the main scapular kinematics code, following the work and method of Senk et al.

```
%First need information from the static trial to set up the scapular solid
%from the AA, AC and SS markers and to determine the relative positions of
%the TS and AI markers to the scapular solid.
```

```
%Step One, read in marker position data from static trial c3d file
function [RTS,LTS,RAI,LAI,ThoraxAngS] =
ScapKinematicsCheck(SWDirection,StartFrame,EndFrame,ViconFilePath,StaticViconFP
)
```

```
    test = c3dserver();
%Read in Kinematic Data from c3d file
openc3d(test,3,StaticViconFP); %Opens the c3d
%First argument: test is the name I gave to the c3d server when downloaded,
%Second/Third argument(s): any number other than one allows for the file name
and path to be entered as a third argument
%Read in marker position data,
%First argument: call c3d server
%Second argument: use marker name as string
%Third argument: 0 means read in xyz position data as matrix,
                  %1 means xyz data and the residual,
%Optional 4th/5th arguments: Can enter desired start and end frames of data,
                  %no numbers here and all data in the channel is obtained
```

```
RTSs = get3dtarget(test,'RTS',0);
LTSSs = get3dtarget(test,'LTS',0);
RAIs = get3dtarget(test,'RAI',0);
LAIs = get3dtarget(test,'LAI',0);
RAAs = get3dtarget(test,'RAA',0);
LAAs = get3dtarget(test,'LAA',0);
RSSs = get3dtarget(test,'RSS',0);
LSSs = get3dtarget(test,'LSS',0);
RACRs = get3dtarget(test,'RACR',0);
LACRs = get3dtarget(test,'LACR',0);
SPC7s = get3dtarget(test,'SPC7',0,StartFrame,EndFrame);
STRNs = get3dtarget(test,'STRN',0,StartFrame,EndFrame);
IJMs = get3dtarget(test,'IJ',0,StartFrame,EndFrame);
%framenum = nframes(test); %obtains total number of frames
```

```
tempRTSs= RTSs(:,2); RTSs(:,2)= RTSs(:,3); RTSs(:,3)= -tempRTSs;
tempLTSSs= LTSSs(:,2); LTSSs(:,2)= LTSSs(:,3); LTSSs(:,3)= -tempLTSSs;
tempRSSs= RSSs(:,2); RSSs(:,2)= RSSs(:,3); RSSs(:,3)= -tempRSSs;
tempLSSs= LSSs(:,2); LSSs(:,2)= LSSs(:,3); LSSs(:,3)= -tempLSSs;
tempRAAs= RAAs(:,2); RAAs(:,2)= RAAs(:,3); RAAs(:,3)= -tempRAAs;
tempLAAs= LAAs(:,2); LAAs(:,2)= LAAs(:,3); LAAs(:,3)= -tempLAAs;
tempRAIs= RAIs(:,2); RAIs(:,2)= RAIs(:,3); RAIs(:,3)= -tempRAIs;
tempLAIs= LAIs(:,2); LAIs(:,2)= LAIs(:,3); LAIs(:,3)= -tempLAIs;
tempRACRs= RACRs(:,2); RACRs(:,2)= RACRs(:,3); RACRs(:,3)= -tempRACRs;
tempLACRs= LACRs(:,2); LACRs(:,2)= LACRs(:,3); LACRs(:,3)= -tempLACRs;
tempSPC7s= SPC7s(:,2); SPC7s(:,2)= SPC7s(:,3); SPC7s(:,3)= -tempSPC7s;
tempSTRNs= STRNs(:,2); STRNs(:,2)= STRNs(:,3); STRNs(:,3)= -tempSTRNs;
tempIJMs= IJMs(:,2); IJMs(:,2)= IJMs(:,3); IJMs(:,3)= -tempIJMs;
```

```
%Calculation of global parameter G from marker coordinates obtained through
%motion analysis system
```

```

%Need to calculate p and a, the barycenters first.
%Determine the barycentre of the static solidified scapular triangle
%First need to determine the positions of each marker
RAAsAvg = mean(RAAs); LAAsAvg = mean(LAAs);
RACRsAvg = mean(RACRs); LACRsAvg = mean(LACRs);
RSSsAvg = mean(RSSs); LSSsAvg = mean(LSSs);
    %And for later use:
    RAIsAvg = mean(RAIs); LAIsAvg = mean(LAIs);
    RTSsAvg = mean(RTSs); LTSsAvg = mean(LTSs);
%Matrix 'a' is the barycentre of the "solidified" static marker positions
%[Righta] = (1/3)*(AvgRAA+AvgRACR+AvgRSS);
%[Lefta] = (1/3)*(AvgLAA+AvgLACR+AvgLSS);
Ra = (1/3).*(RAAsAvg+RACRsAvg+RSSsAvg);
La = (1/3).*(LAAsAvg+LACRsAvg+LSSsAvg);

%Calculate the distance from the average static position of each marker
%from the barycentre of the marker averages
Rhlp1=(RAAsAvg-Ra);
Rhlp2=(RACRsAvg-Ra);
Rhlp3=(RSSsAvg-Ra);
Lhlp1=(LAAsAvg-La);
Lhlp2=(LACRsAvg-La);
Lhlp3=(LSSsAvg-La);

%Now need information from dyanmic trial.
%Read in Kinematic Data from c3d file
openc3d(test,3,ViconFilePath); %Opens the c3d
RAAd = get3dtarget(test,'RAA',0,StartFrame,EndFrame);
LAAd = get3dtarget(test,'LAA',0,StartFrame,EndFrame);
RSSd = get3dtarget(test,'RSS',0,StartFrame,EndFrame);
LSSd = get3dtarget(test,'LSS',0,StartFrame,EndFrame);
RACRd = get3dtarget(test,'RACR',0,StartFrame,EndFrame);
LACRd = get3dtarget(test,'LACR',0,StartFrame,EndFrame);

framesused = EndFrame-StartFrame+1;
framed = zeros(1,framesused)';
for i=1:framesused
    framed(i) = 1;
end

tempRSS= RSSd(:,2); RSSd(:,2)= RSSd(:,3); RSSd(:,3)= -tempRSS;
tempLSS= LSSd(:,2); LSSd(:,2)= LSSd(:,3); LSSd(:,3)= -tempLSS;
tempRAA= RAAd(:,2); RAAd(:,2)= RAAd(:,3); RAAd(:,3)= -tempRAA;
tempLAA= LAAd(:,2); LAAd(:,2)= LAAd(:,3); LAAd(:,3)= -tempLAA;
tempRACR= RACRd(:,2); RACRd(:,2)= RACRd(:,3); RACRd(:,3)= -tempRACR;
tempLACR= LACRd(:,2); LACRd(:,2)= LACRd(:,3); LACRd(:,3)= -tempLACR;

%Determine the measured triangle marker set barycentre for each frame and
%calculate the matrix G, then send this G matrix to the Veldapaus function
%in order to determine the rotation matrix between the static marker set
%and the marker set during each dynamic frame
RAA = zeros(framesused,3); RSS = zeros(framesused,3); RACR =
zeros(framesused,3);
LAA = zeros(framesused,3); LSS = zeros(framesused,3); LACR =
zeros(framesused,3);
for i=1:framesused
    %Right Side determination of matrix G and rotation matrix from Veldpau
    [Rpm] = (1/3).*(RAAd(i,:)+RACRd(i,:)+RSSd(i,:));
    [RG1] = transpose(RAAd(i,:)-Rpm)*Rhlp1;
    [RG2] = transpose(RACRd(i,:)-Rpm)*Rhlp2;
    [RG3] = transpose(RSSd(i,:)-Rpm)*Rhlp3;
    RG = (1/3).*(RG1+RG2+RG3);
    RRot = VeldpauCalc(RG);

```



```

Rr = Rpm - Ra;
%Right Side replacement of dynamic AA, AC and SS markers using R and r
RAA(i,:) = transpose(Ra+Rr)+RRot*transpose((RAAsAvg-Ra));
RSS(i,:) = transpose(Ra+Rr)+RRot*transpose((RSSsAvg-Ra));
RACR(i,:) = transpose(Ra+Rr)+RRot*transpose((RACRsAvg-Ra));
%Left Side determination of matrix G and rotation matrix from Veldpaus
LEFT SIDE SIMILAR TO RIGHT SIDE
end

%All measured markers of the scapular solid have been replaced via Veldpaus
%least-squared-error method. Now can determine position of TS and AI
%markers during the dynamic trial, via Senks method.

%Determine relation of scapular solid to global during static trial for ref
Global_Axes = [1 0 0;0 1 0;0 0 1];
[RS_Xs,RS_Ys,RS_Zs] =
Create_Scap_Axes(RAAsAvg,RACRsAvg,RSSsAvg,LAAsAvg,LACRsAvg,LSSsAvg,'Right');
[LS_Xs,LS_Ys,LS_Zs] =
Create_Scap_Axes(RAAsAvg,RACRsAvg,RSSsAvg,LAAsAvg,LACRsAvg,LSSsAvg,'Left');
RScaps_Axes = [RS_Xs;RS_Ys;RS_Zs];
RSs_Axes = transpose(RScaps_Axes);
%RScapsAng = Determine_Euler_Angles_RadAtan2(Global_Axes,RSs_Axes,'ZXYsf');
%Now need to calculate the rotation matrice for these angles
RRs = Global_Axes\RSs_Axes;

LEFT SIDE IS SIMILAR TO RIGHT SIDE

%Create temporary scapular axes based on the three markers creating the
%scapular solid: AA, AI and SS. Z-axis is directed to the right along the
%SS/AA line, the y-axis is perpendicular to the plane created by all three
%markers and the x-axis is y-axis crossed with the z-axis.
[RS_X,RS_Y,RS_Z] = Create_Scap_AxesD(RAA,RACR,RSS,LAA,LACR,LSS,'Right');
[LS_X,LS_Y,LS_Z] = Create_Scap_AxesD(RAA,RACR,RSS,LAA,LACR,LSS,'Left');

RScaptAng = zeros(framesused,3); %Preallocating improves performance
LScaptAng = zeros(framesused,3); %Preallocating improves performance
RTSinBGlob = zeros(framesused,3); LTSinBGlob = zeros(framesused,3);
RAIinBGlob = zeros(framesused,3); LAIinBGlob = zeros(framesused,3);
for i=1:framesused
    RScapt_Axes = [RS_X(i,:);RS_Y(i,:);RS_Z(i,:)];
    RSt_Axes = transpose(RScapt_Axes);
    RScaptAng(i,:) =
Determine_Euler_Angles_RadAtan2(Global_Axes,RSt_Axes,'ZXYsf');
    RTSinAGlob = RTSsAvg-RAAsAvg;
    RTSinALoc = RRs*RTSinAGlob';
    RTSinBLoc = (Global_Axes\RSt_Axes)'*RTSinALoc;
    RTSinBGlob(i,:) = RTSinBLoc'+RAA(i,:);

    RAIinAGlob = RAIsAvg-RAAsAvg;
    RAIinALoc = RRs*RAIinAGlob';
    RAIinBLoc = (Global_Axes\RSt_Axes)'*RAIinALoc;
    RAIinBGlob(i,:) = RAIinBLoc'+RAA(i,:);

LEFT SIDE IS SIMILAR TO RIGHT SIDE
end
RTS = RTSinBGlob; LTS = LTSinBGlob;
RAI = RAIinBGlob; LAI = LAIinBGlob;

```

A.3.3.2 – Veldpaus Rotation Matrix Calculation

The VeldpausCalc function as used in the ScapKinematicsCheck.m file. Rotation matrix calculation as developed by Veldpaus and used by Senk.

```
function RotationMatrix = VeldpausCalc(G)
%global parameters: G = RB, and RNKG is rank of G
%calculation of adjoint of G
GAD = adjt(G);
%calculation of determinant of G
DETG = det(G);
%transpose of G
TRANG = transpose(G);
P = TRANG*G;
PAD = adjt(P);
%Calculation of invariants J1, J2 and J3
%J1 is the trace of P, summation of diagonal elements
J1 = trace(P);
J2 = trace(PAD);
J3 = DETG*DETG;
%Calculation of the rank
%If RANK of G is less than 2, no decomposition is possible (exit out)
RNKG = rank(G);
%Calculation of the invariants of matrix B by Newton-Raphson Method
%tolerance for convergence is EPS
EPS = 1E-10;
X=1.0;
Y=1.0;
H1 = sqrt(J2)/J1;
H2 = DETG*sqrt(J1)/J2;
DET = X*Y-H1*H2;
HELP1 = 0.5*(1-X*X+2*H1*Y);
HELP2 = 0.5*(1-Y*Y+2*H2*X);
DX = (Y*HELP1+H1*HELP2)/DET;
DY = (H2*HELP1+X*HELP2)/DET;
while ((DX*DX)/(X*X)+(DY*DY)/(Y*Y))>=EPS
    X=X+DX;
    Y=Y+DY;
    DET = X*Y-H1*H2;
    HELP1 = 0.5*(1-X*X+2*H1*Y);
    HELP2 = 0.5*(1-Y*Y+2*H2*X);
    DX = (Y*HELP1+H1*HELP2)/DET;
    DY = (H2*HELP1+X*HELP2)/DET;
end
X=X+DX;
Y=Y+DY;
BETA1 = X*sqrt(J1);
BETA2 = Y*sqrt(J2);
BETA3 = DETG;
%Calculation of R and B Solving eqns 4.9 and 4.10 in Veldpaus 1988
Ident = eye(3);
PART1 = BETA1*G+GAD;
PART2 = P+BETA2*Ident;
%inv is slow and inaccurate, use A\b for INV(A)*b, and b/A for b*inv(A)
RotationMatrix = PART1/PART2;
```

A.3.4 – Additional Functions in Biomechanical Model

Axes Creation - Similar functions were created for all segments

```
% This function calculates a segment axes for the forearm
function [Forearm_X,Forearm_Y,Forearm_Z] =
Create_Forearm_Axes (RULN,RRAD,REJC,LULN,LRAD,LEJC,Side)

for i=1:length(RRAD)
    if strcmpi(Side, 'Right')
        %Forearm_Origin = RULN;
        Forearm_Y(i,:) = unit(REJC(i,:)-RULN(i,:));
        Temp_Vec(i,:) = unit(RULN(i,:)-RRAD(i,:));
    elseif strcmpi(Side, 'Left')
        %Forearm_Origin = LULN;
        Forearm_Y(i,:) = unit(LEJC(i,:)-LULN(i,:));
        Temp_Vec(i,:) = unit(LRAD(i,:)-LULN(i,:));
    end
    Forearm_X(i,:) = cross(Temp_Vec(i,:),Forearm_Y(i,:));
    Forearm_Z(i,:) = cross(Forearm_X(i,:),Forearm_Y(i,:));
end
```

Euler Angle Determination

```
%%This function calculates the Euler angles between two segments, distal
%%with respect to proximal. (normally: [D]=[R][P], must solve: [D]/[P] = [R];

function EAngles = Determine_Euler_Angles_RadAtan2(proxseg,distseg,rot_order)
%Rot_Matrix = proxseg\distseg; %solves [D] =[P][R] for [R]
Rot_Matrix = proxseg\distseg;
%For rotations about the global axis, the rotation matrix is post-multiplied
%because these rotations are "space-fixed". (i.e. dist =[prox]*Rz*Rx*Ry). Thus:

%[ cos(z)*cos(y)-sin(z)*sin(x)*sin(y), -sin(z)*cos(x),
cos(z)*sin(y)+sin(z)*sin(x)*cos(y)]
%[ sin(z)*cos(y)+cos(z)*sin(x)*sin(y), cos(z)*cos(x), sin(z)*sin(y)-
cos(z)*sin(x)*cos(y)]
%[ -cos(x)*sin(y), sin(x), cos(x)*cos(y)]

if strcmpi(rot_order, 'ZXYsf')
    AngX = asin(Rot_Matrix(3,2));
    AngY = atan2((Rot_Matrix(3,1)/(-
1*cos(AngX))), (Rot_Matrix(3,3)/(cos(AngX))));
    AngZ = atan2((Rot_Matrix(1,2)/(-
1*cos(AngX))), (Rot_Matrix(2,2)/(cos(AngX))));
elseif
end
EAngles = [AngX,AngY,AngZ];
```

Angular Velocity Calculation (Acceleration Calculation is similar)

```
function SegmentAngVel = CalculateAngVel(SegmentX,SegmentY,SegmentZ,samplerate)
n=length(SegmentX);
for i=2:n-1
    SegmentAngVelX(i) = (SegmentX(i+1)-SegmentX(i-1))*(samplerate/2);
    SegmentAngVelY(i) = (SegmentY(i+1)-SegmentY(i-1))*(samplerate/2);
    SegmentAngVelZ(i) = (SegmentZ(i+1)-SegmentZ(i-1))*(samplerate/2);
end
SegmentAngVelX(n)=0; SegmentAngVelY(n)=0; SegmentAngVelZ(n)=0;
SgAVelX = transpose(SegmentAngVelX); SgAVelY = transpose(SegmentAngVelY);
SgAVelZ = transpose(SegmentAngVelZ); SegmentAngVel = [SgAVelX,SgAVelY,SgAVelZ];
```

Appendix 4: Coordinate System Diagrams

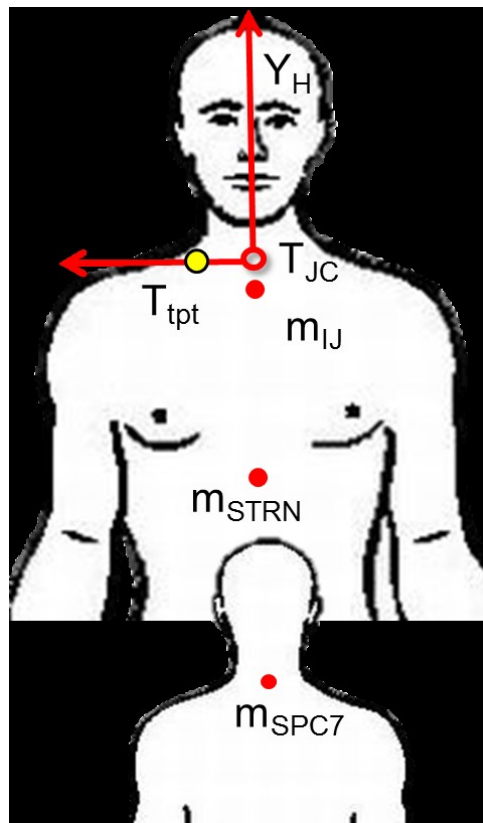


Figure 1: Thorax coordinate system

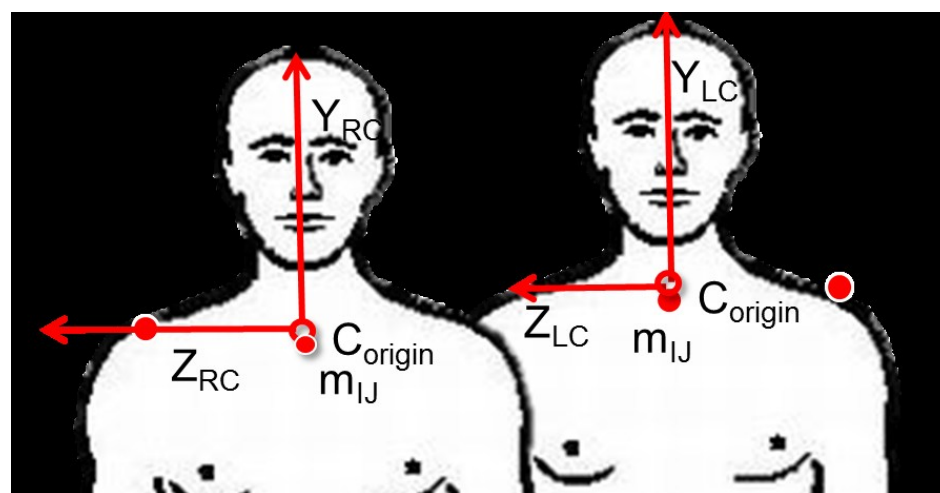


Figure 2: Right clavicle coordinate system,

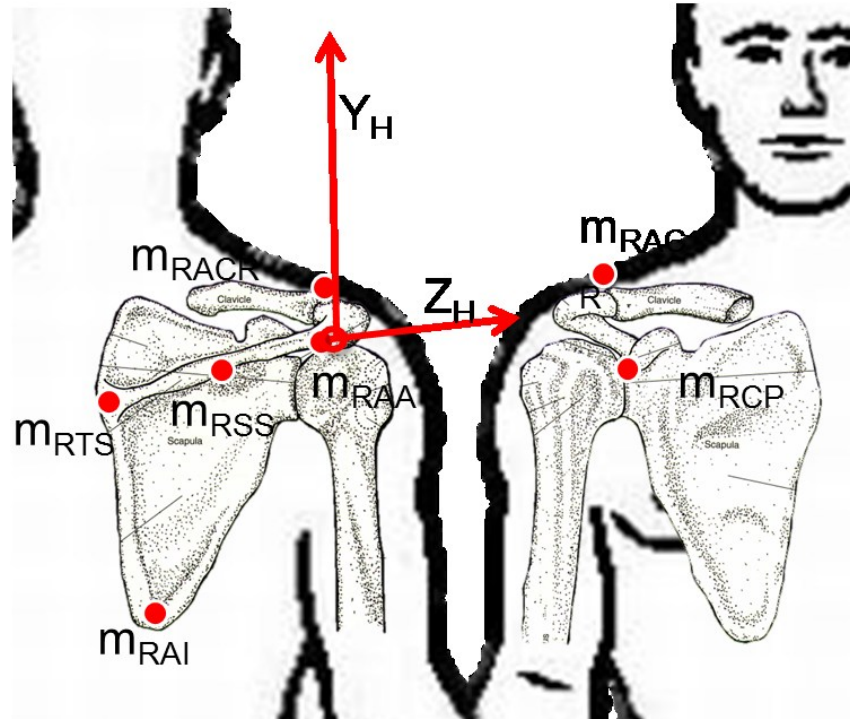


Figure 3: Right scapula coordinate system

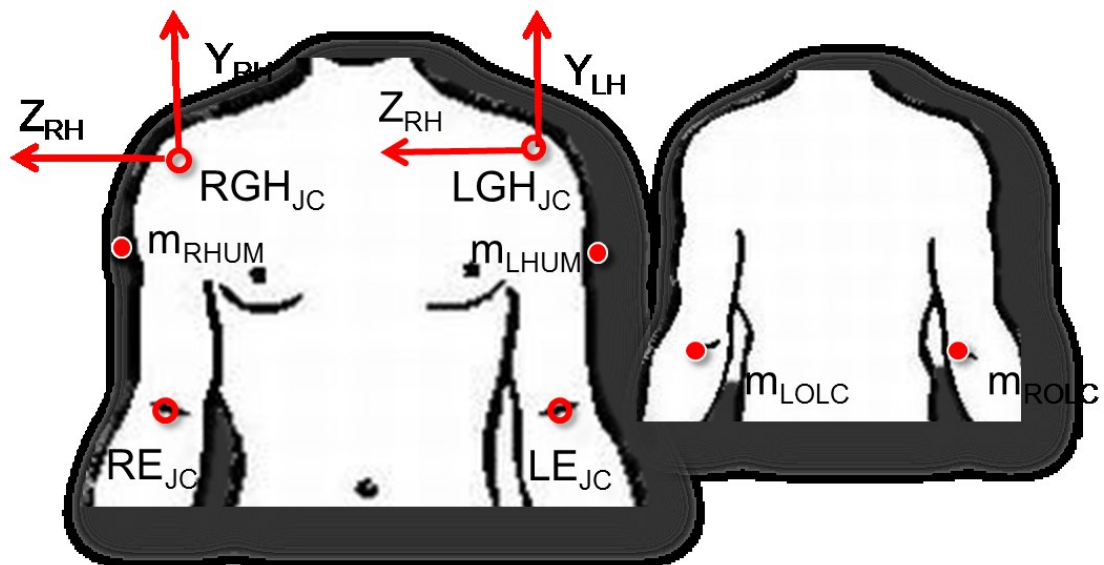


Figure 4: Left and right humerus coordinate systems

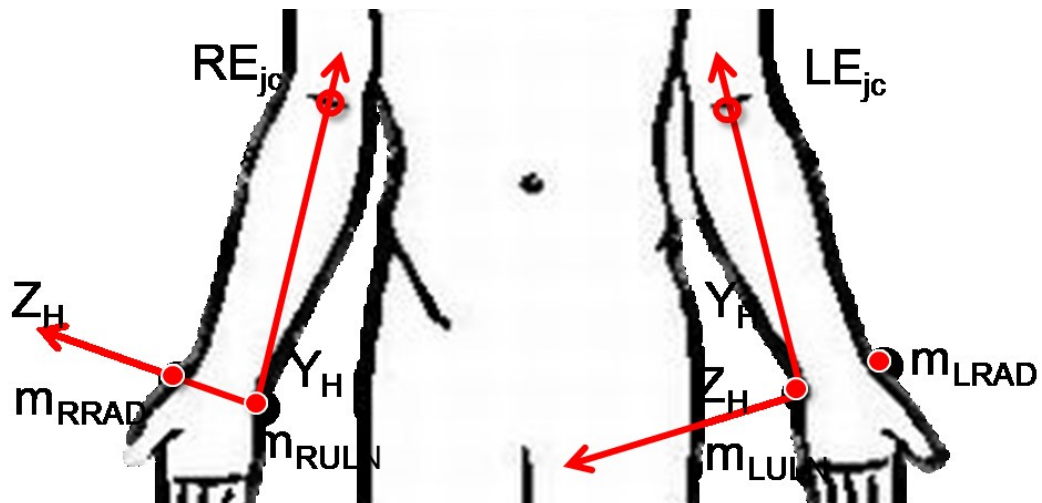


Figure 5: Left and right forearm coordinate systems



Figure 6: Left and right hand coordinate systems

Appendix 5: SmartWheel Specifications

Table 1: SmartWheel specifications

Parameter	Specification
Sampling Frequency	Selectable: 30 – 300 Hz
Digital Sample Resolution	12 bit
Startup Angle Detection Accuracy	+/- 2 degrees
Encoder Resolution	4096 counts/wheel revolution
Battery Life	3+ hours
On-board data storage Capacity at 240Hz	1 hour and 25 minutes
Wheel Size Options	22", 24", 25" or 26"
Tire Type	Alshin AL44 Urethane
Axle Type	½ inch Split-Axle quick release
Handrim Type	Standard ¾ inch tubular
Communication Range	Indoor: 300 feet Outdoor: 500 feet

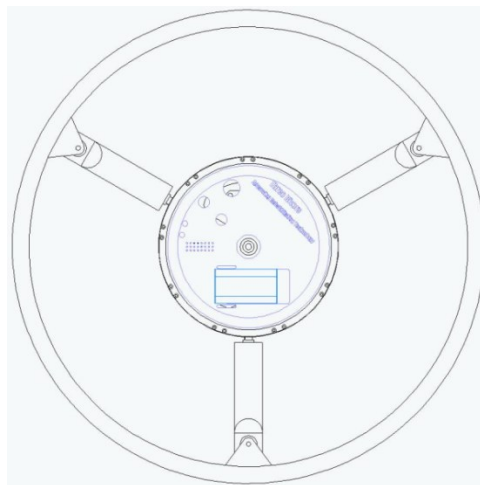


Figure 1: SmartWheel diagram